

# Rational Design of Two-Dimensional Transition Metal Carbide/Nitride (MXene) Hybrids and Nanocomposites for Catalytic Energy Storage and Conversion

*Kang Rui Garrick Lim<sup>1</sup>, Albertus D. Handoko<sup>1</sup>, Srinivasa Kartik Nemani<sup>2</sup>, Brian Wyatt<sup>2</sup>, Hai-Ying Jiang<sup>3</sup>, Junwang Tang<sup>4</sup>, Babak Anasori<sup>2\*</sup>, Zhi Wei Seh<sup>1\*</sup>*

<sup>1</sup> Institute of Materials Research and Engineering, Agency for Science, Technology and Research (A\*STAR), 2 Fusionopolis Way, Innovis, Singapore 138634, Singapore

<sup>2</sup> Department of Mechanical and Energy Engineering, and Integrated Nanosystems Development Institute, Indiana University-Purdue University Indianapolis, Indianapolis, 46202, USA

<sup>3</sup> Key Lab of Synthetic and Natural Functional Molecule Chemistry of Ministry of Education, and the College of Chemistry and Materials Science, College of Chemistry and Materials Science, Northwest University, Xi'an 710127, P. R. China

<sup>4</sup> Department of Chemical Engineering, University College London, Torrington Place, London, WC1E 7JE, UK

## Corresponding Authors

\*Z. W. Seh: [sehzw@imre.a-star.edu.sg](mailto:sehzw@imre.a-star.edu.sg)

\*B. Anasori: [banasori@iupui.edu](mailto:banasori@iupui.edu)

---

This is the author's manuscript of the article published in final edited form as:

Lim, K. R. G., Handoko, A. D., Nemani, S. K., Wyatt, B., Jiang, H.-Y., Tang, J., Anasori, B., & Seh, Z. W. (2020). Rational Design of Two-Dimensional Transition Metal Carbide/Nitride (MXene) Hybrids and Nanocomposites for Catalytic Energy Storage and Conversion. ACS Nano. <https://doi.org/10.1021/acsnano.0c05482>

1  
2  
3 ABSTRACT  
4  
5

6 Electro-, photo-, and photoelectrocatalysis play a critical role toward the realization of a  
7 sustainable energy economy. They facilitate numerous redox reactions in energy storage and  
8 conversion systems, enabling the production of chemical feedstock and clean fuels from abundant  
9 resources like water, carbon dioxide, and nitrogen. One major obstacle for their large-scale  
10 implementation is the scarcity of cost-effective, durable, and efficient catalysts. A family of two-  
11 dimensional transition metal carbides, nitrides, and carbonitrides (MXenes) has recently emerged  
12 as promising earth-abundant candidates for large-area catalytic energy storage and conversion due  
13 to their unique properties of hydrophilicity, high metallic conductivity, and ease of production by  
14 solution processing. To take full advantage of these desirable properties, MXenes have been  
15 combined with other materials to form MXene hybrids with significantly enhanced catalytic  
16 performances beyond the sum of their individual components. MXene hybridization tunes the  
17 electronic structure towards optimal binding of redox active species to improve intrinsic activity,  
18 while increasing the density and accessibility of active sites. This review outlines recent strategies  
19 in the design of MXene hybrids for industrially relevant electrocatalytic, photocatalytic, and  
20 photoelectrocatalytic applications such as water splitting, metal-air/sulfur batteries, carbon dioxide  
21 reduction, and nitrogen reduction. By clarifying the roles of individual material components in the  
22 MXene hybrids, we provide design strategies to synergistically couple MXenes with associated  
23 materials for highly efficient and durable catalytic applications. We conclude by highlighting key  
24 gaps in the current understanding of MXene hybrids to guide future MXene hybrid designs in  
25 catalytic energy storage and conversion applications.  
26  
27  
28  
29  
30  
31  
32  
33  
34  
35  
36  
37  
38  
39  
40  
41  
42  
43  
44  
45  
46  
47  
48  
49  
50  
51

52  
53 KEYWORDS: MXenes, hybrid material, electrocatalysis, photocatalysis, water splitting, CO<sub>2</sub>  
54 reduction, N<sub>2</sub> reduction, energy conversion, batteries, energy storage  
55  
56  
57  
58  
59  
60

1  
2  
3 The advancement of our energy economy using cost-effective, accessible, and  
4 environmentally responsible means is critical to ensure a sustainable supply to meet the burgeoning  
5 global energy demand.<sup>1,2</sup> In this regard, catalysts play a critical role in enabling efficient energy  
6 conversion of earth-abundant resources such as water, carbon dioxide, and nitrogen to clean fuels  
7 and chemical feedstock precursors such as hydrogen, hydrocarbons, and ammonia.<sup>3-5</sup> Durable and  
8 active catalysts are also required to facilitate long-term energy storage in H<sub>2</sub> fuel cells and batteries  
9 of varying architectures.<sup>6-8</sup> Presently, precious platinum group metals (PGMs) such as Pt, their  
10 alloys, and related structures (PtIr, IrO<sub>2</sub>, RuO<sub>2</sub>, *etc.*) are widely regarded as the most effective  
11 catalysts for the hydrogen evolution reaction (HER), oxygen reduction reaction (ORR), and  
12 oxygen evolution reaction (OER), respectively.<sup>9-11</sup> The widespread commercialization and  
13 adoption into energy storage and conversion devices however, can only be realized with alternative  
14 earth-abundant and cost-effective catalysts with high catalytic activity and stability.<sup>3,4</sup>  
15  
16  
17  
18  
19  
20  
21  
22  
23  
24  
25  
26  
27  
28  
29  
30

31 Since their discovery in 2011, more than 30 different compositions belonging to a family  
32 of two-dimensional (2D) transition metal carbides, nitrides, and carbonitrides (MXenes) have been  
33 successfully synthesized, with many other stable compositions predicted theoretically.<sup>12-14</sup>  
34 MXenes have attracted significant attention as promising catalysts due to their unique combination  
35 of physical and chemical properties.<sup>13-15</sup> They possess high metallic electrical conductivity with  
36 hydrophilicity similar to graphene oxide, and mechanical strength of transition metal (TM)  
37 carbides/nitrides. MXenes can be easily scaled, because of their solution processible top-down  
38 synthesis, into stable colloidal solutions or flexible films for energy applications (electrocatalysts,  
39 batteries, and supercapacitors) and beyond (flexible electronics, sensors, and electromagnetic  
40 shielding).<sup>13,14,16</sup> In addition to their high metallic conductivity to facilitate efficient electronic  
41 charge transport at the electrode-electrolyte interface, the large-area 2D basal planes of MXenes  
42  
43  
44  
45  
46  
47  
48  
49  
50  
51  
52  
53  
54  
55  
56  
57  
58  
59  
60

1  
2  
3 are HER-active,<sup>17–19</sup> unlike the widely studied semiconducting 2H-MoS<sub>2</sub> with HER activity  
4 restricted only to their edges.<sup>20</sup> Separate theoretical calculations have also predicted a variety of  
5 MXenes for efficient photocatalytic (PC), electrocatalytic (EC), and photoelectrocatalytic (PEC)  
6 reactions such as the hydrogen evolution (HER), oxygen evolution (OER), oxygen reduction  
7 (ORR), carbon dioxide reduction (CO<sub>2</sub>RR), and nitrogen reduction (N<sub>2</sub>RR) reactions.<sup>21–25</sup> MXenes  
8 have a general formula of M<sub>n+1</sub>X<sub>n</sub>T<sub>x</sub> where n = 1–4, M = early transition metal such as Ti, V and  
9 Mo, X = C and/or N and T<sub>x</sub> = surface termination groups such as –O, –OH, –F, and –Cl, which are  
10 formed on the outer M basal plane during the synthesis process.<sup>26–28</sup> For consistency, a  
11 standardized notation of M<sub>n+1</sub>X<sub>n</sub>T<sub>x</sub> will be used to describe MXenes throughout this review.  
12  
13  
14  
15  
16  
17  
18  
19  
20  
21  
22  
23

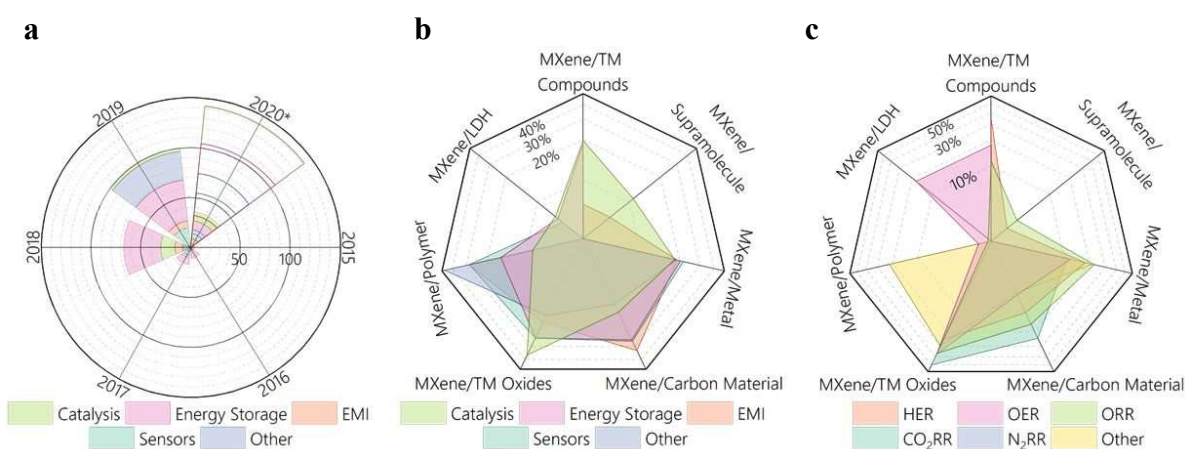
24  
25 MXenes are most commonly produced through the top-down separation of layered MXene  
26 sheets from their parent layered ternary TM carbide MAX phase materials (“A” = group 13 or 14  
27 elements such as Al, Si, and Ga) by aqueous wet selective etching and removal of A-group atom  
28 layers.<sup>12,27</sup> The A-group atom layers are preferentially etched away as the M-A bonds binding the  
29 MXene layers together in the MAX structure are chemically more active than the stronger M-X  
30 bonds within the MXene sheets.<sup>29–31</sup> This scalable top-down etching process to produce MXenes  
31 is most commonly conducted under ambient conditions with gentle heating using hydrofluoric acid  
32 (HF) directly, or HF produced *in-situ* from F-containing etchants.<sup>32–35</sup> After etching away the A-  
33 group atom layers, the exposed outer M basal planes of the etched MXene sheets are functionalized  
34 with hydrophilic surface termination groups (T<sub>x</sub>) such as –O, –OH, –F and –Cl due to the aqueous  
35 F- or Cl-containing etchants.<sup>14,31,36</sup> The surface chemistry of MXenes can be controlled to some  
36 extent by the selective wet etching conditions or through post-etch processing to optimize binding  
37 toward specific electroactive species for efficient catalysis.<sup>18,37</sup> Subsequent delamination and  
38 exfoliation separates the weakly bound MXene sheets into single- or few-layered MXenes using  
39  
40  
41  
42  
43  
44  
45  
46  
47  
48  
49  
50  
51  
52  
53  
54  
55  
56  
57  
58  
59  
60

1  
2  
3 intercalants,<sup>38,39</sup> exposing large MXene surface areas for catalysis and to serve as a conductive  
4 support for co-catalysts.  
5  
6

7  
8  
9 Most recently, organic and inorganic materials such as TM compounds (carbides,  
10 phosphides, chalcogenides, oxides, *etc.*), layered double hydroxides (LDHs), metal-organic  
11 frameworks (MOFs), carbon-based (C-based) materials such as graphitic carbon nitride (*g*-C<sub>3</sub>N<sub>4</sub>)  
12 and carbon nanotubes (CNTs), quantum dots (QDs), metallic alloys, and polymers have been  
13 combined with MXenes to form MXene hybrids and composites.<sup>40–45</sup> These MXene hybrids  
14 exhibit significantly enhanced catalytic activities and stability beyond the sum of their individual  
15 components, due to synergistic coupling between MXenes and the secondary materials. The strong  
16 and intimate coupling increases the density of catalytically active sites, and optimizes these active  
17 sites toward binding of electrochemically active species for efficient catalysis.<sup>40–45</sup> The hybrid mix  
18 can perform a variety of functions such as a large-area, electronically conductive support,  
19 electronic structure modulator, and co-catalyst,<sup>40–45</sup> as we discuss in this review. Indeed, MXene  
20 hybrids have garnered significant traction since 2014, with the number of papers published  
21 doubling year-on-year, and more than half (168) of the publications on MXene hybrids in 2019  
22 (312) focused on catalysis and energy storage (**Figure 1a**). The breakdown of the many different  
23 secondary materials integrated with MXenes to form MXene hybrids also illustrates the versatility  
24 of MXene hybrids to meet the demands of a wide spectrum of applications (**Figure 1b**), especially  
25 in the many important catalytic reactions of interest (**Figure 1c**).  
26  
27  
28  
29  
30  
31  
32  
33  
34  
35  
36  
37  
38  
39  
40  
41  
42  
43  
44  
45  
46  
47  
48

49 In this review, we summarize recent strategies in the design of MXene hybrids for  
50 industrially relevant EC, PC, and PEC applications in energy storage (metal-air/sulfur batteries  
51 catalyzed by OER, ORR, and sulfur redox reactions) and conversion (water splitting catalyzed by  
52 OER and HER). We clarify the roles of each material component in the MXene hybrids for their  
53  
54  
55  
56  
57  
58  
59  
60

intended applications to provide a set of rational design rules to synergistically couple MXenes with the relevant secondary materials for highly efficient and durable catalysis. The feasibility of MXene hybrids for important emerging catalytic applications such as CO<sub>2</sub>RR and N<sub>2</sub>RR is then discussed. The review concludes by highlighting key gaps in the current fundamental understanding of MXene hybrids and provides an outlook to inform forthcoming MXene hybrid designs in catalytic energy storage and conversion applications.

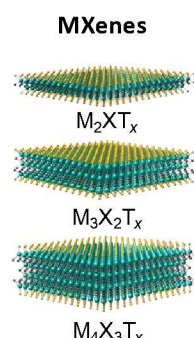
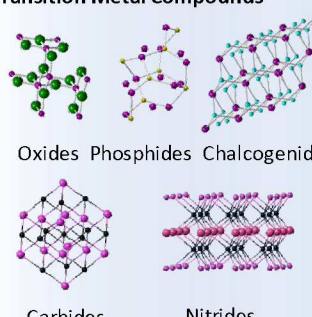
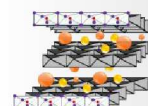
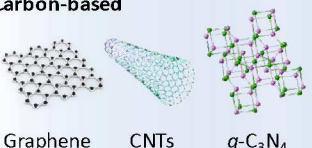

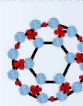


**Figure 1.** (a) Graphical representation of the total publications to date (\*March 2020) on MXene hybrids for various applications on Web of Science. Color filled radial bars represent different applications, while uncolored radial bars are the projected number of publications for the rest of 2020. (b) Spider plot survey of all MXene hybrid publications to date, illustrating the type of MXene hybrids most used for specific applications. For example, 31% of all published MXene hybrid papers for catalysis used MXene/TM oxides hybrids. (c) Spider plot survey of all MXene hybrid publications for catalysis to date, illustrating the type of MXene hybrids most used for various catalytic reactions of interest. For instance, MXene/TM compound hybrids account for 32% of all HER-related papers using MXene hybrids. Raw data used for each plot is provided in **Tables S1a–S1c** respectively.

## DESIGN STRATEGIES FOR MXENE HYBRIDS AND COMPOSITES

The layered nature and variety in surface  $T_x$  groups of MXenes<sup>30</sup> afford a high degree of tuneability in their properties<sup>13-15</sup> and hence, strong compatibility with a wide range of secondary materials to produce MXene hybrids with high catalytic performances. MXene hybrids with precise and well-formed interfaces have been reported to improve charge transfer,<sup>46-48</sup> mitigate volumetric expansion in batteries<sup>49,50</sup> and resist secondary material agglomeration through confinement effects.<sup>51-53</sup> In this review, we define a MXene hybrid/composite as a material comprising MXenes and at least one other non-MXene material, either organic or inorganic. This is a more general term than MXene heterostructures, which are produced when a material is grown onto MXenes in a repetitive layered manner (see **Vocabulary** for full definition of MXene hybrid/composite and MXene heterostructures).

A growing number of MXenes have been integrated with non-MXene secondary materials to form MXene hybrids, realizing unique material properties and enhanced performance. These MXenes include, but are not limited to,  $Ti_2CT_x$ ,<sup>54</sup>  $Ti_3C_2T_x$ ,<sup>55,56</sup>  $Ti_3CNT_x$ ,<sup>56</sup>  $V_2CT_x$ ,<sup>57,58</sup>  $V_4C_3T_x$ ,<sup>59,60</sup>  $Nb_2CT_x$ ,<sup>61,62</sup>  $Nb_4CT_x$ ,<sup>62</sup>  $Mo_{1.33}CT_x$ ,<sup>63</sup>  $Mo_2CT_x$ ,<sup>64-66</sup>  $Mo_2TiC_2T_x$ ,<sup>67</sup> and  $Ta_4C_3T_x$ .<sup>68</sup> Since rapid electronic charge transfer is crucial to efficient electrocatalysis,  $Ti_3C_2T_x$  is most extensively incorporated into MXene hybrids for electrocatalytic applications, due to their high electrical conductivity (up to  $15000\text{ S cm}^{-1}$ )<sup>69</sup> as compared to other MXenes. The wide diversity in MXene-compatible secondary materials (TM compounds, supramolecular structures, C-based materials, and metals), coupled with the many different synthetic methods to form these hybrids (**Figure 2**), illustrates the boundless potential for MXene hybrids and composites to meet the various demands in energy-related applications and beyond.<sup>40-44</sup>

	Secondary Materials	Processing method	Applications
<b>MXenes</b>  $M_2X_Tx$ $M_3X_2T_x$ $M_4X_3T_x$	<b>Transition Metal Compounds</b>  Oxides Phosphides Chalcogenides Carbides Nitrides	<i>In situ</i> oxidation/sulfidation Hydro/solvothermal synthesis Solution processing Electrostatic self-assembly Electrodeposition Dropcasting	Water splitting: HER/OER Metal-air battery: OER/ORR Metal-S battery: S cathode CO <sub>2</sub> RR, N <sub>2</sub> RR
	<b>Layered Double Hydroxides</b> 	Hydro/solvothermal synthesis Electrostatic self-assembly	Water splitting: HER/OER Metal-air battery: OER CO <sub>2</sub> RR
	<b>Carbon-based</b>  Graphene CNTs <i>g</i> -C <sub>3</sub> N <sub>4</sub>	Solution processing Electrostatic self-assembly Physical deposition (CVD, ALD)	Water splitting: OER Metal-air battery: OER/ORR Metal-S battery: S cathode CO <sub>2</sub> RR, N <sub>2</sub> RR
	<b>Element/ Multi-element</b>  Metals Metallic Alloys	Electrostatic self-assembly Solution processing (self-reduction stabilization)	Water splitting: HER/OER Metal-air battery: OER/ORR CO <sub>2</sub> RR, N <sub>2</sub> RR
	<b>Supramolecular Structures</b>  <b>MOFs</b>	Solution processing Electrostatic self-assembly	Water splitting: OER CO <sub>2</sub> RR

**Figure 2.** Three different MXene types combined with secondary materials to form MXene hybrids. Cyan, dark grey and yellow spheres represent M, X, and T<sub>x</sub> respectively. Common processing methods to fabricate the MXene hybrids and their catalytic applications are also listed.

The first step to designing efficient and durable MXene hybrids for energy storage and conversion is the deliberate choice of secondary material and the processing method. Highly interconnected charge transfer networks for electronic transport, a large-area/hierarchical/porous network for mass transfer of electroactive species, and an abundance of catalytically active sites, are all highly desirable properties in MXene hybrids for catalytic applications.<sup>40–44</sup> Additionally, a



1  
2  
3 strongly and chemically coupled MXene hybrid synergistically increases the hybrid's intrinsic  
4 activity, while secondary material dislodgement or degradation during electrocatalysis is  
5 prevented, especially at large applied potentials.<sup>70</sup> MXene hybrids are synthesized through three  
6 main routes: (1) *in-situ* conversion of the MXenes' surface structure through oxidation (*e.g.*  
7  $\text{Ti}_3\text{C}_2\text{T}_x$  to  $\text{TiO}_2$ )<sup>55</sup> or sulfidation (*e.g.*  $\text{Mo}_2\text{TiC}_2\text{T}_x$  to  $\text{MoS}_2$ ),<sup>67</sup> (2) reactive chemical formation of  
8 secondary materials on MXenes, using methods such as hydro/solvothermal synthesis,<sup>47,71,72</sup>  
9 solution processing,<sup>73</sup> or deposition,<sup>74–79</sup> and (3) non-reactive assembly of secondary materials by  
10 drop-casting<sup>80</sup> and adsorption processes.<sup>56</sup> In this section, we summarize the common and unique  
11 features for each of these three synthetic routes for MXene hybrid formation, highlighting their  
12 suitability, advantages, and shortfalls (and how they have been overcome).

13  
14  
15  
16  
17  
18  
19  
20  
21  
22  
23  
24  
25  
26  
27 ***In-situ* conversion of MXene surfaces to form MXene hybrids.** The layered structure of  
28 MXenes leaves the TM atomic layers exposed on their outer basal planes (left schematics in **Figure**  
29 **2**). These TM layers are highly oxophilic<sup>81,82</sup> and hence prone to surface reactions such as oxidation  
30 (*e.g.* Ti to  $\text{TiO}_2$  in  $\text{Ti}_3\text{C}_2\text{T}_x$ )<sup>55</sup> or sulfidation (*e.g.* Mo to  $\text{MoS}_2$  in  $\text{Mo}_2\text{TiC}_2\text{T}_x$ ).<sup>67</sup> In these processes,  
31 the MXenes' surface is transformed, either partially or fully, to form a second material. We thus  
32 refer to this process as an *in-situ* conversion of the MXenes' surface. The advantage of surface  
33 conversion is clear: the second material is strongly integrated with MXenes, forming a hybrid  
34 interface.<sup>67</sup> Since the MXene surfaces are directly involved in the conversion, no additional TM  
35 source is required for the secondary material growth. Consequently, this process is self-limited by  
36 the MXenes' surface exposure,<sup>67</sup> minimizing the issue of excessive secondary material nucleation  
37 and growth that would otherwise restrict access of reactants to catalytically active sites.

38  
39  
40  
41  
42  
43  
44  
45  
46  
47  
48  
49  
50  
51  
52  
53 Most surface conversions involve the treatment of MXenes with gases such as  $\text{O}_2$  or  $\text{CO}_2$   
54 for oxidation, or  $\text{H}_2\text{S}$  for sulfidation. These processes are typically conducted at elevated  
55  
56  
57  
58  
59  
60

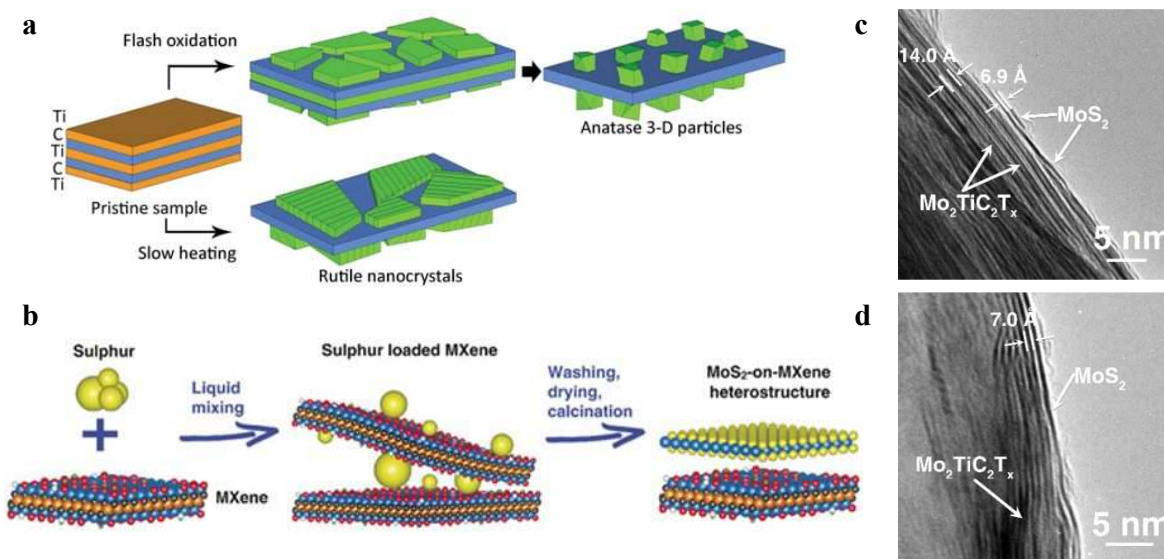
1  
2  
3 temperatures to form highly crystalline secondary materials on MXene surfaces.<sup>67,83</sup> Hence, there  
4 exists a delicate balance between the extent of MXene conversion, and preserving the MXenes'  
5 structural integrity that can be compromised in oxidizing environments at high temperatures.<sup>83</sup> The  
6 range of secondary materials that can be grown through MXene surface conversion is also limited  
7 by the chemical identity and reactivity of the MXenes' TM surface exposed. For instance, the Ti  
8 surface of  $\text{Ti}_3\text{C}_2\text{T}_x$  implies that only Ti-based secondary materials can be grown through this  
9 conversion route. In this regard, we anticipate that disordered solid solution MXenes such as  
10  $(\text{Ti},\text{V})_2\text{CT}_x$  and  $(\text{Mo},\text{V})_4\text{C}_3\text{T}_x$ , denoted by the chemical formula  $(\text{M}',\text{M}'')_{n+1}\text{C}_n\text{T}_x$ , will be interesting  
11 for growth of secondary materials through this surface conversion route, since they possess two  
12 different TMs at the surface in a random distribution.<sup>84</sup>

13  
14  
15  
16  
17  
18  
19  
20  
21  
22  
23  
24  
25  
26  
27  
28  
29  
30  
31  
32  
33  
34  
35  
36  
37  
38  
39  
40  
41  
42  
43  
44  
45  
46  
47  
48  
49  
50  
51  
52  
53  
54  
55  
56  
57  
58  
59  
60  
Thermally-assisted oxidation is an efficient one-step method to produce MXene/TM oxide  
hybrids.<sup>41,43</sup> MXene surface oxidation is most commonly employed in Ti-based MXenes to form  
 $\text{TiO}_2$  photocatalysts,<sup>55</sup> although oxidation can be also applied to V, Nb, and Mo-based MXenes to  
form their respective oxides.<sup>58,62,82</sup> *In-situ* oxidation is achieved through flash oxidation (1150 °C,  
30 s),<sup>55</sup> prolonged oxidation from calcination (350–650 °C),<sup>85–87</sup> hydro/solvothermal processes  
(120–220 °C),<sup>47,78,88–91</sup> or  $\text{CO}_2$  oxidation (500–900 °C).<sup>62,83</sup> Control over the MXenes' surface  $\text{T}_x$   
groups prior to oxidation is crucial, since different surface terminations have resulted in  
morphological differences in the oxides formed. Li *et al.* reported that calcining untreated  $\text{Ti}_3\text{C}_2\text{T}_x$   
with –O, –F, and –OH terminations resulted in larger anatase  $\text{TiO}_2$  nanoparticles (NPs) with  
exposed (001) planes, compared to the smaller and more spherical anatase  $\text{TiO}_2$  NPs formed by  
calcining  $\text{Ti}_3\text{C}_2\text{T}_x$  with primarily –OH terminations.<sup>87</sup> With precise control and optimization over  
the heat treatment conditions, a variety of functional  $\text{TiO}_2/\text{MXene}$  hybrids can be formed with high  
PC activity toward water splitting,  $\text{CO}_2\text{RR}$ , and  $\text{N}_2\text{RR}$ .<sup>87,89</sup>

1  
2  
3 For example,  $\text{Ti}_3\text{C}_2\text{T}_x$  has been oxidized to varying degrees to produce hybrids ranging  
4 from  $\text{Ti}_3\text{C}_2\text{T}_x/\text{TiO}_2$  (partial MXene surface oxidation) to  $\text{C}/\text{TiO}_2$  (complete MXene  
5 oxidation).<sup>83,92,93</sup> While controlled partial oxidation retained some of the Ti-C layered structure  
6 from the MXene precursor,<sup>92</sup> complete oxidation degraded the entire MXene structure.<sup>83</sup> The latter  
7 resulted in a Ti-O structure supported by C-C bonded layers, in the form of  $\text{TiO}_2$  on 2D carbon  
8 sheets ( $\text{C}/\text{TiO}_2$ ).<sup>83,94</sup> The morphology and phase of the resulting  $\text{TiO}_2$  NPs was also highly  
9 dependent on the treatment conditions.<sup>83,95</sup> This is important as the identity and quantity of exposed  
10 facets, together with the distribution and phase of  $\text{TiO}_2$  formed, directly influences PC activity.<sup>47,93</sup>  
11 Ghassemi *et al.* utilized *in-situ* environmental transmission electron microscopy (TEM) and  
12 Raman spectroscopy to elucidate the oxidation mechanism of  $\text{Ti}_3\text{C}_2\text{T}_x$  under various conditions  
13 (**Figure 3a**).<sup>96</sup> In flash oxidation, the exposed Ti basal planes serve as nucleating sites to form a  
14 thin 2D anatase  $\text{TiO}_2$  film. Subsequently, the 2D  $\text{TiO}_2$  nuclei grew vertically to form 3D  $\text{TiO}_2$   
15 anatase NPs from the outward migration of inner Ti layer atoms. Conversely, a slower heating  
16 process yielded rutile  $\text{TiO}_2$  NPs without the formation of the intermediate anatase phase.  
17 Experimentally, anatase  $\text{TiO}_2$  was formed from partial  $\text{Ti}_3\text{C}_2\text{T}_x$  oxidation at lower  
18 temperatures,<sup>47,62,83</sup> while rutile  $\text{TiO}_2$  was mostly formed through near-complete oxidation of  
19  $\text{Ti}_3\text{C}_2\text{T}_x$ , often resulting in degradation of the Ti-C MXene interior.<sup>83,97</sup>  
20  
21  
22  
23  
24  
25  
26  
27  
28  
29  
30  
31  
32  
33  
34  
35  
36  
37  
38  
39  
40  
41  
42

43 MXene/TM chalcogenides hybrids have also been formed through *in-situ* sulfidation of  
44 MXene surfaces.<sup>67</sup> Although TM chalcogenides are HER-active, they are less electrically  
45 conductive than MXenes. Thus, MXene/TM chalcogenides hybrids benefit from (1) significantly  
46 improved charge transfer kinetics due to the metallic MXenes, and (2) an increased number of  
47 active sites with TM chalcogenides acting as co-catalysts in the hybrid structure.<sup>70,89</sup> In ordered  
48 double TM (Mo, Ti) MXenes such as  $\text{Mo}_2\text{TiC}_2\text{T}_x$  and  $\text{Mo}_2\text{Ti}_2\text{C}_3\text{T}_x$ , Mo atoms preferentially  
49  
50  
51  
52  
53  
54  
55  
56  
57  
58  
59  
60

occupy the surface (outer) basal planes.<sup>98,99</sup> This led to a follow-up study on the *in-situ* sulfidation of the Mo-rich surface of  $\text{Mo}_2\text{TiC}_2\text{T}_x$  to form the  $\text{MoS}_2@\text{Mo}_2\text{TiC}_2\text{T}_x$  hybrid.<sup>67</sup> After an initial liquid mixing process to incorporate sulfur on and within the  $\text{Mo}_2\text{TiC}_2\text{T}_x$  sheets, heat treatment in an inert Ar atmosphere with additional elemental sulfur converted the surface Mo-O motifs to 2H- $\text{MoS}_2$  to form the final  $\text{MoS}_2@\text{Mo}_2\text{TiC}_2\text{T}_x$  hybrid (**Figure 3b**). The  $\text{Mo}_2\text{TiC}_2\text{T}_x$  :  $\text{MoS}_2$  ratio was also tuned from 1 : 0.62 and 1 : 2.19 by adjusting the treatment temperature from 500 to 700 °C. Furthermore, the intimate interfacial relationship was evident in the stacking of thin 2H- $\text{MoS}_2$  on the MXenes (**Figures 3c and 3d**). This 2H- $\text{MoS}_2$  on MXene hybrid exhibited an increased specific capacity when used as a lithium ion anode, which was attributed to the incorporation of  $\text{MoS}_2$ . We speculate that ordered double TM MXenes with a Mo-rich surface, such as  $\text{Mo}_2\text{TiC}_2\text{T}_x$  and  $\text{Mo}_2\text{Ti}_2\text{C}_3\text{T}_x$ , might be better suited for sulfidation compared to single TM MXenes ( $\text{Mo}_2\text{CT}_x$ ), due to the presence of a conductive inner Ti layer after surface Mo sulfidation to  $\text{MoS}_2$ .<sup>98–100</sup>



**Figure 3.** *In-situ* conversion of MXene surfaces to form MXene hybrids. (a) Oxidation mechanism of  $\text{Ti}_3\text{C}_2\text{T}_x$  to form  $\text{TiO}_2$  under different oxidation conditions. Adapted with permission from ref <sup>96</sup>. Copyright 2014 Royal Society of Chemistry. (b) *In-situ* sulfidation of  $\text{Mo}_2\text{TiC}_2\text{T}_x$  and cross-sectional TEM image of the resulting  $\text{MoS}_2@\text{Mo}_2\text{TiC}_2\text{T}_x$  hybrid heat treated at (c) 500 °C and (d) 700 °C. Adapted with permission from ref <sup>67</sup>. Copyright 2018 Wiley-VCH.

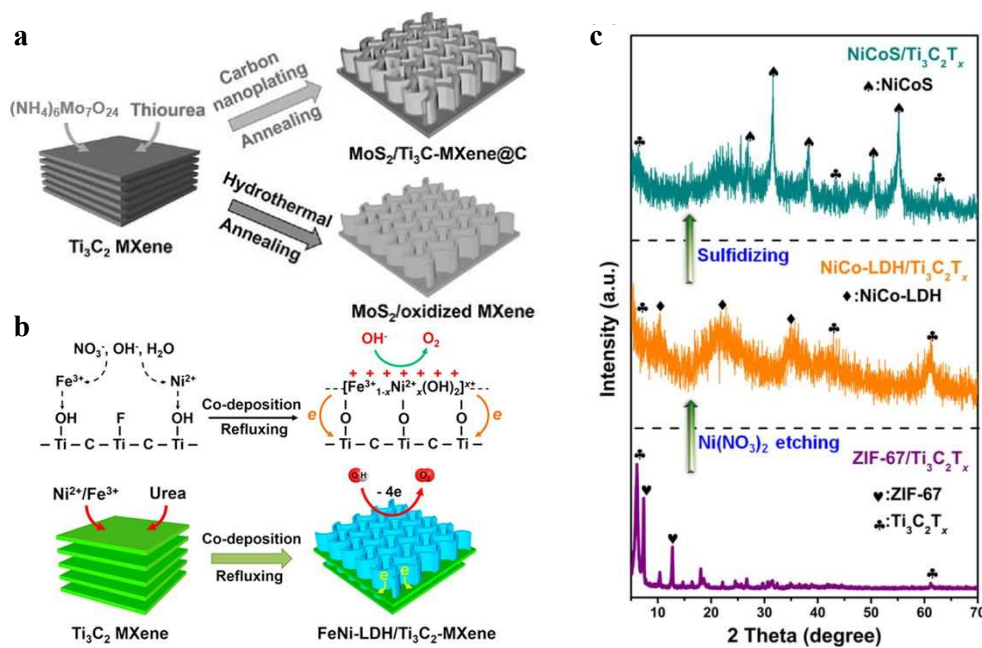
1  
2  
3 ***In-situ* reactive formation of secondary materials onto MXenes to form MXene**  
4 **hybrids.** Compared to *in-situ* conversion of MXene surfaces, this approach allows for the  
5  
6 incorporation of wider material compositions, independent of the MXenes' TM surface identity.  
7  
8 Here, MXenes can be viewed as substrates, not reactants, for secondary material growth. The main  
9  
10 advantage of *in-situ* reactive formation is the preservation of the MXenes' integrity in the synthesis  
11  
12 process, as virtually any precursors (cationic, anionic, or metallic) can be utilized for the nucleation  
13  
14 and growth of the secondary material. With this process, it is possible to form hybrids with high  
15  
16 secondary material to MXene ratios as reported for Bi<sub>2</sub>WO<sub>6</sub>/Ti<sub>3</sub>C<sub>2</sub>T<sub>x</sub> (Bi<sub>2</sub>WO<sub>6</sub> : MXene layer  
17  
18 height ≈3:1)<sup>101</sup> or MoSe<sub>2</sub>/Ti<sub>3</sub>C<sub>2</sub>T<sub>x</sub>.<sup>102</sup> Thus, this strategy is most useful if the secondary material is  
19  
20 catalytically active, since large quantities can be grown on the large surface area of MXenes.  
21  
22 Typical synthesis routes available for this strategy include hydro/solvothermal synthesis,<sup>47,72,103–</sup>  
23  
24 <sup>105</sup> solution processing,<sup>73</sup> and deposition (physical or electro/photo-induced).<sup>74–79</sup> Most of these  
25  
26 synthetic routes, except physical deposition, rely on the van der Waals<sup>53</sup> or ionic/electrostatic<sup>106</sup>  
27  
28 interactions between the negatively charged MXene surfaces (from the T<sub>x</sub> groups) and positively  
29  
30 charged secondary material precursors.<sup>41</sup> After initial adsorption, the secondary materials are  
31  
32 formed *in-situ* onto the MXenes' surface through chemical processing with additional reactants  
33  
34 and/or heat treatment.<sup>101,107</sup>  
35  
36  
37  
38  
39  
40  
41  
42

43 Hydro/solvothermal synthesis exploits the interactions between the liquid solvent,  
44  
45 mineralizer (*e.g.* base), and precursor moieties at elevated temperatures and pressures, mimicking  
46  
47 the processes occurring at the Earth's crust.<sup>108</sup> This synthesis route is a simple and scalable way to  
48  
49 synthesize many different types of secondary materials (**Figure 2**) in various morphologies,<sup>109–111</sup>  
50  
51 and is versatile enough to yield solid solution mixtures<sup>112</sup> or different material allotropes<sup>113</sup> by  
52  
53 carefully tuning the processing conditions. Although hydrothermal synthesis is typically directed  
54  
55  
56  
57  
58  
59  
60

1  
2  
3 at bulk material synthesis, heterogeneous nucleation and epitaxial films can be achieved by adding  
4 suitable substrates.<sup>114,115</sup> A major challenge in this route is aggressive corrosion by water  
5 molecules or –OH moieties at elevated temperatures and pressures, which may induce undesired  
6 damage to the MXenes.<sup>70</sup> This can be partially alleviated by replacing water with non-aqueous  
7 solvents, thus the term solvothermal.<sup>116</sup> Wu *et al.* proposed the addition of glucose to the solvent  
8 to protect MXenes from oxidative damage.<sup>70</sup> During the reaction, glucose molecules were adhered  
9 on MXene surfaces *via* hydrogen bonding and converted to a simple hydrocarbon coating (**Figure**  
10 **4a**), which was subsequently converted to carbon with thermal treatment. The carbon coating was  
11 shown to improve charge transport characteristics and prevent secondary material aggregation.<sup>117</sup>  
12  
13  
14  
15  
16  
17  
18  
19  
20  
21  
22  
23  
24

25 Solution processing at ambient pressure is an alternative to hydro/solvothermal treatment,  
26 since the gentler reaction conditions can reduce unwanted MXene damage.<sup>73</sup> To achieve controlled  
27 growth, metallic precursors are first adsorbed onto MXenes *via* a mixing process. Thereafter,  
28 anionic precursors are introduced to chemically react and form the desired secondary materials on  
29 the MXene surface. An additional annealing step is usually required to complete the reaction and  
30 enhance the integration of the secondary material on MXenes.<sup>118–120</sup> A variety of inorganic  
31 materials such as TM oxides,<sup>121</sup> phosphides,<sup>122</sup> chalcogenides,<sup>118</sup> nitrides,<sup>123</sup> MOFs,<sup>124</sup>  
32 perovskites,<sup>125</sup> and LDHs<sup>109,126</sup> have been hybridized with MXenes this way (**Figure 2**). Yu *et al.*  
33 prepared FeNi-LDH@Ti<sub>3</sub>C<sub>2</sub>T<sub>x</sub> hybrids by the co-precipitation of Fe<sup>3+</sup> and Ni<sup>2+</sup> cations on  
34 negatively charged Ti<sub>3</sub>C<sub>2</sub>T<sub>x</sub> sheets for EC OER (**Figure 4b**).<sup>126</sup> The abundance of –OH and –F  
35 surface groups facilitated the initial electrostatic nucleation and subsequent growth of LDH sheets  
36 on MXenes with minimal oxidation. Additionally, secondary materials that are initially  
37 electrostatically adsorbed and formed on MXene surfaces, can be chemically converted to other  
38 more catalytically active materials.<sup>119,120</sup> For instance, zeolitic imidazolate framework-67 (ZIF-67)  
39  
40  
41  
42  
43  
44  
45  
46  
47  
48  
49  
50  
51  
52  
53  
54  
55  
56  
57  
58  
59  
60

self-assembled on  $\text{Ti}_3\text{C}_2\text{T}_x$  was etched to NiCo-LDH by ultrasonication after the addition of  $\text{Ni}^{2+}$  precursors. Then, heat treatment and sulfidation of the mildly OER-active NiCo-LDH/ $\text{Ti}_3\text{C}_2\text{T}_x$  yielded NiCoS/ $\text{Ti}_3\text{C}_2\text{T}_x$  MXene hybrids with significantly enhanced OER activity (**Figure 4c**).<sup>120</sup>



**Figure 4.** *In-situ* formation of secondary materials on MXenes to form MXene hybrids. (a) Carbon nanoplating to resist MXene oxidation during hydrothermal treatment. Adapted with permission from ref <sup>70</sup>. Copyright 2017 Wiley-VCH. (b) *In-situ* electrostatic self-assembly of FeNi-LDH/ $\text{Ti}_3\text{C}_2\text{T}_x$  hybrid. Adapted with permission from ref <sup>126</sup>. Copyright 2017 Elsevier Ltd. (c) X-ray diffraction (XRD) spectra showing the conversion of ZIF-67/ $\text{Ti}_3\text{C}_2\text{T}_x$  to NiCoS/ $\text{Ti}_3\text{C}_2\text{T}_x$  hybrid. Adapted with permission from ref <sup>120</sup>. Copyright 2018 American Chemical Society.

Finally, MXene hybrids can be formed *via* various deposition methods. Deposition methods are generally non-invasive, controlled, and a more conformal way of fabricating MXene hybrids and heterostructures as compared to the random assembly methods of *in-situ* conversion and self-assembly. Secondary materials have been deposited on MXene surfaces through atomic layer deposition (ALD),<sup>79,127–130</sup> electro-,<sup>76,77,131,132</sup> or photodeposition.<sup>78,133</sup> MXenes have been used as substrates for ALD and chemical vapor deposition (CVD) of secondary material precursors to grow TM oxides,<sup>79</sup> metal NPs,<sup>127</sup> CNTs,<sup>128</sup> and inorganic NPs.<sup>129</sup> These techniques promote strong interfacial bonding due to *in-situ* hybrid formation at elevated temperatures,<sup>128,129</sup> which

1  
2  
3 promotes charge transfer for electrocatalysis.<sup>130</sup> While ALD and CVD are useful for atomic-scale  
4 studies at the MXene hybrid interface,<sup>65</sup> these methods may not be viable to produce hybrids for  
5 electrocatalysis at larger scales due to the cost and difficulty in scaling up.  
6  
7  
8  
9

10 MXene hybrids comprising TM phosphides,<sup>74</sup> oxides,<sup>131</sup> metals,<sup>76</sup> and C-based  
11 materials<sup>77,132</sup> have also been formed through electrodeposition. Electrodeposition can be used to  
12 produce MXene hybrid coatings or electrodes without the use of binders or additives, which can  
13 potentially hinder charge and mass transport during electrocatalysis.<sup>132</sup> In one study, the  
14 conductive  $Ti_3C_2T_x$  film was directly used as a cathode for the deposition of secondary material  
15 precursors.<sup>76</sup> Alternatively, other electrodeposition studies disperse both the MXenes and  
16 secondary material precursors in the electrolyte, and deposit the hybrid onto a conductive electrode  
17 such as nickel foam,<sup>131</sup> graphite paper<sup>132</sup> or nickel plate.<sup>74</sup> Specifically,  $-OH$  surface groups on  
18  $Ti_3C_2T_x$  have been demonstrated to improve the adsorption of  $Sn^{4+}$  and  $Pb^{2+}$ ,<sup>134,135</sup> which presents  
19 the possibility of tuning the  $T_x$  composition to selectively favor the electrodeposition of specific  
20 metallic precursors. Complementary to electrodeposition, photodeposition was used to reduce  
21 metallic ions to deposit metallic NPs such as  $Cu^{78}$  and  $Pt^{133}$  *in-situ* onto MXene surfaces.  
22 Photodeposition possesses an advantage over other deposition methods in that it can be used to  
23 target specific areas or facets where photo-generated electrons accumulate.<sup>136</sup> However, the light  
24 intensity must be controlled carefully, as very intense light irradiation has been shown to oxidize  
25 and degrade MXenes.<sup>137,138</sup>  
26  
27  
28  
29  
30  
31  
32  
33  
34  
35  
36  
37  
38  
39  
40  
41  
42  
43  
44  
45  
46  
47

#### 48 **Non-reactive assembly of secondary materials onto MXenes to form MXene hybrids.**

49 Secondary materials with a positive surface charge can also be easily combined with MXenes to  
50 form MXene hybrids through physical processes such as drop-casting<sup>80</sup> and adsorption.<sup>56</sup> This  
51 method also relies on the same electrostatic/van der Waals self-assembly principle as the previous  
52  
53  
54  
55  
56  
57  
58  
59  
60



1  
2  
3 method (reactive chemical formation of secondary materials on MXenes). However, in this non-  
4 reactive method, the secondary materials are in the final forms *prior* to integration with MXenes.  
5 Hence, the MXenes are typically not subjected to high temperature treatment steps such as  
6 hydro/solvothermal treatment for secondary material integration. This method is most suitable for  
7 ambient-stable secondary materials that can be easily solution-processed.  
8  
9

10  
11  
12 Adsorption of C-based materials such as *g*-C<sub>3</sub>N<sub>4</sub>,<sup>133,139</sup> CNTs,<sup>56,140,141</sup> graphene oxide  
13 (GO), and reduced graphene oxide (rGO)<sup>61,142</sup> is commonly used for the assembly of MXene/C-  
14 based material hybrids. CNTs are often mixed with MXenes by sonication,<sup>56,140</sup> while *g*-C<sub>3</sub>N<sub>4</sub>, GO,  
15 and rGO are electrostatically adsorbed.<sup>143,144</sup> MXene hybrids with CNTs, *g*-C<sub>3</sub>N<sub>4</sub>, and GO/rGO are  
16 then traditionally filtered to yield free standing films for electrode applications and  
17 capacitors.<sup>139,141,145</sup> After the adsorption process, MXene hybrids with CNTs and GO/rGO can be  
18 further freeze-dried to form conductive aerogel networks for capacitors.<sup>61,140,142</sup> Generally,  
19 MXene/*g*-C<sub>3</sub>N<sub>4</sub> hybrids promote electron transfer at the interface to augment the catalytic activity  
20 of *g*-C<sub>3</sub>N<sub>4</sub>,<sup>133,143</sup> while CNTs, GO, and rGO on MXenes serve as additional conductive and/or  
21 structural supports.<sup>146</sup> Other secondary materials such as TM oxides,<sup>121</sup> phosphates,<sup>122</sup>  
22 chalcogenides,<sup>118</sup> nitrides,<sup>123</sup> MOFs<sup>107</sup> and LDHs<sup>109</sup> can also be combined with MXenes this way.  
23  
24  
25  
26  
27  
28  
29  
30  
31  
32  
33  
34  
35  
36  
37  
38  
39  
40

41  
42 MXene hybrids have also been formed by drop-casting MXenes onto the secondary  
43 material (or *vice versa*).<sup>80,147</sup> For example, TiO<sub>2</sub> nanorods were grown hydrothermally on a  
44 fluorine-doped tin oxide (FTO) substrate, and then coated with Ti<sub>3</sub>C<sub>2</sub>T<sub>x</sub> through solution drop  
45 casting to produce the Ti<sub>3</sub>C<sub>2</sub>T<sub>x</sub>/TiO<sub>2</sub>/FTO photoanode for PEC water splitting.<sup>80</sup> While drop-  
46 casting is a less-intensive process, post-processing steps such as annealing may be required to  
47 optimize MXene-secondary material interfacial chemical bonding and charge transfer.  
48  
49  
50  
51  
52  
53  
54  
55  
56  
57  
58  
59  
60

1  
2  
3       **Summary, specific challenges, and outlook for processing of MXene hybrids.** We have  
4 described how MXene hybrids can be formed through (1) *in-situ* conversion by using MXene  
5 surfaces as reactants, (2) direct chemical growth of secondary materials on MXenes, and (3)  
6 deposition of secondary materials on MXenes. The processing method employed for MXene  
7 hybrids formation is highly dependent on their intended catalytic application. For instance, PC  
8 applications require semiconducting photo-absorbers, which can be formed *via in-situ* oxidation  
9 or hydro/solvothermal treatment of Ti-based MXenes.<sup>89</sup> In contrast, oxide formation on MXenes  
10 is detrimental to electrocatalysis, as oxides are less conductive and limit charge transport  
11 properties,<sup>148</sup> so a self-assembly process may be more appropriate. MXene hybrids should also be  
12 carefully designed to optimize chemical coupling at the MXene-secondary material interfaces  
13 toward catalytic activity enhancement. For example, strong chemical coupling between  $Ti_3C_2T_x$   
14 with *g*- $C_3N_4$  afforded a highly OER-active hybrid.<sup>139</sup> A strongly coupled MXene hybrid also  
15 reduces the probability of hybrid disintegration during electrocatalysis.<sup>149</sup> Finally, the surface  
16 chemistry of MXene  $T_x$  groups play an important role in determining the morphology, phase, and  
17 growth characteristics of secondary materials in the various synthesis methods.<sup>83,87,95</sup> Since the  
18 presence of termination groups on MXene surfaces is dependent on the synthesis processes,<sup>150</sup> it  
19 is thus crucial to carefully select the route of MXene synthesis, as well as the subsequent treatment  
20 steps, to develop MXene hybrids with high catalytic activity and structural stability.  
21  
22  
23  
24  
25  
26  
27  
28  
29  
30  
31  
32  
33  
34  
35  
36  
37  
38  
39  
40  
41  
42  
43  
44  
45  
46  
47  
48  
49  
50  
51  
52  
53  
54  
55  
56  
57  
58  
59  
60

## MXENE HYBRIDS FOR WATER SPLITTING REACTIONS

MXenes' unique set of physical and electronic properties make them excellent candidates for catalytic water splitting.<sup>13–15</sup> High hydrophilicity and solution processability allow MXenes to be robust and durable in aqueous electrolytes such as acids, bases, and seawater.<sup>151</sup> Metallic electronic conductivity enables MXenes to facilitate efficient electronic charge transport at the electrode-electrolyte interface as a large-area conductive 2D substrate when coupled to other highly active but less conductive co-catalysts.<sup>42,152</sup> This combination of properties circumvent the limitations of conventional C-based supports such as graphene whose hydrophobicity restricts their use in aqueous electrocatalysis, and GO whose conductivity is reduced because of hydroxyl functionalization.<sup>126,153</sup> Hybridization also creates additional catalytically active motifs at the interface<sup>139</sup> and modulates the electronic structure to augment intrinsic catalytic activity.<sup>126,153</sup> With precise control over the MXene hybrid's interfaces and growth of secondary materials, bifunctional non-PGM MXene hybrid couples have outperformed full PGM couples (Pt/C as HER cathode, RuO<sub>2</sub> or IrO<sub>2</sub> as OER anode) in both activity and stability.<sup>102,149</sup> Here, we highlight highly active and non-PGM HER, OER, and bifunctional water splitting MXene hybrid catalysts, clarifying the roles played by each material component in the overall catalyst design. For the reader's benefit, a summary table of performance metrics for various MXene hybrids in EC HER/OER and PC/PEC HER is provided in **Tables S2 and S3** respectively.

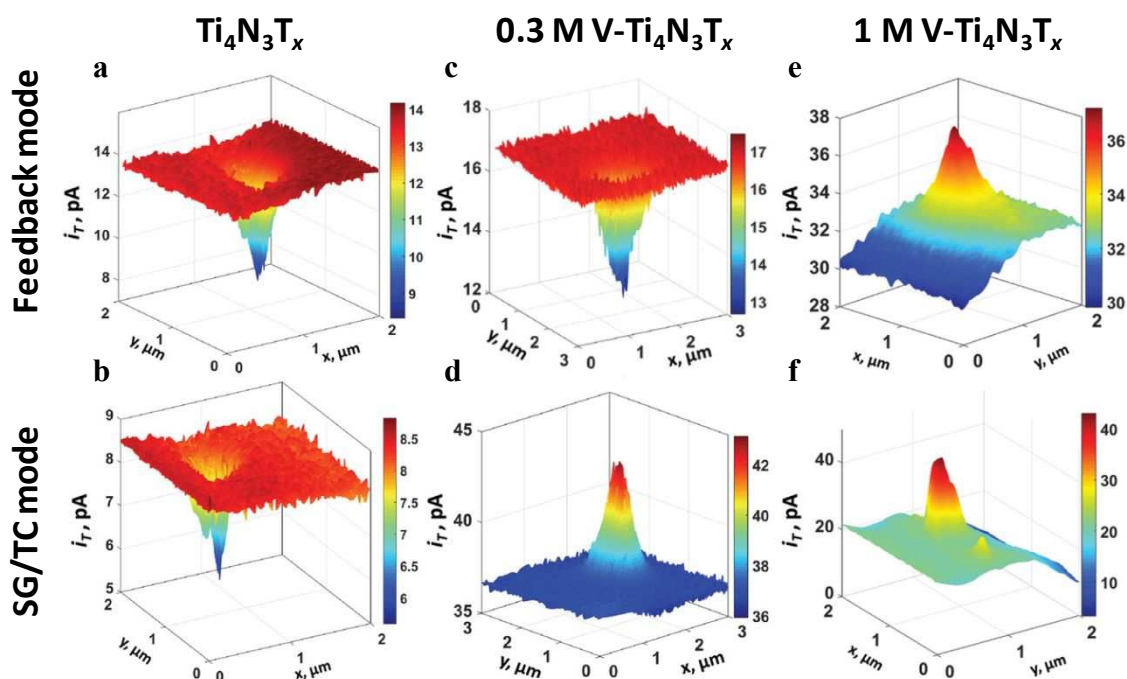
**MXene hybrids and composites for electrocatalytic (EC) HER.** MXenes have garnered significant attention after they were theoretically predicted<sup>154–156</sup> and then demonstrated to be HER-active.<sup>17</sup> Unlike other 2D materials like 2H-MoS<sub>2</sub> that exhibit higher catalytic activity on the edges,<sup>20</sup> the 2D basal planes of MXenes are more HER active,<sup>17–19</sup> allowing for more efficient catalyst utilization. HER activity in bare MXenes was reported experimentally using Mo<sub>2</sub>CT<sub>x</sub> and

1  
2  
3  $\text{Ti}_2\text{CT}_x$  by Seh *et al.*, with the  $-\text{O T}_x$  surface groups determined as active sites on the MXenes' basal planes.<sup>17</sup> Due to the modest EC HER activity of bare MXenes, initial efforts were directed at improving their HER activity through physically increasing the density of electrochemically active surface area (ECSA) by nanostructuring,<sup>157,158</sup> or by modulating the MXene electronic structure to achieve a more thermoneutral  $^*\text{H}$  adsorption free energy ( $\Delta G_{\text{H}} \rightarrow 0$ ), a common predictor for HER activity.<sup>154-156</sup> Effective binding energy tuning may be achieved through  $\text{T}_x$  control,<sup>18,154</sup> and doping with other TMs<sup>127,159-162</sup> and/or non-metals (such as N, S, and P).<sup>163-165</sup>

19  
20 The effect of TM doping in changing  $^*\text{H}$  binding energy was recently illustrated by Djire *et al.* using scanning electrochemical microscopy (SECM) on  $\text{Ti}_4\text{N}_3\text{T}_x$  MXenes.<sup>19</sup> SECM is a unique tool capable of generating high-resolution local conductivity and EC activity maps of the catalyst surface. In the feedback mode, ferrocene (Fc), a redox mediator, is included to probe the surface conductivity. A higher tip current ( $i_T$ ) will be observed on a more conductive surface due to a faster rate of  $\text{Fc}^+$  reduction. As the MXene flakes are placed on top of a conductive substrate like indium tin oxide (ITO),  $i_T$  contrast also demarcates the boundaries of the MXene flake edges. The HER activity can be mapped by applying a negative bias to the substrate, referred to as the substrate generation/tip collection (SG/TC) mode.

41 Alloying  $\text{Ti}_4\text{N}_3\text{T}_x$  with V, which produced V-alloyed  $\text{Ti}_4\text{N}_3\text{T}_x$  (denoted as y M V- $\text{Ti}_4\text{N}_3\text{T}_x$ , where y = molar concentration of aqueous  $\text{VO}_2^+$  dopant used for alloying), did not improve the surface conductivity, as shown by the negligible  $i_T$  in 0.3 M V- $\text{Ti}_4\text{N}_3\text{T}_x$ , similar to bare  $\text{Ti}_4\text{N}_3\text{T}_x$  (**Figures 5a** and **5c**). However, the HER activity in V-alloyed  $\text{Ti}_4\text{N}_3\text{T}_x$  increased very significantly compared to the bare MXenes (**Figures 5b** and **5d**). Improved conductivity in V- $\text{Ti}_4\text{N}_3\text{T}_x$  was also be achieved by increasing the concentration of  $\text{VO}_2^+$  dopant used (**Figure 5e**) and was accompanied by a slight improvement in HER activity (**Figure 5f**). This study by Djire *et al.* is

1  
2  
3 experimental proof of basal plane HER activity in MXenes, as inferred from the lower  $i_T$  around  
4 the flake edges in the SG/TC mode. Furthermore, it demonstrates that the conductivity and HER  
5 activity in MXenes may be decoupled, possibly due to the self-gating phenomenon, reported  
6 activity in MXenes may be decoupled, possibly due to the self-gating phenomenon, reported  
7 previously on the basal planes of a variety of semiconducting 2D materials, including 2H-MoS<sub>2</sub>.<sup>166</sup>  
8  
9  
10  
11  
12



13  
14  
15  
16  
17  
18  
19  
20  
21  
22  
23  
24  
25  
26  
27  
28  
29  
30  
31  
32  
33  
34  
35 **Figure 5.** SECM feedback mode and SG/TC mapping of (a, b) bare Ti<sub>4</sub>N<sub>3</sub>T<sub>x</sub> and V-alloyed  
36 Ti<sub>4</sub>N<sub>3</sub>T<sub>x</sub>, using (c, d) 0.3 M or (e, f) 1.0 M aqueous VOSO<sub>4</sub> dopant for alloying. Adapted with  
37 permission from ref<sup>19</sup>. Copyright 2020 WILEY-VCH.  
38

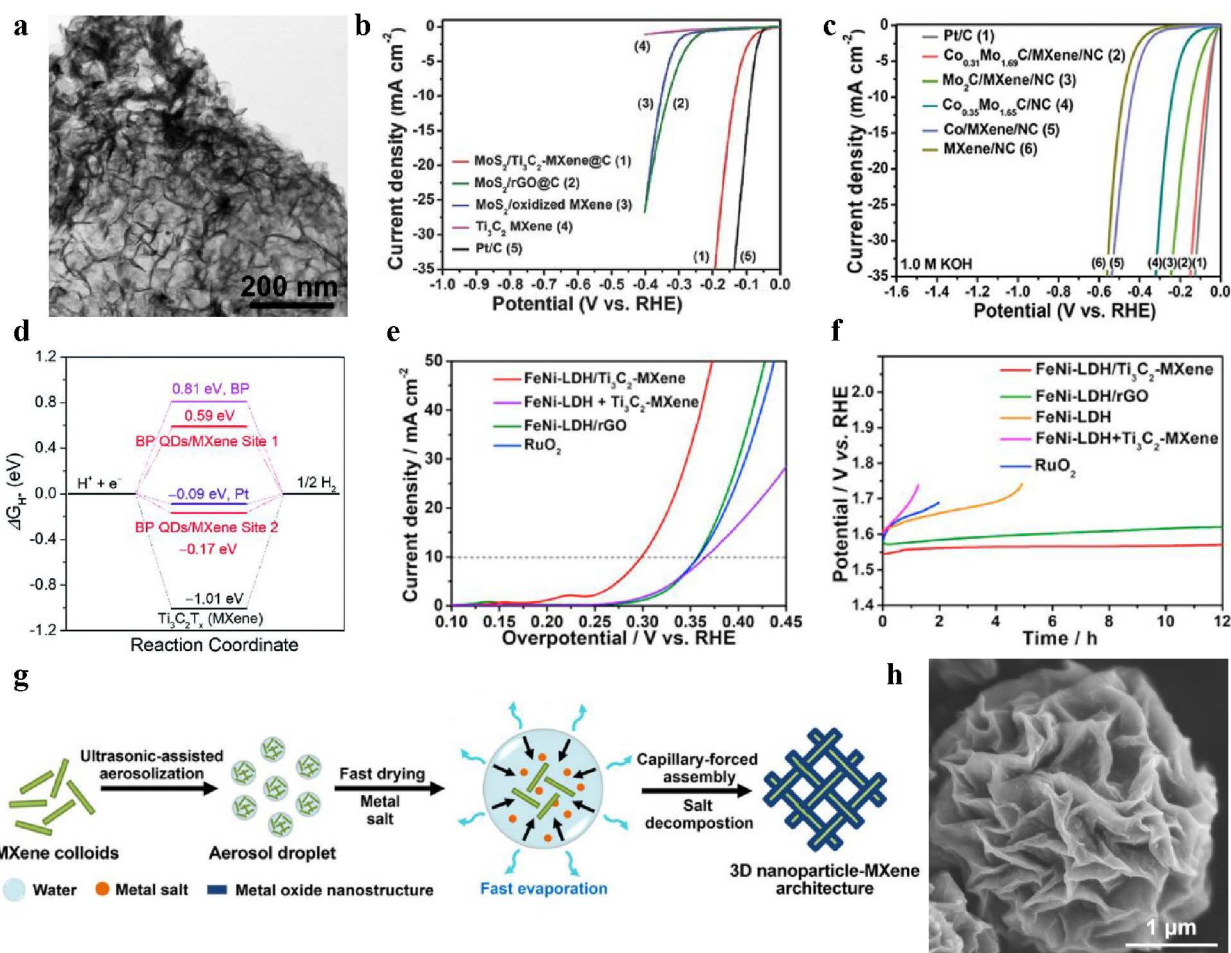
39  
40 Coupling MXenes with other HER-active co-catalysts such as TM chalcogenides,<sup>102,167</sup>  
41 phosphides,<sup>168–170</sup> carbides,<sup>151,171</sup> and QDs (metallic alloys and black phosphorus, BP) are  
42 common ways to enhance HER activity.<sup>52,53</sup> Here, MXenes serve as a large-area conductive and  
43 mechanical support to facilitate charge transfer, act as a HER co-catalyst, and modulate the  
44 hybrid's electronic structure to optimize for H<sup>+</sup> adsorption and HER activity. With significantly  
45 higher HER activities than the sum of their individual material components, intimately coupled  
46 MXene hybrids benefit from synergistic HER enhancement to achieve PGM-like activities.  
47  
48  
49  
50  
51  
52  
53  
54  
55  
56  
57  
58  
59  
60

Coupling MXenes with TM chalcogenides for EC HER was reported by Wu *et al.* in a hierarchical MoS<sub>2</sub>/Ti<sub>3</sub>C<sub>2</sub>T<sub>x</sub>@C architecture (**Figure 4a**).<sup>70</sup> The MXene support constrained 2H-MoS<sub>2</sub> to grow vertically,<sup>172,173</sup> maximizing ECSA and mass transport of gaseous products (**Figure 6a**). The strong interfacial and chemical relationship between Ti<sub>3</sub>C<sub>2</sub>T<sub>x</sub> and 2H-MoS<sub>2</sub> was verified by the Mo (MoS<sub>2</sub>)-C (MXene) X-ray photoelectron spectroscopy (XPS) peak, which would be absent in a physical mixture of Ti<sub>3</sub>C<sub>2</sub>T<sub>x</sub> and 2H-MoS<sub>2</sub>. With a small charge transfer resistance of 1.28 Ω, MoS<sub>2</sub>/Ti<sub>3</sub>C<sub>2</sub>T<sub>x</sub>@C required a small overpotential ( $\eta_{j=10}$ ) of 135 mV at a current density of -10 mA cm<sup>-2</sup> in 0.5 M H<sub>2</sub>SO<sub>4</sub>, 217 mV smaller than the MoS<sub>2</sub>/rGO@C hybrid when rGO is used as the substrate (curves 1 and 2, **Figure 6b**, see **Vocabulary** for a definition of overpotential and Tafel slope).<sup>70</sup> The nanohybrids were also durable in acid for 20 h of operation at -130 mV (*vs.* reversible hydrogen electrode, RHE), due to the protective carbon nanoplating surrounding the hybrid. Additionally, coupling other TM chalcogenides such as MoS<sub>2</sub>,<sup>118</sup> MoSe<sub>2</sub>,<sup>102</sup> NiS<sub>2</sub>,<sup>174</sup> NiSe<sub>2</sub>,<sup>175</sup> and VS<sub>2</sub><sup>176</sup> to various MXenes have also achieved synergistically enhanced HER activity.

TM carbides<sup>151,171</sup> and phosphides<sup>168-170</sup> have also been integrated into MXene hybrids for EC HER. TM phosphides will be discussed in the next sub-section due to their HER and OER bifunctionality. A collaborative catalytic interface was formed between the cobalt-doped β-Mo<sub>2</sub>C co-catalyst, Ti<sub>3</sub>C<sub>2</sub>T<sub>x</sub>, and N-doped carbon (NC) to enhance electrical conductivity and expose ECSA, while improving H<sup>+</sup> and water absorption kinetics for efficient HER in a wide pH range, including in seawater.<sup>151</sup> Theoretical calculations revealed that the Co<sub>x</sub>Mo<sub>2-x</sub>C/NC interface reduced the H<sup>+</sup> absorption barrier to 0.05 eV, and the water dissociation barrier to 0.78 eV. Notably, the water dissociation barrier was lower than Pt (111) at 0.89 eV. With accelerated water dissociation and HER kinetics, the optimized Co<sub>0.31</sub>Mo<sub>1.69</sub>C/MXene/NC hybrid exhibited Pt-like HER activity with an  $\eta_{j=10}$  and Tafel slope of 75 mV and 32 mV dec<sup>-1</sup>, respectively, in 1 M KOH

1  
2  
3 (curve 2, **Figure 6c**), outperforming the individual  $\beta$ -Mo<sub>2</sub>C and MXene components (curves 4 and  
4  
5 **6, Figure 6c**). This corroborated with a separate report on Mo<sub>2</sub>C/Ti<sub>3</sub>C<sub>2</sub>T<sub>x</sub>@NC, whose exchange  
6  
7 current density ( $j_0$ ) in acid was four-fold higher than Mo<sub>2</sub>C@NC without the MXene support.<sup>171</sup>  
8  
9  
10 These works demonstrate the synergistic co-operation between material components, with  $\beta$ -Mo<sub>2</sub>C  
11  
12 and NC providing favorable H<sup>+</sup> adsorption sites,<sup>151</sup> while MXenes facilitated charge transport.<sup>171</sup>  
13  
14

15  
16 QDs have also been anchored on MXenes to modulate the electronic structure or alter the  
17  
18 adsorption kinetics of intermediates. Du *et al.* modified the Ti<sub>3</sub>C<sub>2</sub>T<sub>x</sub> surface with Ni/Co alloyed  
19  
20 QDs to reduce the overly strong Ti-H interaction.<sup>177</sup> Nb was also doped into Ti<sub>3</sub>C<sub>2</sub>T<sub>x</sub> to raise the  
21  
22 Fermi level to the conduction band, improving the electronic conductivity of the Ti<sub>3</sub>C<sub>2</sub>T<sub>x</sub> support.  
23  
24 The optimized Ni<sub>0.9</sub>Co<sub>0.1</sub>@Ti<sub>2.5</sub>Nb<sub>0.5</sub>C<sub>2</sub>T<sub>x</sub> hybrid showed  $\eta_{j=10}$  of 43 mV for HER, a significant  
25  
26 improvement compared to the 516 mV required for Ti<sub>2.5</sub>Nb<sub>0.5</sub>C<sub>2</sub>T<sub>x</sub> without the alloyed QDs.  
27  
28 Critically, the HER enhancement was intrinsic, given that the HER improvement trends were still  
29  
30 valid after normalization for ECSA. Separately, BP QDs were decorated on Ti<sub>3</sub>C<sub>2</sub>T<sub>x</sub> to similarly  
31  
32 reduce Ti<sub>3</sub>C<sub>2</sub>T<sub>x</sub> surface binding to H<sup>+</sup> from -1.01 eV to as low as -0.17 eV (**Figure 6d**).<sup>53</sup>  
33  
34  
35 Beneficially, the MXene support physically confined the growth of BP to discrete 0D QDs, which  
36  
37 prevented agglomeration, and maximized ECSA and mass transport for electrocatalysis.<sup>52,53</sup>  
38  
39  
40  
41  
42  
43  
44  
45  
46  
47  
48  
49  
50  
51  
52  
53  
54  
55  
56  
57  
58  
59  
60



**Figure 6.** MXene hybrids for EC water splitting. (a) TEM image and (b) polarization curves of MoS<sub>2</sub>/Ti<sub>3</sub>C<sub>2</sub>T<sub>x</sub>-MXene@C, showing vertical growth of MoS<sub>2</sub> on Ti<sub>3</sub>C<sub>2</sub>T<sub>x</sub>. Adapted with permission from ref <sup>70</sup>. Copyright 2017 WILEY-VCH. (c) Polarization curves of Co<sub>x</sub>Mo<sub>2-x</sub>C/MXene/NC. Adapted with permission from ref <sup>151</sup>. Copyright 2019 WILEY-VCH. (d) Free energy diagram of BP QDs/Ti<sub>3</sub>C<sub>2</sub>T<sub>x</sub>. Adapted with permission from ref <sup>53</sup>. Copyright 2018 Royal Society of Chemistry. (e) Polarization curves and (f) Constant current (-10 mA cm<sup>-2</sup>) stability test of FeNi-LDH/Ti<sub>3</sub>C<sub>2</sub>T<sub>x</sub>-MXene. Adapted with permission from ref <sup>126</sup>. Copyright 2017 Elsevier Ltd. (g) Assembly and (h) Scanning electron microscope (SEM) image of 3D CoP-MXene. Adapted with permission from ref <sup>169</sup>. Copyright 2018 American Chemical Society.

### MXene hybrids and composites for electrocatalytic (EC) OER and water splitting.

Compared to HER, OER is a more complex reaction as it involves a four-electron transfer process and multiple reaction intermediates. Achieving efficient and durable OER often require electrocatalysts with intricate heterostructuring and design.<sup>178</sup> Although bare MXenes are not efficient OER catalysts,<sup>45</sup> they can serve as electrically conductive supports, modulate the



1  
2  
3 electronic density of their coupled OER co-catalyst, and even create additional OER-active motifs  
4 to greatly enhance OER activity.<sup>44,139</sup> For instance, coupling  $\text{Ti}_3\text{C}_2\text{T}_x$  with  $g\text{-C}_3\text{N}_4$  created a highly  
5 OER-active Ti (MXene)- $\text{N}_x$  ( $g\text{-C}_3\text{N}_4$ ) motif at the interface for PGM-like OER activity.<sup>139</sup> Many  
6 OER-active materials such as TM chalcogenides,<sup>102,120</sup> oxides,<sup>131,179</sup> nitrides,<sup>180</sup> phosphides,<sup>168–170</sup>  
7 MOFs,<sup>107</sup> LDHs,<sup>126,153,181</sup> C-based materials,<sup>139,182</sup> and QDs<sup>53,183</sup> have been coupled with MXenes  
8 to augment OER activity. More significantly, these strategies have yielded non-PGM MXene  
9 hybrids that have outperformed PGM-based electrocatalysts for EC OER and water splitting.  
10  
11  
12  
13  
14  
15  
16  
17  
18  
19

20 Heterostructured and hybrid materials are often subject to lattice mismatch and strain at the  
21 interface, which has been exploited in phase engineering to alter electronic states near the interface  
22 and stabilize metastable material phases.<sup>184,185</sup> Li *et al.* stabilized a mixture of metastable 1T (23%)  
23 and stable 2H (77%)  $\text{MoSe}_2$  on  $\text{Ti}_3\text{C}_2\text{T}_x$  as a bifunctional HER and OER electrocatalyst.<sup>102</sup> The  
24 1T/2H  $\text{MoSe}_2$ /MXene hybrid (HER  $\eta_{j=10} = 95$  mV) outperformed their individual components and  
25 other phases (2H  $\text{MoSe}_2$ /MXene HER  $\eta_{j=10} = 123$  mV) for both HER and OER. The non-PGM  
26 1T/2H  $\text{MoSe}_2$ /MXene couple also required a modest 1.64 V (*vs.* RHE) to maintain a current  
27 density of  $-10$  mA  $\text{cm}^{-2}$  for 50 h while retaining a high 1T phase content. The activity improvement  
28 was attributed to the use of conductive MXenes to improve charge transfer and confine the 1T/2H  
29  $\text{MoSe}_2$  nanostructures to prevent aggregation. The intrinsic activity of  $\text{MoSe}_2$  was also boosted by  
30 the abundance of  $\text{MoSe}_2$  active sites, particularly from the more catalytically active and now  
31 stabilized 1T phase. This work illustrates the potential of using MXenes to stabilize metastable  
32 phases that are highly electrocatalytically active, as co-catalysts to achieve higher activities.<sup>102</sup>  
33  
34  
35  
36  
37  
38  
39  
40  
41  
42  
43  
44  
45  
46  
47  
48  
49

50 Although LDHs are excellent candidates for alkaline OER and water splitting, they are  
51 poor electrical conductors and aggregate easily.<sup>126,153,181</sup> Previously, LDHs were used with C-based  
52 supports such as graphene to improve charge transport. These C-based supports, however, had to  
53  
54  
55  
56  
57  
58  
59  
60

1  
2  
3 be first functionalized to rGO/GO before they could be integrated with LDHs, compromising the  
4 support's structural integrity and conductivity. Therefore, Yu *et al.* exploited the negatively  
5 charged surface  $T_x$  groups of MXenes to electrostatically self-assemble FeNi-LDH nanostructures  
6 vertically on  $Ti_3C_2T_x$  in a 3D array (**Figure 4b**).<sup>126</sup> The vertical growth of LDH atop MXenes  
7 reduced repulsion and aggregation between positively charged LDH sheets while maximizing  
8 ECSA for catalysis.<sup>153,181</sup> The benefits of strong chemical coupling within the hybrid was evident  
9 in their OER performance (**Figure 6e**) and stability (**Figure 6f**), which are far superior to the  
10 physical mixture (FeNi-LDH +  $Ti_3C_2T_x$ ) or when the FeNi-LDH OER catalyst was hybridized with  
11 a less conductive substrate (FeNi-LDH/rGO) instead of MXenes. The reasoning for the enhanced  
12 OER is attributed to the increased oxidation state of Ni and Fe centers after hybridization, as shown  
13 in the +0.5 eV shift of the Ni and Fe 2p XPS peaks.<sup>126</sup> A follow-up work integrated the FeNi-  
14 LDH/ $Ti_3C_2T_x$  structure with a 3D nickel foam network to further maximize ECSA and mass  
15 transport, achieving a high current density of 500 mA cm<sup>-2</sup> at very low overpotentials for alkaline  
16 OER (300 mV), HER (205 mV), and bifunctional water splitting (1.75 V vs. RHE).<sup>149</sup> Separately,  
17 extensive growth of Co-LDH on  $Ti_3C_2T_x$  was successful in arresting  $Ti_3C_2T_x$  surface oxidation  
18 during OER, which would have impeded both charge transfer at the MXene-LDH interface, and  
19 overall electronic conductivity in the hybrid.<sup>186</sup>

20  
21  
22  
23  
24  
25  
26  
27  
28  
29  
30  
31  
32  
33  
34  
35  
36  
37  
38  
39  
40  
41  
42  
43 The LDH-MXene hybrids can also be processed further to form bifunctional catalysts like  
44 phospho-sulfides. For example, FeNi-LDH/MXenes can be converted to 2D bimetallic  $Ni_xFe_{1-x}$   
45  $PS_3$  ( $MPS_3$ )/MXenes hybrid *via* thermal annealing with red phosphorus in a vacuum sealed  
46 ampule.<sup>167</sup> The resulting  $MPS_3$ /MXenes hybrid possess a broken-up nanomosaic morphology with  
47 high ECSA, possibly due to the thermal stress. More importantly, the  $MPS_3$ /MXenes composition  
48 can be easily tailored by tuning the starting Fe : Ni ratio in the FeNi-LDH/MXenes precursor.

1  
2  
3 Interestingly, the catalytic reaction preference of MPS<sub>3</sub> hybrids depends on its Fe : Ni ratio –  
4 Ni<sub>0.9</sub>Fe<sub>0.1</sub>PS<sub>3</sub>/Ti<sub>3</sub>C<sub>2</sub>T<sub>x</sub> was found to be most proficient in catalyzing HER ( $\eta_{j=10} = 196$  mV) in 1 M  
5  
6 KOH, while Ni<sub>0.7</sub>Fe<sub>0.3</sub>PS<sub>3</sub>/Ti<sub>3</sub>C<sub>2</sub>T<sub>x</sub> exhibited excellent OER activity ( $\eta_{j=10} = 282$  mV). The  
7  
8 Ni<sub>0.7</sub>Fe<sub>0.3</sub>PS<sub>3</sub>/Ti<sub>3</sub>C<sub>2</sub>T<sub>x</sub> (OER) || Ni<sub>0.9</sub>Fe<sub>0.1</sub>PS<sub>3</sub>/Ti<sub>3</sub>C<sub>2</sub>T<sub>x</sub> (HER) couple can deliver -10 mA cm<sup>-2</sup> of  
9  
10 complete water splitting at a lower potential (1.65 V vs. RHE) than the full-PGM IrO<sub>2</sub> || Pt/C  
11  
12 reference standard (1.71 V vs. RHE). The MPS<sub>3</sub>/MXenes couple was also stable for over 50 h at  
13  
14 the said potential. This work demonstrates strain engineering for ECSA maximization, and the  
15  
16 added flexibility of tuning multi-metal compounds to optimize toward different electrochemical  
17  
18 reactions of interest as multi-functional electrocatalysts.  
19  
20  
21  
22  
23

24  
25 TM phosphides have also been integrated with MXenes as bifunctional HER and OER  
26  
27 electrocatalysts.<sup>168–170</sup> Xiu *et al.* reported a hierarchical CoP@3D Ti<sub>3</sub>C<sub>2</sub>T<sub>x</sub>-MXene architecture to  
28  
29 significantly enhance EC activity for water splitting.<sup>169</sup> After nebulizing MXene colloids  
30  
31 containing cobalt salts into tiny droplets, the droplets were dried rapidly at 600 °C. Solvent  
32  
33 evaporation induced an inward capillary force on the droplets to cause isotropic compression of  
34  
35 MXene sheets into aggregation-resistant Co<sub>3</sub>O<sub>4</sub>@3D Ti<sub>3</sub>C<sub>2</sub>T<sub>x</sub>-MXene hybrids (**Figure 6g**). Further  
36  
37 phosphorization converted Co<sub>3</sub>O<sub>4</sub> in the hybrids into OER-active CoP. The highly porous and  
38  
39 interconnected 3D MXene architecture (**Figure 6h**) provided a large surface area for catalysis and  
40  
41 facilitated long-range electrical charge transport. An efficient bifunctional HER and OER  
42  
43 electrocatalyst, CoP@3D Ti<sub>3</sub>C<sub>2</sub>T<sub>x</sub>-MXene required only 1.565 V (vs. RHE) to supply -10 mA cm<sup>-2</sup>  
44  
45 of current density and remained stable (< 25 mV degradation) for 150 h at a high current density  
46  
47 of -100 mA cm<sup>-2</sup>. Combining TM phosphides with MXenes is also reported to shift the TM *d*-band  
48  
49 center to higher energies, resulting in reduced occupancy of antibonding states from the TM and  
50  
51 adsorbed O intermediate, for enhanced OH<sup>-</sup> adsorption and OER.<sup>168</sup> Additionally, 1D CoP  
52  
53  
54  
55  
56  
57  
58  
59  
60

1  
2  
3 nanorods grown on top of  $\text{Ti}_3\text{C}_2\text{T}_x$  sheets was also reported to induce tensile stress and bending of  
4  
5  $\text{Ti}_3\text{C}_2\text{T}_x$  to expose higher ECSA for improved OER activity.<sup>170</sup>  
6  
7

8  
9 **MXene hybrids and composites for photocatalytic (PC) and photoelectrocatalytic (PEC)**  
10 **water splitting.** Given the close alignment of the MXenes' Fermi energy ( $E_F$ ) position to the  $\text{H}^+/\text{H}_2$   
11 reduction potential,<sup>187</sup> efficient  $\text{H}^+$  adsorption, and respectable EC water splitting performances as  
12 described earlier, MXene hybrids are a logical choice for PC/PEC water splitting to harvest  
13 sunlight as a renewable energy driving source. Unlike EC, PC reactions require semiconductor  
14 photo-absorbers, where electron-hole pairs are generated. Since most MXenes are metallic and not  
15 semiconducting,<sup>152</sup> other materials are necessarily drafted to harvest light and promote the  
16 separation of photo-generated carriers.<sup>188</sup> A few works feature MXene hybrids as multi-functional  
17 PEC HER, OER, and water splitting catalysts. Lin *et al.* reported a  $\text{Ti}_3\text{C}_2\text{T}_x/\text{InGaN}$  photo-anode  
18 with a 10-fold improvement in HER photocurrent density after MXene hybridization, verifying  
19 the high HER activity on the MXene surface.<sup>189</sup>  $\text{Ti}_3\text{C}_2\text{T}_x/\text{TiO}_2/\text{NiFeCo-LDH}$  was also tested for  
20 PEC OER, with the MXene and NiFeCo-LDH acting as the conductive support and OER catalyst,  
21 respectively.<sup>181</sup> Yu *et al.* reported  $\text{Ti}_3\text{C}_2\text{T}_x/\text{TiO}_2$  as an OER photo-anode with a six-fold increment  
22 in applied bias photon-to-current efficiency compared to a bare  $\text{TiO}_2$  photoanode.<sup>80</sup> Here, PEC  
23 OER occurred on the MXene surface, which served as a hole scavenger and OER active site.  
24  
25  
26  
27  
28  
29  
30  
31  
32  
33  
34  
35  
36  
37  
38  
39  
40  
41  
42  
43

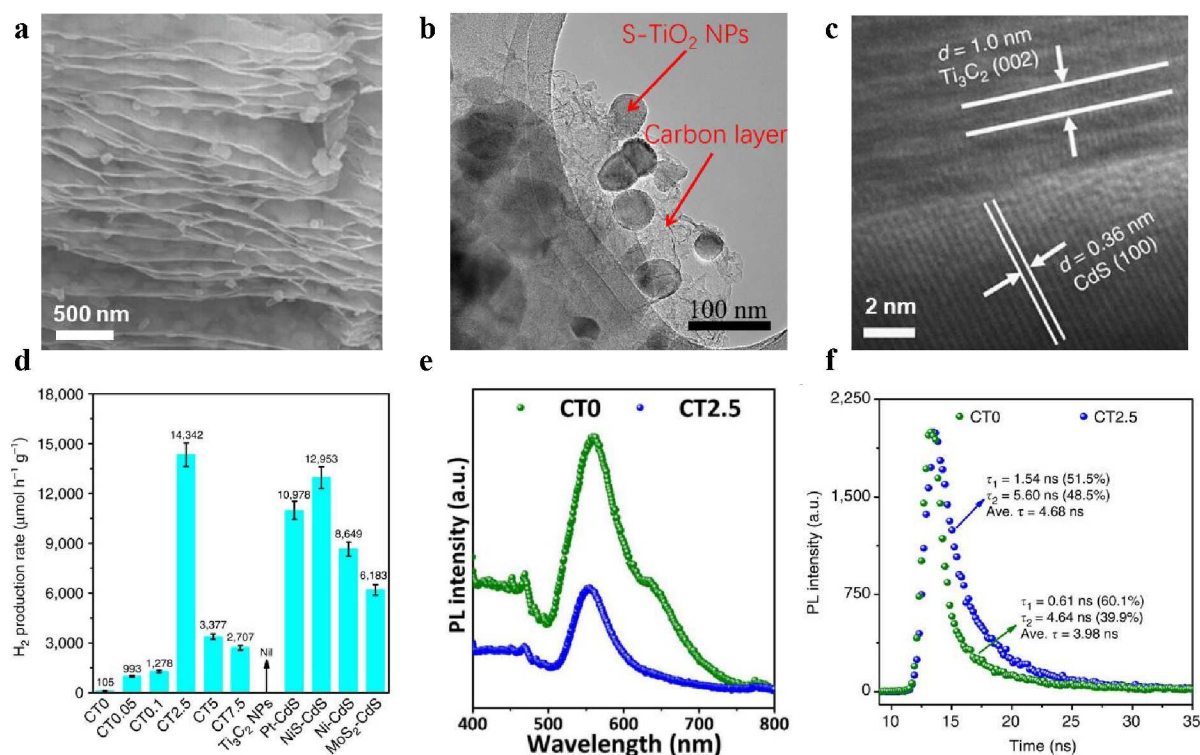
44 As discussed previously, MXenes generally exhibit only modest OER activity and hence rely  
45 on hybridization with OER-active catalysts (such as TM chalcogenides<sup>102</sup> and LDHs<sup>126,149</sup>), with  
46 the MXenes serving primarily as conductive supports and electronic modulators.<sup>44,139</sup> Thus, most  
47 PC/PEC applications of MXenes and their hybrids are directed at HER instead of OER to take  
48 advantage of MXenes' HER activity. In this endeavor, MXenes, especially Ti-based MXenes, have  
49  
50  
51  
52  
53  
54  
55  
56  
57  
58  
59  
60

1  
2  
3 been employed as precursors to TM oxides with rich vacancies, which are widely considered as  
4 stable, efficient, and robust HER photocatalysts.<sup>83,97,100</sup>  
5  
6

7  
8 Yuan *et al.* oxidized  $\text{Ti}_3\text{C}_2\text{T}_x$  in  $\text{CO}_2$  at high temperatures to produce a 2D MXene-derived  
9 C/ $\text{TiO}_2$  hybrid.<sup>83</sup> Since the Ti and C atoms were already alternately arranged in the MXene  
10 structure ( $\text{Ti}_3\text{C}_2\text{T}_x$ ), calcination is likely to result in alternating  $\text{TiO}_2$  and 2D carbon sheets, while  
11 retaining the large-area 2D-layered structure of MXenes, which is suitable for PC HER (**Figure**  
12 **7a**). After optimizing for calcination temperature and  $\text{CO}_2$  flow rates, C/ $\text{TiO}_2$ -700-150 hybrid  
13 exhibited the highest PC  $\text{H}_2$  generation rate of  $24 \mu\text{mol g}^{-1} \text{h}^{-1}$ , representing an 89-fold  
14 enhancement from  $\text{TiO}_2$ . This was credited to the thin carbon layers facilitating charge transport,  
15 whose high electrical conductivity improved photo-carrier separation efficiency and reduced their  
16 recombination rate, in agreement with other works.<sup>100,190,191</sup> The thin carbon layers also provided  
17 a high degree of transparency for visible light penetration to the  $\text{TiO}_2$  photo-absorber. This method  
18 was also employed to synthesize S-doped  $\text{TiO}_2$  NPs/C (**Figure 7b**) from S-doped  $\text{Ti}_3\text{C}_2\text{T}_x$ ,  
19 whereby S doping further optimized  $\text{H}^+$  binding energy for efficient HER.<sup>97</sup> The strategy of using  
20 MXenes as precursors to synthesize MXene/TM oxide hybrids has also been applied to other  
21 MXenes, given the relative ease in oxidizing MXenes,<sup>192,193</sup> such as in the oxidation of  $\text{Nb}_2\text{CT}_x$  to  
22  $\text{Nb}_2\text{CT}_x/\text{C}/\text{Nb}_2\text{O}_5$ ,<sup>194</sup>  $\text{Mo}_2\text{CT}_x$  to  $\text{Mo}_2\text{C}/\text{MoO}_x$ ,<sup>148</sup> and  $\text{V}_2\text{CT}_x$  to  $\text{V}_2\text{CT}_x/\text{V}_2\text{O}_x$ .<sup>57,195</sup>  
23  
24  
25  
26  
27  
28  
29  
30  
31  
32  
33  
34  
35  
36  
37  
38  
39  
40  
41  
42  
43

44 Apart from acting as TM oxide precursors, MXenes can also serve as efficient PC/PEC HER  
45 co-catalysts themselves to promote photo-generated charge carrier separation when coupled to  
46 semiconductors.<sup>133,196–199</sup> The most widely studied MXene,  $\text{Ti}_3\text{C}_2\text{T}_x$ , has been applied as a PC HER  
47 co-catalyst and successfully coupled to a variety of semiconducting photocatalysts such as TM  
48 oxides,<sup>191,196</sup> sulfides,<sup>124,187</sup> perovskites,<sup>197,198</sup> and  $g\text{-C}_3\text{N}_4$ .<sup>133,199</sup>  
49  
50  
51  
52  
53  
54  
55  
56  
57  
58  
59  
60

1  
2  
3 For instance, Ran *et al.* investigated the use of  $\text{Ti}_3\text{C}_2\text{T}_x$  as a HER co-catalyst, with CdS acting  
4 as a photo-absorber for PC HER.<sup>187</sup> The electrostatic self-assembly of CdS NPs on  $\text{Ti}_3\text{C}_2\text{T}_x$  NPs  
5 produced cauliflower-structured sub-microspheres (referred to as CTX, where X refers to the mass  
6 ratio of MXenes : CdS) with distinct and well-formed  $\text{Ti}_3\text{C}_2\text{T}_x/\text{CdS}$  interfaces (**Figure 7c**). An  
7 optimal 2.5 wt% MXene incorporation (CT2.5) resulted in a substantial 136-fold improvement in  
8  $\text{H}_2$  production rate compared to bare CdS (CT0, **Figure 7d**). In fact, the strongly coupled  
9  $\text{Ti}_3\text{C}_2\text{T}_x/\text{CdS}$  (CT2.5) hybrid outperformed other hybrids such as 2.5 wt% Pt-CdS, NiS-CdS, Ni-  
10 CdS and  $\text{MoS}_2\text{-CdS}$  (**Figure 7d**). The outstanding PC HER activity of CT2.5 was attributed to a  
11 reduction in interfacial charge transfer resistance arising from intimate chemical coupling at the  
12  $\text{Ti}_3\text{C}_2\text{T}_x/\text{CdS}$  interface, and high metallic conductivity of  $\text{Ti}_3\text{C}_2\text{T}_x$ . Furthermore, the photo-carrier  
13 separation efficiency was enhanced by deliberately matching the energy bands of  $\text{Ti}_3\text{C}_2\text{T}_x$  and CdS  
14 in a Schottky junction to trap photo-generated electrons and limit carrier recombination. This was  
15 observed in the suppression of both the radiative recombination photoluminescence (PL,  $\lambda \approx 560$   
16 nm, **Figure 7e**), and defect level recombination (red-shifted tail from 650–700 nm in **Figure 7e**)  
17 peaks, resulting in a longer overall photo-carrier lifetime (**Figure 7f**). Finally, theoretical  
18 calculations revealed that –O terminations in  $\text{Ti}_3\text{C}_2\text{T}_x$  served as active HER sites due to their  
19 favorable  $E_F$  position and efficient  $\text{H}^+$  adsorption.  $\text{Ti}_3\text{C}_2\text{T}_x$  was also further hybridized with other  
20 semiconductor photocatalysts such as ZnS and  $\text{Zn}_{0.8}\text{Cd}_{0.2}\text{S}$  and similar trends in improved PC HER  
21 activity was observed. This work thus demonstrates the use of O-terminated  $\text{Ti}_3\text{C}_2\text{T}_x$  as efficient  
22 and durable PC HER co-catalysts for synergistic coupling with a variety of earth-abundant  
23 semiconductor photocatalysts (*e.g.* CdS, ZnS,  $\text{Zn}_{1-x}\text{Cd}_x\text{S}$ ) to achieve significantly improved PC  
24 HER performances for PC water splitting.  
25  
26  
27  
28  
29  
30  
31  
32  
33  
34  
35  
36  
37  
38  
39  
40  
41  
42  
43  
44  
45  
46  
47  
48  
49  
50  
51  
52  
53  
54  
55  
56  
57  
58  
59  
60



**Figure 7.** MXene hybrids for PC HER. (a) SEM of  $\text{Ti}_3\text{C}_2\text{T}_x$ -derived 2D-layered C/ $\text{TiO}_2$ . Adapted with permission from ref<sup>83</sup>. Copyright 2017 WILEY-VCH. (b) High resolution TEM (HRTEM) of  $\text{Ti}_3\text{C}_2\text{T}_x$ -derived S- $\text{TiO}_2$ /C. Adapted with permission under a Creative Commons CC-BY license from ref<sup>97</sup>. Copyright 2018 The Authors. (c) HRTEM of 2.5%- $\text{Ti}_3\text{C}_2\text{T}_x$ :CdS hybrid (CT2.5). (d) PC HER activity of various co-catalysts hybridized with CdS. (e) PL and (f) time-resolved PL spectrum of bare CdS (CT0), and CT2.5 MXene hybrids. Adapted with permission under a Creative Commons CC-BY license from ref<sup>187</sup>. Copyright 2017 The Author(s).

**Summary, specific challenges, and outlook for EC, PC, and PEC water splitting.** In this section, we reviewed the various materials hybridized with MXenes for EC/PC/PEC HER, OER, and water splitting. A summary table of performance metrics ( $\eta_{j=10}$ , Tafel slope, and turnover rate) for various MXene hybrids in EC HER/OER and PC/PEC HER is provided in **Tables S2 and S3** respectively. In summary, MXenes play various critical roles: (1) providing a large-area conductive and structural support, (2) acting as a HER co-catalyst, (3) confining, stabilizing, and thus preventing the hybridized material from aggregating on the MXene support, and (4) inducing charge transfer to modulate the electronic band structure of the hybrid material to optimize  $\text{H}^+$ ,  $\text{OH}^-$ , and water adsorption kinetics when strongly and chemically coupled to other materials.

1  
2  
3 Lattice strain induced at the MXene-secondary material interfaces can also alter electronic density  
4 and stabilize metastable co-catalyst material phases through strain and phase engineering. Apart  
5 from activity enhancement, MXene hybrids also benefit from improved stability in acidic and  
6 alkaline electrolytes (**Figure 5f**).<sup>126</sup> A strong and chemically coupled MXene hybrid, especially at  
7 the hybrid interface, is important for prolonged cycling and operational stability, particularly at  
8 higher current densities.<sup>149</sup> The NiFe-LDH/Ti<sub>3</sub>C<sub>2</sub>T<sub>x</sub>/3D nickel foam hybrid was stable for 200 h of  
9 continuous water splitting in 1 M KOH at a high current density of 100 mA cm<sup>-2</sup> due to the strong  
10 chemical integration between the LDH, MXenes, and 3D nickel foam network.<sup>149</sup> Conversely,  
11 Mo<sub>2</sub>CT<sub>x</sub>/2H-MoS<sub>2</sub> hybrid suffered a significant ≈50% loss in operating current density after a short  
12 8 h of HER.<sup>200</sup> This was due to crack formation within the hybrid, and MoS<sub>2</sub> dislodgement during  
13 HER, possibly due to poor chemical integration between Mo<sub>2</sub>CT<sub>x</sub> and 2H-MoS<sub>2</sub>.

14  
15  
16  
17  
18  
19  
20  
21  
22  
23  
24  
25  
26  
27  
28  
29 Presently, non-PGM MXene hybrid couples have outperformed full-PGM couples (IrO<sub>2</sub> and  
30 RuO<sub>2</sub> for OER, Pt/C for HER) for EC water splitting due to the exceptional OER activity from the  
31 non-MXene OER-active components (TM phosphides, LDHs). From an activity standpoint, more  
32 work should thus be done on improving non-PGM MXene hybrids for HER, and this begins by  
33 working with Mo-based MXenes, which possess a higher intrinsic HER activity compared to Ti-  
34 based MXenes.<sup>17</sup> Concurrently, further improvement in the OER competitiveness of MXene  
35 hybrids can be realized through the theory-guided development of MXenes with higher intrinsic  
36 OER activities such as nitride MXenes.<sup>201</sup> Lastly, the use of *operando* and localized  
37 electrochemical/physical characterization techniques such as scanning electrochemical cell  
38 microscopy (SECCM) can elucidate more information on catalytic activity at different areas of the  
39 MXene hybrid, of which regions near and at the hybrid interface is of particular interest for further  
40  
41  
42  
43  
44  
45  
46  
47  
48  
49  
50  
51  
52  
53  
54  
55  
56  
57  
58  
59  
60



1  
2  
3 investigation.<sup>19,202</sup> These investigations are of particular importance to MXene hybrids for OER,  
4  
5 since MXenes can be readily oxidized to TM oxides under the applied oxidizing potentials.  
6  
7  
8  
9  
10  
11  
12  
13  
14  
15  
16  
17  
18  
19  
20  
21  
22  
23  
24  
25  
26  
27  
28  
29  
30  
31  
32  
33  
34  
35  
36  
37  
38  
39  
40  
41  
42  
43  
44  
45  
46  
47  
48  
49  
50  
51  
52  
53  
54  
55  
56  
57  
58  
59  
60

## MXENE HYBRIDS AS ELECTROCATALYSTS FOR METAL-AIR AND METAL-SULFUR BATTERIES

Aside from their high HER and OER catalytic activity for water splitting, MXene hybrids are also similarly efficient in catalyzing the OER/ORR redox couple<sup>203,204</sup> to serve as cathodes for metal-air batteries.<sup>180,205–207</sup> With high metallic conductivity, MXene hybrids are well-positioned to facilitate rapid electronic transfer for sulfur redox reactions at the sulfur cathode in lithium-sulfur (Li-S) batteries as well.<sup>56,208</sup> MXene hybrids have recently been demonstrated to possess a high binding affinity toward deleterious lithium polysulfide (LiPS) side products when used as a separator, extending the cycle life and reducing the capacity fade of Li-S batteries.<sup>209,210</sup> In this section, we review the catalytic role of MXene hybrids towards realizing the industrial potential of metal-air and metal-sulfur batteries (see **Vocabulary** for full definition) as next-generation battery architectures to complement existing lithium ion batteries (LIBs).

**MXene hybrids and composites for electrocatalytic (EC) OER and ORR in metal-air batteries.** A post-LIB technological prospect, metal-air batteries comprise of design elements from both traditional batteries (using a metal anode) and fuel cells (using a cathode exposed to air).<sup>8</sup> Metal-air batteries have attracted widespread interest due to their compact size, lightweight composition,<sup>211</sup> and high theoretical energy density.<sup>212</sup> For instance, Zn-air batteries have a theoretical energy density (1350 Wh kg<sup>-1</sup>, excluding oxygen) about five times that of LIBs,<sup>212</sup> and can be produced at significantly lower costs (<\$10 kW<sup>-1</sup> h<sup>-1</sup>) than LIBs (≈\$400–800 kW<sup>-1</sup> h<sup>-1</sup>).<sup>213</sup>

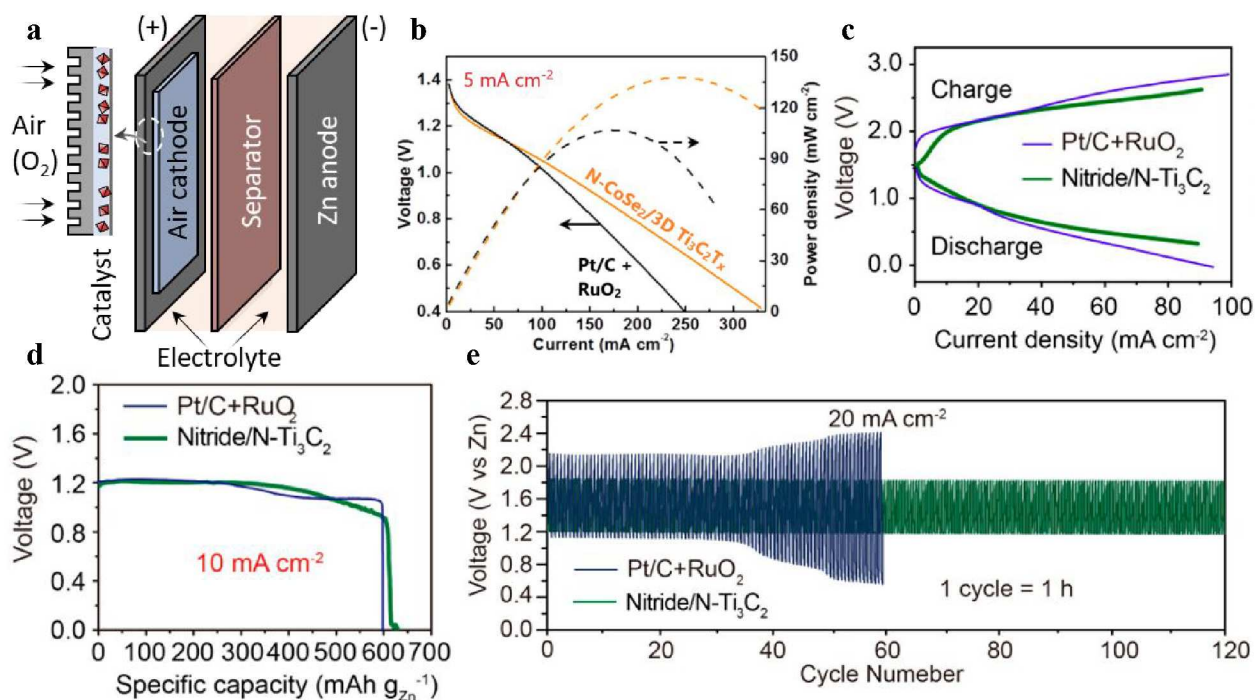
Unfortunately, the theoretical promise of metal-air batteries has yet to be practically realized due to their poor air cathode performance. The complex, multi-step, four-electron OER/ORR redox couple is severely hampered by sluggish kinetics as the rate-determining step.<sup>211</sup>

1  
2  
3 Even though MXenes are not OER or ORR-active as previously discussed, MXenes have been  
4 utilized as conductive supports for other ORR-active electrocatalysts.<sup>182,206</sup> Hybridizing MXenes  
5 with other materials also resulted in electronic structure modulation, and the creation of catalytic  
6 motifs to exhibit enhanced OER, ORR, and bifunctional OER/ORR activity comparable to PGMs  
7 such as Pt/C (for ORR) and IrO<sub>2</sub>/RuO<sub>2</sub> (for OER).<sup>123,139,180</sup> Since MXene hybrids for EC OER have  
8 been described previously for water splitting, we focus our discussions here on MXene hybrids for  
9 EC ORR, bifunctional EC OER/ORR, and their use in Zn-air batteries.<sup>180,205–207</sup> A summary of EC  
10 ORR performances for various MXene hybrids is provided in **Table S2c**.

11  
12  
13  
14  
15  
16  
17  
18  
19  
20  
21  
22 Iron-nitrogen-carbon (Fe-N-C) materials are one of the most promising class of PGM-free  
23 ORR catalysts due to their highly active FeN<sub>4</sub> motifs.<sup>123,203,214</sup> To further augment the intrinsic  
24 ORR activity of iron phthalocyanine (FePc), Li *et al.* hybridized FePc on Ti<sub>3</sub>C<sub>2</sub>T<sub>x</sub> support and  
25 obtained a significant two-fold activity enhancement in FePc, which was also five times higher  
26 than Pt/C.<sup>123</sup> Two-electron ORR was also virtually suppressed with a calculated electron number  
27 of ≈4 and an ultralow H<sub>2</sub>O<sub>2</sub> yield (<1%). The authors posit that the negatively charged –OH/–F T<sub>x</sub>  
28 groups of Ti<sub>3</sub>C<sub>2</sub>T<sub>x</sub> interacted strongly with the Fe<sup>2+</sup> center through intermolecular van der Waals  
29 forces or hydrogen bonding to reduce the local Fe<sup>2+</sup> electron density, which induced a transition  
30 to a higher spin state to optimize O<sub>2</sub> binding for ORR. A follow-up work synthesized  
31 Fe(phen)<sub>2</sub>/Ti<sub>3</sub>C<sub>2</sub>T<sub>x</sub> hybrids through pyrolysis, using the MXene as a large-area 2D conductive  
32 support to prevent aggregation of the rugged Fe(phen)<sub>2</sub> coating.<sup>214</sup> Separately, positively charged  
33 2D Fe-N-C sheets were produced by decorating g-C<sub>3</sub>N<sub>4</sub> sheets with Fe NPs.<sup>203</sup> By manipulating  
34 the Fe/g-C<sub>3</sub>N<sub>4</sub> precursor ratio, the positive zeta potential (from Fe<sup>2+</sup>) per unit area of Fe-N-C sheets  
35 was adjusted to +30.4 mV to match the negative zeta potential (from MXenes' T<sub>x</sub> groups) per unit  
36 area of Ti<sub>3</sub>C<sub>2</sub>T<sub>x</sub> sheets (-39.7 mV). This allowed both sheets to be electrostatically self-assembled  
37  
38  
39  
40  
41  
42  
43  
44  
45  
46  
47  
48  
49  
50  
51  
52  
53  
54  
55  
56  
57  
58  
59  
60

1  
2  
3 in a 2D/2D layered superlattice-like heterostructure in aqueous solutions with enhanced ORR  
4 activity. This work can potentially be further extended to manipulate the positive sheet charges of  
5 other 2D materials using TM NP clusters to achieve the wet chemical, electrostatic self-assembly  
6 of 2D material/MXene layered heterostructures, circumventing the use of small-scale and energy  
7 intensive physical deposition methods such as CVD and ALD.  
8  
9

10  
11  
12  
13  
14  
15 TM oxide<sup>207</sup> and chalcogenide<sup>206</sup> NPs have also been incorporated onto MXene scaffolds  
16 to synergistically enhance ORR activity for Zn-air batteries (**Figure 8a**). For example, 3D N-  
17 CoSe<sub>2</sub>/MXene architecture can be obtained with the aid of a poly(vinylalcohol) (PVA) cross-  
18 linker, followed by thermal annealing in NH<sub>3</sub>.<sup>206</sup> The 3D architecture separates the MXene layers  
19 and prevents them from aggregation, thus maximizing ECSA and mass transport properties.  
20 Theoretical calculations revealed that N-CoSe<sub>2</sub>/MXene hybridization increases the activity at Co  
21 sites, by virtue of significant electron transfer from Ti<sub>3</sub>C<sub>2</sub>T<sub>x</sub> to CoSe<sub>2</sub>, while N-doping reduces the  
22 thermodynamic barrier to the potential-limiting steps for both OER and ORR. This resulted in a  
23 highly efficient bifunctional OER/ORR electrocatalyst, with a higher specific capacity (751 mAh  
24 g<sub>Zn</sub><sup>-1</sup>) than the RuO<sub>2</sub>+Pt/C OER/ORR benchmark (690 mAh g<sub>Zn</sub><sup>-1</sup>) when discharged at 5 mA cm<sup>-2</sup>.  
25 The discharge characteristics and maximum power density of N-CoSe<sub>2</sub>/3D Ti<sub>3</sub>C<sub>2</sub>T<sub>x</sub> (142 mW cm<sup>-2</sup>  
26 at 232 mA cm<sup>-2</sup>) also outperforms the full PGM standard reference of RuO<sub>2</sub> + Pt/C (119 mW cm<sup>-2</sup>  
27 at 168 mA cm<sup>-2</sup>), as seen in **Figure 8b**. The high cycling stability (500 cycles, 166 h at 10 mA  
28 cm<sup>-2</sup>) was attributed to the preservation of the 3D MXene architecture and strong integration of  
29 CoSe<sub>2</sub> NPs into the MXene network, which prevented CoSe<sub>2</sub> NPs from dislodging during cycling.  
30  
31  
32  
33  
34  
35  
36  
37  
38  
39  
40  
41  
42  
43  
44  
45  
46  
47  
48  
49  
50  
51  
52  
53  
54  
55  
56  
57  
58  
59  
60



**Figure 8.** MXene hybrids as air cathodes for (a) Zn-air batteries. (b) Discharge and power density curves of N-CoSe<sub>2</sub>/3D Ti<sub>3</sub>C<sub>2</sub>T<sub>x</sub> cathode, compared against Pt/C + RuO<sub>2</sub>. Adapted with permission from ref <sup>206</sup>. Copyright 2019 American Chemical Society. (c) Charge-discharge polarization curves, (d) specific capacities (calculated with Zn mass consumed) and (e) galvanostatic charge-discharge cycling of NiFeMn nitride/N-Ti<sub>3</sub>C<sub>2</sub>T<sub>x</sub> cathode, compared against Pt/C + RuO<sub>2</sub>. Adapted with permission from ref <sup>180</sup>. Copyright 2020 American Chemical Society.

Recently, fiber-shaped flexible Zn-air batteries were developed with molecularly thin trimetallic NiFeMn nitride sheets stabilized by Ti<sub>3</sub>C<sub>2</sub>T<sub>x</sub>, exhibiting bifunctionality toward both OER and ORR.<sup>180</sup> The stabilization effect was supported by theoretical calculations, while strong interfacial coupling between the nitride and Ti<sub>3</sub>C<sub>2</sub>T<sub>x</sub> sheets was marked by the formation of ORR-active motifs (Ni/Fe/Mn-N-Ti) from the Ti (MXene)-N (trimetallic nitride) peak in the Ti 2p XPS spectrum. The ECSA for ORR/OER was maximized by stabilizing the 2D nitride sheets atop the MXene sheets, which facilitated efficient charge transport for electrocatalysis. This resulted in synergistic OER and ORR activity enhancement of the nitride/N-Ti<sub>3</sub>C<sub>2</sub>T<sub>x</sub> hybrid after Ti<sub>3</sub>C<sub>2</sub>T<sub>x</sub> incorporation, despite standalone Ti<sub>3</sub>C<sub>2</sub>T<sub>x</sub> being practically OER and ORR-inactive. The potential difference between the OER  $\eta_{j=10}$  and ORR half-wave potential ( $E_{1/2}$ ) was smaller for the nitride/N-

1  
2  
3  $\text{Ti}_3\text{C}_2\text{T}_x$  hybrid (0.68 V) than  $\text{RuO}_2 + \text{Pt}/\text{C}$  (0.80 V), illustrating the hybrid's superior OER/ORR  
4  
5 bifunctionality without the use of PGMs. When used in Zn-air battery applications, the bifunctional  
6  
7 nitride/N- $\text{Ti}_3\text{C}_2\text{T}_x$  air cathode operated with a smaller charge-discharge voltage gap (hence better  
8  
9 rechargeability, **Figure 8c**), and higher specific capacity (**Figure 8d**,  $630 \text{ mAh g}_{\text{Zn}}^{-1}$ ) than  $\text{RuO}_2 +$   
10  
11  $\text{Pt}/\text{C}$ . The hybrid also demonstrated long-term cycling stability for 120 cycles (120 h at  $20 \text{ mA cm}^{-2}$ )  
12  
13 with no appreciable voltage fade, in comparison to the large voltage increase and hence  
14  
15 instability of the  $\text{RuO}_2 + \text{Pt}/\text{C}$  air cathode during the same cycling test (**Figure 8e**). After being  
16  
17 incorporated into a unique fibrous design, the flexible Zn-air battery operated durably for more  
18  
19 than 3 h under various mechanical deformation states for wearable technology applications.  
20  
21  
22  
23

24  
25 **Summary, specific challenges, and outlook for metal-air batteries.** MXene hybrid  
26  
27 metal-air batteries are still in their early stages of development, with predominantly  $\text{Ti}_3\text{C}_2\text{T}_x$ -based  
28  
29 MXene hybrids being explored for Zn-air batteries. Theoretically, a high efficiency for MXene-  
30  
31 derived catalyst supports has been predicted for Li-air batteries due to the MXenes' ability to  
32  
33 adsorb Li species to facilitate interfacial charge transfer and redox reactions.<sup>215</sup> We thus expect  
34  
35 MXene hybrids to be explored for other metal-air chemistries such as Li, Na, Mg and Al, using  
36  
37 other highly conductive MXenes apart from  $\text{Ti}_3\text{C}_2\text{T}_x$ .  
38  
39  
40

41  
42 Beyond metal-air batteries, the high ORR activity of MXene hybrids can also be translated  
43  
44 to effective PC pollutant degradation and environmental remediation, an essential application that  
45  
46 can be readily deployed in remote and less developed areas. For example,  $\text{Ti}_3\text{C}_2\text{T}_x/\text{TiO}_2$ ,<sup>47</sup>  
47  
48  $\text{Ti}_3\text{C}_2\text{T}_x/\text{Ag}_3\text{PO}_4$ ,<sup>122</sup> and  $\text{In}_2\text{S}_3/\text{TiO}_2@ \text{Ti}_3\text{C}_2\text{T}_x$ <sup>48</sup> hybrids have demonstrated very high activity and  
49  
50 durability for PC removal of organic dyes and inorganic pollutants.<sup>42,44</sup> By combining strategies  
51  
52 for designing efficient water splitting photocatalysts in the previous section (maximizing photo-  
53  
54 carrier separation and minimizing carrier recombination) with the strategies discussed here in  
55  
56  
57  
58  
59  
60

1  
2  
3 designing efficient ORR electrocatalysts, we anticipate further strides to be made in MXene hybrid  
4 photocatalysts for broad-based pollutant remediation applications too.  
5  
6

7  
8 **MXene hybrids and composites for metal-sulfur batteries.** Li-S batteries have been  
9 touted as the next-generation energy storage device for decades due to their unique conversion  
10 mechanism and high theoretical energy density (2500 Wh kg<sup>-1</sup>).<sup>216</sup> During discharge, the Li anode  
11 is oxidized to Li<sup>+</sup> ions which travel to the S cathode, reacts with it, and forms Li<sub>2</sub>S through a series  
12 of lithiation steps and intermediate LiPS species ( $n \text{Li}^+ + \text{S}_8 + n e^- \rightarrow \text{soluble Li}_2\text{S}_8 \rightarrow \text{Li}_2\text{S}_6 \rightarrow$   
13  $\text{Li}_2\text{S}_4 \rightarrow \dots \rightarrow \text{solid Li}_2\text{S}$ ). In reality, the majority of the intermediate LiPS species (Li<sub>2</sub>S<sub>4</sub> to Li<sub>2</sub>S<sub>8</sub>)  
14 dissolves readily into the electrolyte before reaching the insoluble Li<sub>2</sub>S phase, resulting in a lower  
15 discharge capacity and rapid capacity decay.<sup>216</sup> The soluble LiPS species can further diffuse to the  
16 Li anode to be chemically reduced to shorter-chain LiPS before diffusing back to the cathode to  
17 be re-oxidized in an internal short circuit/self-discharge (shuttling effect).<sup>216</sup> Furthermore, the poor  
18 ionic and electrical conductivity of the S cathode, coupled with a large volumetric expansion in  
19 the cathode upon lithiation ( $\approx 80\%$ ), imposes structural stress and inhibits electrochemical  
20 performance at the S cathode.<sup>216</sup> To address these issues, S cathodes have been hybridized with C-  
21 based materials to improve conductivity, while polymeric binders, TM oxides and chalcogenides  
22 have been incorporated to improve LiPS adsorption.<sup>216</sup> Separator membranes, commonly coated  
23 with conductive polymers, TM oxides, or C-based materials, have also been placed in the  
24 electrolyte between the electrodes to capture the shuttling LiPS.<sup>216</sup>  
25  
26  
27  
28  
29  
30  
31  
32  
33  
34  
35  
36  
37  
38  
39  
40  
41  
42  
43  
44  
45  
46  
47

48 With a unique combination of metallic conductivity and polar T<sub>x</sub> groups, MXenes have  
49 been employed as S-host materials for both the S cathode<sup>56,208</sup> and separator,<sup>209,210</sup> as they can  
50 chemically interact with LiPS and facilitate efficient electronic transport at the cathode.<sup>14</sup>  
51 Experimentally, highly conductive MXenes (Ti<sub>2</sub>CT<sub>x</sub>,<sup>56,217</sup> Ti<sub>3</sub>C<sub>2</sub>T<sub>x</sub>,<sup>56,218</sup> Ti<sub>3</sub>CNT<sub>x</sub>,<sup>56</sup> and V<sub>2</sub>CT<sub>x</sub><sup>58</sup>)  
52  
53  
54  
55  
56  
57  
58  
59  
60

1  
2  
3 have been investigated as cathode materials. Theoretical studies have also revealed various MXene  
4 structures as good binders for LiPS chemisorption:  $M_2X$  MXenes ( $Ti_2CT_x$ ,<sup>217</sup>  $Ti_2NT_x$ ,<sup>219</sup>  $V_2CT_x$ ,<sup>219</sup>),  
5  
6  $M_3X_2$  MXenes ( $Ti_3C_2T_x$ ,<sup>220</sup>  $V_3C_2T_x$ ,<sup>221</sup>  $Cr_3C_2T_x$ ,<sup>221</sup>  $Zr_3C_2T_x$ ,<sup>221</sup>  $Nb_3C_2T_x$ ,<sup>221</sup>  $Hf_3C_2T_x$ ,<sup>221</sup>), and  
7  
8 ordered double TM MXenes ( $Mo_2TiC_2T_x$ ,<sup>67</sup>). Nazar's group determined that the LiPS species are  
9  
10 strongly bonded to the Ti atoms in  $Ti_2CT_x$  through Lewis acid-base Ti-S bonding at the expense  
11  
12 of Ti-OH ( $T_x$ ) interactions.<sup>56,217</sup> The effect of MXenes' surface chemistry on LiPS affinity was  
13  
14 elucidated by density functional theory (DFT) calculations which concluded that -O and -F  $T_x$   
15  
16 groups act as stronger immobilizers than -F in restricting LiPS diffusion in conventional  
17  
18 electrolytes.<sup>219,221,222</sup> Additionally, N-doping of  $Ti_3C_2T_x$  further improved charge transport  
19  
20 capacity and the Lewis acid-base binding strength to LiPS species.<sup>223</sup> Since the MXene surface  
21  
22 chemistry and doping character can be directly tuned by the synthetic method,<sup>34,43</sup> we expect future  
23  
24 work to utilize theory-guided calculations to screen dopants and  $T_x$  groups, to complement current  
25  
26 synthetic methods and deliberately modulate the LiPS immobilization strength for a variety of  
27  
28 MXenes to act as efficient S-host cathodes and separators for Li-S batteries.  
29  
30  
31  
32  
33  
34  
35

36 Beyond the high electrical conductivity and chemical affinity to LiPS, MXenes are also  
37  
38 mechanically robust to accommodate the large volumetric changes in the S cathode during  
39  
40 charge/discharge cycles.<sup>14</sup> However, MXene nanosheets have a high tendency to self-restack,<sup>51</sup>  
41  
42 limiting the S/LiPS loading and restricting  $Li^+$ /electrolyte access at the S cathode. Thus, secondary  
43  
44 materials have been integrated with MXenes as spacers to reduce MXene inter-layer re-stacking,  
45  
46 while retaining the high electrical conductivity and LiPS binding affinity of MXenes. In this  
47  
48 section, we highlight the use of MXene hybrids as S-host cathode and separator materials,  
49  
50 illustrating how hybridization can augment the LiPS binding affinity to improve discharge capacity  
51  
52 and impede capacity decay beyond that demonstrated by bare MXenes.  
53  
54  
55  
56  
57  
58  
59  
60



1  
2  
3 MXenes have been hybridized with TM chalcogenides<sup>224</sup> and oxides<sup>105,208,225</sup> to chemically  
4 interact with LiPS and expedite their catalytic conversion to Li<sub>2</sub>S (**Figure 9a**). Zhang *et al.*  
5 electrostatically self-assembled a 3D S/MnO<sub>2</sub>@Ti<sub>3</sub>C<sub>2</sub>T<sub>x</sub> hybrid, taking advantage of the high  
6 surface area and conductivity of delaminated Ti<sub>3</sub>C<sub>2</sub>T<sub>x</sub> sheets, and the high chemical affinity of  
7 MnO<sub>2</sub> to LiPS.<sup>208</sup> The 3D mesoporous conductive network enabled a high S loading of ≈70% and  
8 could readily accommodate volumetric changes during charge/discharge cycles. Moreover, the  
9 intense O-Ti-S and O-S peaks in the O 1s XPS spectrum validated the strong MnO<sub>2</sub>-MXene  
10 integration and LiPS retention ability of MnO<sub>2</sub>. The S/MnO<sub>2</sub>@Ti<sub>3</sub>C<sub>2</sub>T<sub>x</sub> cathode had a higher initial  
11 discharge capacity (1140 mAh g<sub>S</sub><sup>-1</sup>, 0.05C) than the unhybridized components, which implies  
12 higher S utilization. The high cathode stability was demonstrated in the hybrid's respectable  
13 specific capacity of 501 mAh g<sub>S</sub><sup>-1</sup> after 500 cycles at 1C, with a minor 0.06% decay/cycle.  
14 Compared to the individual components (S/MnO<sub>2</sub> and S/Ti<sub>3</sub>C<sub>2</sub>T<sub>x</sub>), the S/MnO<sub>2</sub>@Ti<sub>3</sub>C<sub>2</sub>T<sub>x</sub> hybrid's  
15 superior LiPS absorption was visually confirmed by the faintest coloration in the electrolyte after  
16 4 h of cycling, indicating minimal LiPS dissolution into the electrolyte (**Figure 9b**).

17  
18  
19 Separately, the high LiPS binding affinity to other TM compounds such as TiO<sub>2</sub><sup>105,225</sup> and  
20 MoS<sub>2</sub><sup>224</sup> was validated experimentally. When used as symmetric cell electrodes in an electrolyte  
21 with Li<sub>2</sub>S<sub>x</sub> species, Ti<sub>3</sub>C<sub>2</sub>T<sub>x</sub>/1T-2H MoS<sub>2</sub>-C hybrid afforded the highest redox current density, and  
22 hence the fastest rate of catalytic LiPS conversion, as compared to their separate components  
23 (Ti<sub>3</sub>C<sub>2</sub>T<sub>x</sub> and 2H-MoS<sub>2</sub>) and the Ti<sub>3</sub>C<sub>2</sub>T<sub>x</sub>/2H MoS<sub>2</sub>-C hybrid (**Figure 9c**).<sup>224</sup> This highlighted the  
24 importance of higher electrical conductivity (in 1T/2H-MoS<sub>2</sub>) to facilitate electron transfer for  
25 LiPS redox conversion, as compared to using semiconducting 2H-MoS<sub>2</sub> for hybridization with  
26 MXenes. The 1T/2H-MoS<sub>2</sub> also contained a high concentration of edge defects and positively  
27  
28  
29  
30  
31  
32  
33  
34  
35  
36  
37  
38  
39  
40  
41  
42  
43  
44  
45  
46  
47  
48  
49  
50  
51  
52  
53  
54  
55  
56  
57  
58  
59  
60

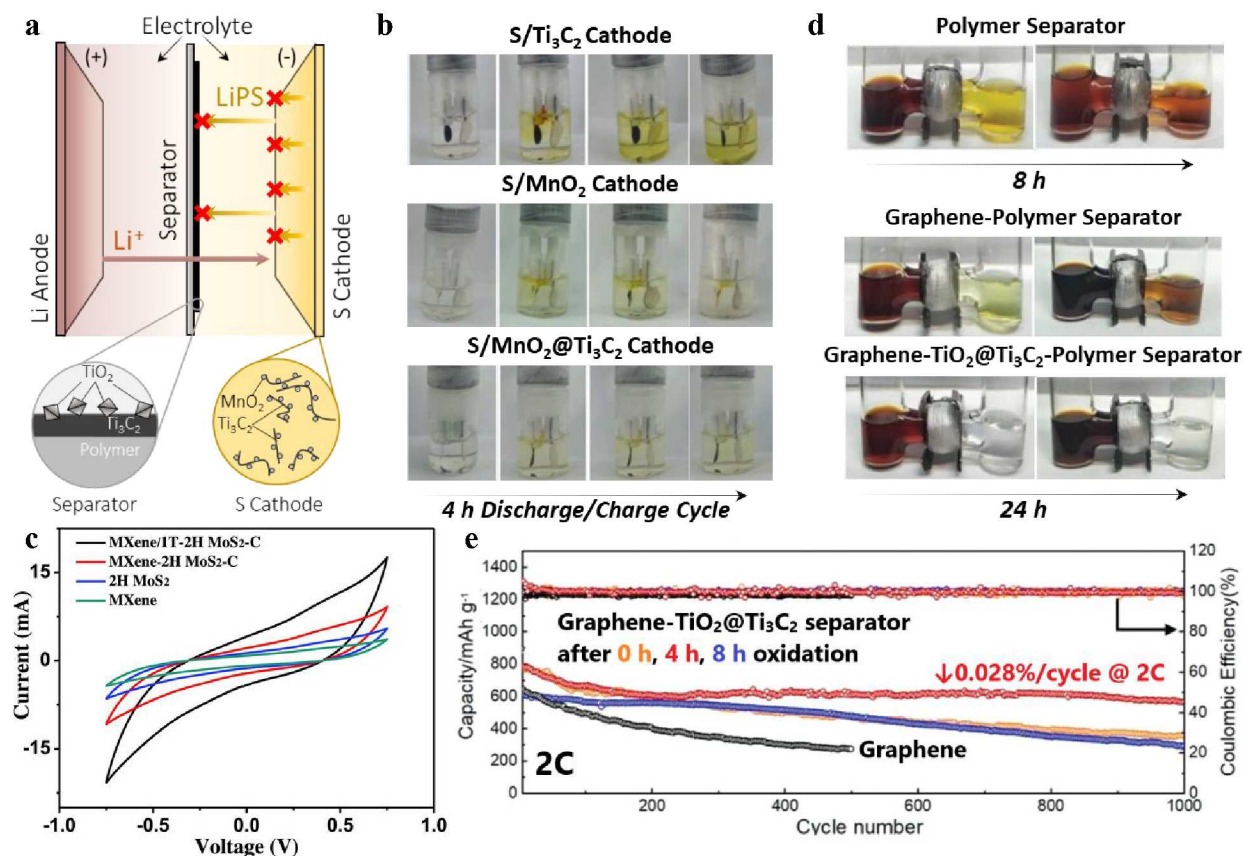
1  
2  
3 charged S vacancies to bind strongly to negatively charged LiPS and facilitate electron transfer for  
4 rapid LiPS redox conversion.  
5  
6

7  
8 Beyond TM compounds, C-based materials<sup>56,64,218</sup> have also been hybridized with MXenes  
9 to further improve the cathode's electronic conductivity<sup>56</sup> for more efficient S utilization, and  
10 provide large surface areas to physically confine LiPS species.<sup>218</sup> Interweaving Ti-based MXene  
11 nanosheets ( $\text{Ti}_3\text{C}_2\text{T}_x$ ,  $\text{Ti}_2\text{CT}_x$ , and  $\text{Ti}_3(\text{CN})\text{T}_x$ ) with CNTs inhibited MXene inter-layer restacking  
12 to maximize Ti-S interactions for LiPS absorption, which led to stable cycling performances with  
13 high S loading of up to  $5.5 \text{ mg cm}^{-2}$  for high energy density Li-S batteries.<sup>56</sup> Separately, Zhou *et*  
14 *al.* treated  $\text{Ti}_3\text{C}_2\text{T}_x$  sheets with molten KOH to produce  $\text{Ti}_3\text{C}_2\text{T}_x/\text{C}$  hybrids with an expanded inter-  
15 layer spacing and significantly increased surface area (from  $3.5$  to  $150 \text{ m}^2 \text{ g}^{-1}$ ).<sup>218</sup> Hybridization  
16 with disordered C also reduced the charge transfer resistance by five-folds to accelerate LiPS  
17 conversion, increasing the calculated  $\text{Li}_2\text{S}$  precipitation capacity from  $95$  to  $226 \text{ mAh g}^{-1}$ .<sup>218</sup> Since  
18  $\text{TiO}_2$  was previously reported to improve LiPS binding efficiency,<sup>105,225</sup> we predict that the partial  
19 oxidation of Ti-based MXenes to MXene/ $\text{TiO}_2/\text{C}$  hybrids<sup>92</sup> (similar to those for PC HER  
20 applications) may significantly enhance LiPS absorption and redox conversion kinetics, while  
21 providing a conductive, large-area support for LiPS deposition.  
22  
23  
24  
25  
26  
27  
28  
29  
30  
31  
32  
33  
34  
35  
36  
37  
38  
39  
40

41 MXenes and their hybrids have also been incorporated in Li-S battery separators. As some  
42 MXenes are known to have high LiPS binding affinity, MXene-containing separators can  
43 immobilize parasitic LiPS shuttling between electrodes, thus limiting the internal short circuit  
44 effect and prolonging cycling stability.<sup>209,210,226</sup> Similar to the cathode designs, MXenes have been  
45 hybridized with TM oxides (with high LiPS adsorption affinity)<sup>227</sup> and C-based materials<sup>210,226</sup> to  
46 act as efficient physical barriers at the separator facing the cathode. For example, Jiao *et al.*  
47 produced  $\text{TiO}_2@\text{Ti}_3\text{C}_2\text{T}_x$  hybrids from controlled partial oxidation of  $\text{Ti}_3\text{C}_2\text{T}_x$ , to be mixed with  
48  
49  
50  
51  
52  
53  
54  
55  
56  
57  
58  
59  
60

1  
2  
3 graphene and coated on a commercial Celgard polymer separator (**Figure 9a**).<sup>227</sup> From the LiPS  
4 permeation test (**Figure 9d**), no significant darkening in the electrolyte was observed when the  
5 optimized (4 h oxidation) graphene-TiO<sub>2</sub>@Ti<sub>3</sub>C<sub>2</sub>T<sub>x</sub>-polymer separator was used, in contrast to the  
6 untreated and graphene-coated separators. This validated the use of TiO<sub>2</sub> as LiPS adsorption  
7 centers, while MXenes provided a conductive large-area support to facilitate rapid LiPS  
8 conversion. When the separator was incorporated into a Li-S cell, only a minor 0.028% capacity  
9 fade/cycle was observed over 1000 cycles at 2C (red curve, **Figure 9e**), with stable cycling also  
10 observed for over 200 cycles at a higher 7.3 mg cm<sup>-2</sup> S loading.  
11  
12  
13  
14  
15  
16  
17  
18  
19  
20  
21

22 **Summary, specific challenges, and outlook of metal-sulfur batteries.** The discovery of  
23 a strong Ti (MXene)-S (LiPS) bond,<sup>56</sup> coupled with high metallic conductivity and mechanical  
24 flexibility, have enabled Ti-based MXenes to serve as large-area S-host materials in Li-S cathodes  
25 and separators. By hybridizing MXenes with other secondary materials with high affinity toward  
26 LiPS absorption, MXene hybrids have successfully enhanced LiPS capture and redox conversion  
27 kinetics to improve the discharge capacity and cycling stability. While not discussed in this section,  
28 MXenes have also been utilized as S-host materials for Na-S batteries,<sup>228</sup> and have shown promise  
29 as alkali metal hosts to impede dendrite formation at the anode.<sup>229–232</sup> We thus expect efforts to be  
30 made in the theoretical screening of potential MXene hybrid combinations, especially with  
31 conductive non-Ti-based MXenes, for LiPS binding affinity and catalytic conversion to Li<sub>2</sub>S.  
32 Combined with advanced synthetic designs in phase, defect, doping, and structural engineering of  
33 secondary materials on MXenes, future MXene hybrids could be applied in the cathode, anode,  
34 and separator to realize industrially relevant Li-S batteries with high discharge capacities, cycling  
35 stability, and S loading.  
36  
37  
38  
39  
40  
41  
42  
43  
44  
45  
46  
47  
48  
49  
50  
51  
52  
53  
54  
55  
56  
57  
58  
59  
60



**Figure 9.** MXene hybrids as S cathodes and separators for (a) Li-S batteries. (b) Photographs of S/Mn<sub>3</sub>O<sub>4</sub>@Ti<sub>3</sub>C<sub>2</sub>T<sub>x</sub> S cathode during 4 h of charge-discharge (yellow colouration indicates LiPS leeching into the electrolyte). Adapted from ref <sup>208</sup>. Copyright 2018 American Chemical Society. (c) Symmetric cell cyclic voltammetry (CV) cycling using the MXene hybrids for both electrodes. Adapted from ref <sup>224</sup>. Copyright 2018 WILEY-VCH. (d) Visual LiPS permeation test with graphene-TiO<sub>2</sub>@Ti<sub>3</sub>C<sub>2</sub>T<sub>x</sub>-polymer separator (yellow/brown colouration on the right side of the cell indicates LiPS permeating through the separator) and (e) long-term cycling of graphene-TiO<sub>2</sub>@Ti<sub>3</sub>C<sub>2</sub>T<sub>x</sub> separators (with different oxidation durations) at 2C. Adapted from ref <sup>227</sup>. Copyright 2019 WILEY-VCH.

1  
2  
3 MXENE HYBRIDS FOR EMERGING EC, PC, AND PEC REACTIONS OF INTEREST  
4  
5

6 TM carbides and nitrides have a long history in catalyzing hydrogenation (or  
7 dehydrogenation) reactions due to their suitable surface interactions with the relevant reaction  
8 intermediates.<sup>233,234</sup> With growing research interest in sustainable catalytic reactions, it was  
9 discovered that TM carbides and nitrides are also active in the catalytic conversion of abundant  
10 and stable moieties like CO<sub>2</sub> or N<sub>2</sub> to higher value-added chemicals.<sup>235</sup> Sharing similarities to the  
11 bulk 3D crystalline TM carbide and nitride forms, MXenes are also anticipated to be catalytically  
12 active for CO<sub>2</sub> and N<sub>2</sub> activation due to their suitable adsorption sites<sup>236,237</sup> and favorable adsorbate  
13 interactions.<sup>238</sup> Having recently demonstrated promising nitrogen and carbon catalysis on  
14 MXenes,<sup>25,239</sup> MXene hybrids have been predicted to expand the platform even further to enhance  
15 catalytic activity and catalyze other important reactions in the future. Here, we analyze the current  
16 strategies and pathways in which MXenes hybrids have been used to enhance important PC, EC,  
17 and PEC reactions of CO<sub>2</sub>, N<sub>2</sub>, and their related moieties.  
18  
19  
20  
21  
22  
23  
24  
25  
26  
27  
28  
29  
30  
31  
32  
33

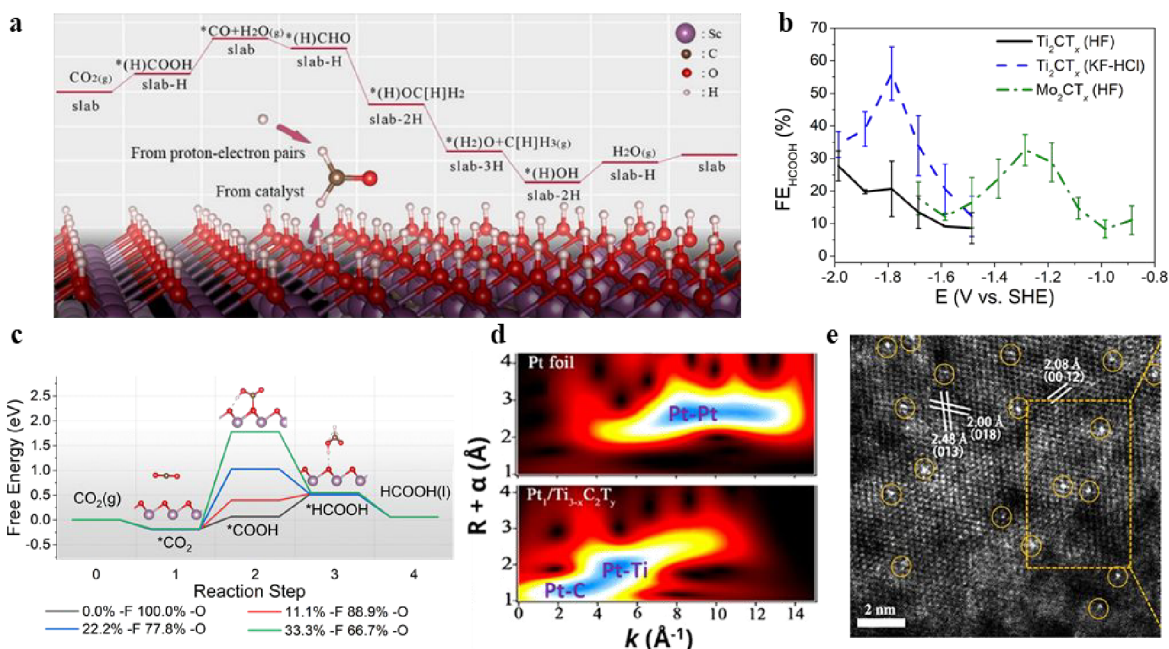
34 **MXene hybrids and composites for electrocatalytic/photocatalytic (EC/PC) carbon**  
35 **dioxide reduction (CO<sub>2</sub>RR).** MXenes synthesized to date are similar to the bulk 3D crystalline  
36 non-MXene TM carbides and nitrides in terms of high electronic conductivity.<sup>152,240</sup> Additionally,  
37 the MXenes' basal planes are terminated with T<sub>x</sub> groups in ambient conditions or electrolytes.<sup>241</sup>  
38 These T<sub>x</sub> groups usually comprise of electronegative elements (F, O, Cl) that can alter the MXenes'  
39 effective work function<sup>242,243</sup> and bring about unique MXene-intermediate molecule adsorbate  
40 interactions.<sup>23,244,245</sup> In CO<sub>2</sub>RR, these unusual interactions render alternative thermodynamic  
41 pathways that were previously and commonly unfavorable on TM catalysts, feasible, providing a  
42 means to circumvent the scaled binding energy relations.<sup>246</sup> Beyond providing active sites for  
43 CO<sub>2</sub>RR intermediates, Chen *et al.* described an interesting possibility of MXenes' T<sub>x</sub> groups being  
44  
45  
46  
47  
48  
49  
50  
51  
52  
53  
54  
55  
56  
57  
58  
59  
60

1  
2  
3 involved in the catalysis process.<sup>22</sup> The DFT scheme in **Figure 10a** describes how H atoms in the  
4  $T_x$  termination group can be “borrowed” by the intermediate during some of the proton-electron  
5 transfer steps, before being regenerated in the last three proton coupled electron transfer steps.  
6  
7  
8  
9

10  
11 Despite encouraging theoretical simulations, EC CO<sub>2</sub>RR catalysis by bare MXenes in  
12 aqueous electrolytes have yet to be reported, possibly due to the weaker CO<sub>2</sub>RR intermediate-  
13 MXenes binding strength, and severe competition from HER as a side-reaction.<sup>18</sup> Handoko *et al.*  
14 recently reported EC CO<sub>2</sub>RR on Ti<sub>2</sub>CT<sub>x</sub> and Mo<sub>2</sub>CT<sub>x</sub> MXenes in a mixture of acetonitrile, water,  
15 and 1-Butyl-3-methylimidazolium tetrafluoroborate (BMIMBF<sub>4</sub>).<sup>25</sup> Formic acid (HCOOH) was  
16 the main product, with peak HCOOH Faradaic efficiency (FE<sub>HCOOH</sub>, see **Vocabulary** for definition  
17 of FE) of 56% at -1.8 V (vs. standard hydrogen electrode, SHE) on Ti<sub>2</sub>CT<sub>x</sub> synthesized with KF-  
18 HCl (**Figure 10b**). Interestingly, higher activity and an earlier CO<sub>2</sub>RR onset potential was  
19 observed for MXenes with lower -F  $T_x$  content. This observation is explained by DFT calculations,  
20 which revealed that the critical step involving the \*COOH intermediate is more adversely affected  
21 by an increasing presence of -F  $T_x$  groups (**Figure 10c**).  
22  
23  
24  
25  
26  
27  
28  
29  
30  
31  
32  
33  
34  
35  
36

37 As such, we believe that MXene hybrids can offer a viable value proposition. In addition  
38 to their excellent electronic conductivity, thin MXene layers would be a superior catalyst support  
39 choice compared to other C-based materials, due to stronger metal-support interactions.<sup>247</sup>  
40 Furthermore, the possibility of intermetallic compound formation has been reported,<sup>248</sup> revealing  
41 an active surface with a unique electronic structure that is more resistant to agglomeration.<sup>249</sup> For  
42 example, Mo<sub>2</sub>CO<sub>2</sub> MXene has been predicted as a good Pd support.<sup>250</sup> Specifically, a more active  
43 Pd dimer species that allows for partial methane oxidation to methanol can be stabilized on  
44 Mo<sub>2</sub>CO<sub>2</sub> MXenes.<sup>250</sup>  
45  
46  
47  
48  
49  
50  
51  
52  
53  
54  
55  
56  
57  
58  
59  
60

In addition, MXenes have also been demonstrated to be suitable substrates for single atom catalysts (an emerging active frontier in heterogeneous catalysis<sup>251</sup>) such as Pt, Ru and Rh, through a simple self-reduction reaction at room temperature.<sup>252</sup> The single atom nature of PGMs substituting the Ti positions in  $\text{Ti}_3\text{C}_2\text{T}_x$  MXene was demonstrated with extended X-ray absorption fine structure (EXAFS, **Figure 10d**) spectroscopy and high-angular annular dark-field (HAADF) scanning transmission electron microscopy (STEM) imaging (**Figure 10e**).<sup>252</sup> In particular,  $\text{Pt}_1/\text{Ti}_{3-\delta}\text{C}_2\text{T}_x$  structures were reported to be active for  $\text{CO}_2$  activation with amines and silane into formamide at 140 °C with near-complete conversion and selectivity.<sup>252</sup>



**Figure 10.** MXenes for  $\text{CO}_2\text{RR}$ . (a) DFT scheme showing the possible involvement of  $\text{T}_x$  atoms in  $\text{CO}_2\text{RR}$  to  $\text{CH}_4$ . Adapted with permission from ref <sup>22</sup>. Copyright 2019 American Chemical Society. (b) Comparison of FE for  $\text{CO}_2\text{RR}$  to formic acid on  $\text{Ti}_2\text{CT}_x$  and  $\text{Mo}_2\text{CT}_x$ . Error bars represent one standard deviation of three independent measurements. (c) Calculated free energy diagram at 0 V applied potential for  $\text{CO}_2\text{RR}$  to formic acid on  $\text{Mo}_2\text{CT}_x$  MXenes with varying fractions of -F and -O surface  $\text{T}_x$  groups. Purple, red, brown and white spheres represent Mo, O, C and H atoms respectively. Adapted with permission from ref <sup>25</sup>. Copyright 2020 The Authors. (d) Two-dimensional wavelet transformation of Pt K-edge EXAFS (radial distance information in the y-axis and energy dependence  $k$ -space in the x-axis) and (e) HAADF STEM of  $\text{Pt}_1/\text{Ti}_{3-\delta}\text{C}_2\text{T}_x$ , which clearly demonstrates the absence of Pt-Pt bond in the single atom Pt-on- $\text{Ti}_3\text{C}_2\text{T}_x$  MXene. Adapted with permission from ref <sup>252</sup>. Copyright 2019 American Chemical Society.

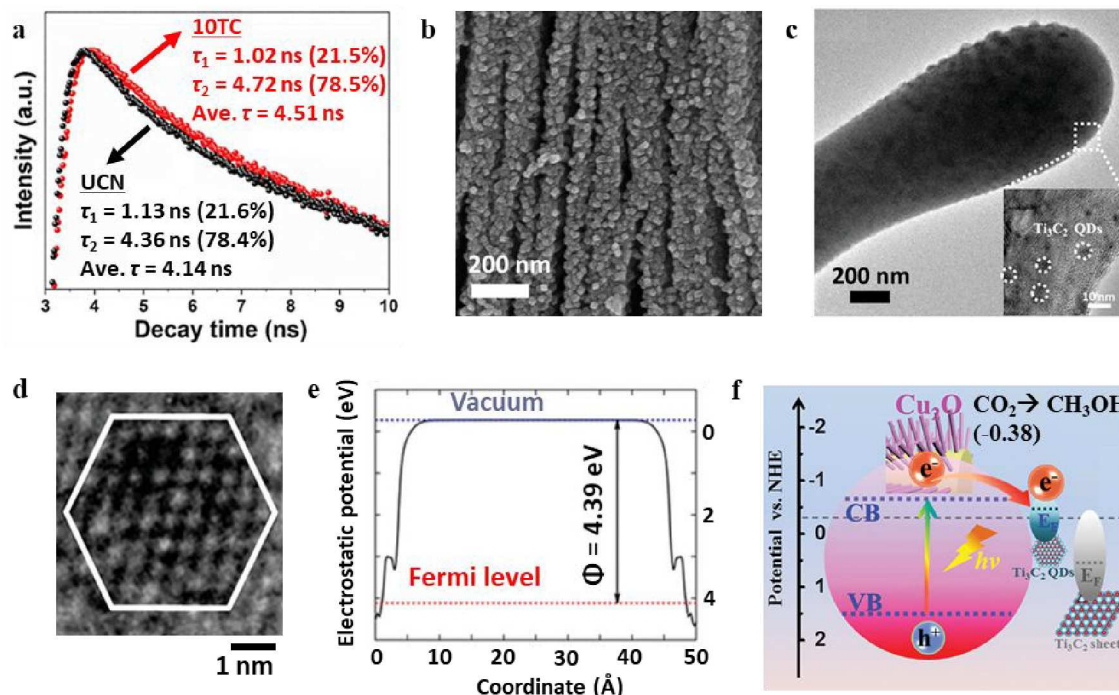
1  
2  
3 We note that most experimental CO<sub>2</sub>RR on MXenes or their hybrids were conducted using  
4 PC/PEC instead of EC. This is intriguing, as apart from the photophysical processes, PC should  
5 share many commonalities with EC.<sup>253</sup> Discrepancies between the measured activities of the same  
6 TM catalyst (or co-catalyst) species in EC and PC approaches have been reported.<sup>254</sup> These  
7 discrepancies can be partly attributed to the attenuated work function under steady state  
8 illumination and interfacial voltage loss,<sup>255</sup> limited cathodic potential range (*i.e.* conduction band  
9 position),<sup>256</sup> and temporal discontinuity between the photo-generated carrier lifetime (fs to ms) and  
10 reaction kinetics (ms to s).<sup>256,257</sup> Besides impacting catalytic activity, we believe that these  
11 differences may enhance the selectivity in PC CO<sub>2</sub>RR, as the diverse intermediate stability in  
12 CO<sub>2</sub>RR and rate of competitive HER is sensitive to the applied potential.<sup>202</sup>

13  
14  
15  
16  
17  
18  
19  
20  
21  
22  
23  
24  
25  
26  
27 A commonly adopted hybrid combination for PC CO<sub>2</sub>RR is MXenes coupled with a wider  
28 bandgap photo-absorber. MXenes made to date are metallic and some are predicted to have narrow  
29 bandgaps,<sup>258</sup> thus hybridization with a wider bandgap photo-absorber is the only way to generate  
30 sufficient photo-carriers for catalysis. A notable example is the Ti<sub>3</sub>C<sub>2</sub>T<sub>x</sub>/g-C<sub>3</sub>N<sub>4</sub> hybrid which  
31 produced 2.24–5.19 and 0.04–0.05 μmol g<sup>-1</sup> h<sup>-1</sup> of CO and CH<sub>4</sub> respectively.<sup>259,260</sup> Although g-  
32 C<sub>3</sub>N<sub>4</sub> is a very good photo-absorber with high quantum yield even at visible wavelengths ( $\lambda > 395$   
33 nm),<sup>261</sup> it is limited by rapid charge recombination.<sup>262</sup> The role of Ti<sub>3</sub>C<sub>2</sub>T<sub>x</sub> in the hybrid is likely  
34 that of a charge separator, as their work function position is suitably positioned to accept electrons  
35 from the g-C<sub>3</sub>N<sub>4</sub> conduction band, thus enhancing the photo-generated carrier lifetime (**Figure**  
36 **11a**).<sup>259</sup> The activity of Ti<sub>3</sub>C<sub>2</sub>T<sub>x</sub>/g-C<sub>3</sub>N<sub>4</sub> was further enhanced considerably by depositing Pd on  
37 the hybrid structure, which produced formate and methanol at a rate of 905 and 350 μmol g<sup>-1</sup> h<sup>-1</sup>,  
38 respectively, in a PEC setting.<sup>263</sup> Pd is a very interesting co-catalyst choice, because it is known to  
39 bind very strongly to adsorbed \*CO in EC CO<sub>2</sub>RR,<sup>264</sup> which often leads to catalyst deactivation.



1  
2  
3 The authors attributed the high activity of the  $\text{Ti}_3\text{C}_2\text{T}_x/\text{g-C}_3\text{N}_4/\text{Pd}$  hybrid to electron trapping by  
4  
5 protonic species on the Pd surface, but we speculate that the stronger binding may allow the key  
6  
7 \*CO intermediate to persist longer, allowing for photo-electron accumulation and transfer.  
8  
9

10  
11 Depending on the relative band positions, hybridization of metals (*i.e.* MXenes) with  
12  
13 semiconductors often results in a built-in Schottky junction. This increases the electronic transport  
14  
15 resistance and it is thus generally undesired. However, in PC, the Schottky barrier junction may  
16  
17 actually improve the overall carrier lifetime by minimizing the electron losses associated with back  
18  
19 injections. One example of the adoption of this strategy is reported in  $\text{Ti}_3\text{C}_2\text{T}_x/\text{CeO}_2$ , which  
20  
21 produced up to  $40.2 \mu\text{mol g}^{-1} \text{h}^{-1}$  of CO.<sup>265</sup> The built-in junction may also exist in many other  
22  
23 examples, especially in hybrids involving wide-bandgap *n*-type semiconductors such as  $\text{TiO}_2$ ,<sup>85</sup>  
24  
25  $\text{Bi}_2\text{WO}_6$ ,<sup>101</sup> or  $\text{CsPbBr}_3$ ,<sup>125</sup> although this is hard to ascertain as the MXenes' work function varies<sup>243</sup>  
26  
27 depending on the actual  $\text{T}_x$  composition in the reaction environment. Hybridization with these  
28  
29 semiconductors generally yield modest  $\text{CO}_2\text{RR}$  activity (**Table S4a**), of up to  $28 \mu\text{mol g}^{-1} \text{h}^{-1}$   
30  
31 products for  $\text{Ti}_3\text{C}_2\text{T}_x/\text{P25}/\text{TiO}_2$ .<sup>266</sup> While a slightly higher activity was observed for  
32  
33  $\text{Ti}_3\text{C}_2\text{T}_x/\text{CsPbBr}_3$  ( $32 \mu\text{mol g}^{-1} \text{h}^{-1}$  CO and  $14 \mu\text{mol g}^{-1} \text{h}^{-1}$   $\text{CH}_4$ ), the perovskite's ( $\text{CsPbBr}_3$ )  
34  
35 instability in aqueous solutions necessitated the use of ethyl acetate as the electrolyte.<sup>125</sup>  
36  
37  
38  
39  
40  
41  
42  
43  
44  
45  
46  
47  
48  
49  
50  
51  
52  
53  
54  
55  
56  
57  
58  
59  
60



**Figure 11.** MXene hybrids for PC/PEC  $\text{CO}_2\text{RR}$ . (a) Transient PL spectroscopy showing a longer photo-generated carrier lifetime for  $\text{Ti}_3\text{C}_2\text{T}_x/\text{g-C}_3\text{N}_4$  (10TC), compared to bare  $\text{g-C}_3\text{N}_4$  (UCN). Adapted with permission from ref <sup>259</sup>. Copyright 2020 Elsevier B.V. (b) Morphology of  $\text{Ti}_3\text{C}_2\text{T}_x/\text{TiO}_2$  after controlled calcination of  $\text{Ti}_3\text{C}_2\text{T}_x$  at  $550^\circ\text{C}$ . Adapted with permission from ref <sup>85</sup>. Copyright 2018 Elsevier Inc. (c) TEM image of  $\text{Ti}_3\text{C}_2\text{T}_x$  QD/ $\text{Cu}_2\text{O}$  and (d) HRTEM image of  $\text{Ti}_3\text{C}_2\text{T}_x$  QDs, showing hexagonal units. (e) DFT calculated Fermi level and (f) band diagram of  $\text{Ti}_3\text{C}_2\text{T}_x$  QD/ $\text{Cu}_2\text{O}$ . Adapted with permission from ref <sup>121</sup>. Copyright 2018 WILEY-VCH.

$\text{TiO}_2/\text{Ti}_3\text{C}_2\text{T}_x$  is another popular MXene hybrid for PC  $\text{CO}_2\text{RR}$ , since  $\text{TiO}_2$  can be naturally grown from *in-situ* conversion of Ti-based MXenes *via* partial oxidation. Under the right synthesis conditions, hierarchical hybrids were produced while retaining the conductive  $\text{Ti}_3\text{C}_2\text{T}_x$  backbone (Figure 11b).<sup>85</sup> The *in-situ* grown  $\text{TiO}_2/\text{Ti}_3\text{C}_2\text{T}_x$  hybrid, combined with Pd co-catalysts, is possibly the most active MXene hybrid for PEC  $\text{CO}_2\text{RR}$ , yielding a cocktail of products (formate, methanol, and ethanol) at a high total hydrocarbon yield of  $1840 \mu\text{mol g}^{-1} \text{h}^{-1}$ .<sup>92</sup> Separately, a different approach hybridized  $\text{Ti}_3\text{C}_2\text{T}_x$  with  $\text{Cu}_2\text{O}$  (Figure 11c).<sup>121</sup> Instead of using large MXenes flakes directly, tiny  $\text{Ti}_3\text{C}_2\text{T}_x$  QDs were prepared by rigorous sonication in inert argon. These MXene QDs were then treated with positively charged polyethylenimine to aid their electrostatic self-assembly with negatively charged polystyrene sulfonate-coated  $\text{Cu}_2\text{O}$  nanorods. The theoretical Fermi level

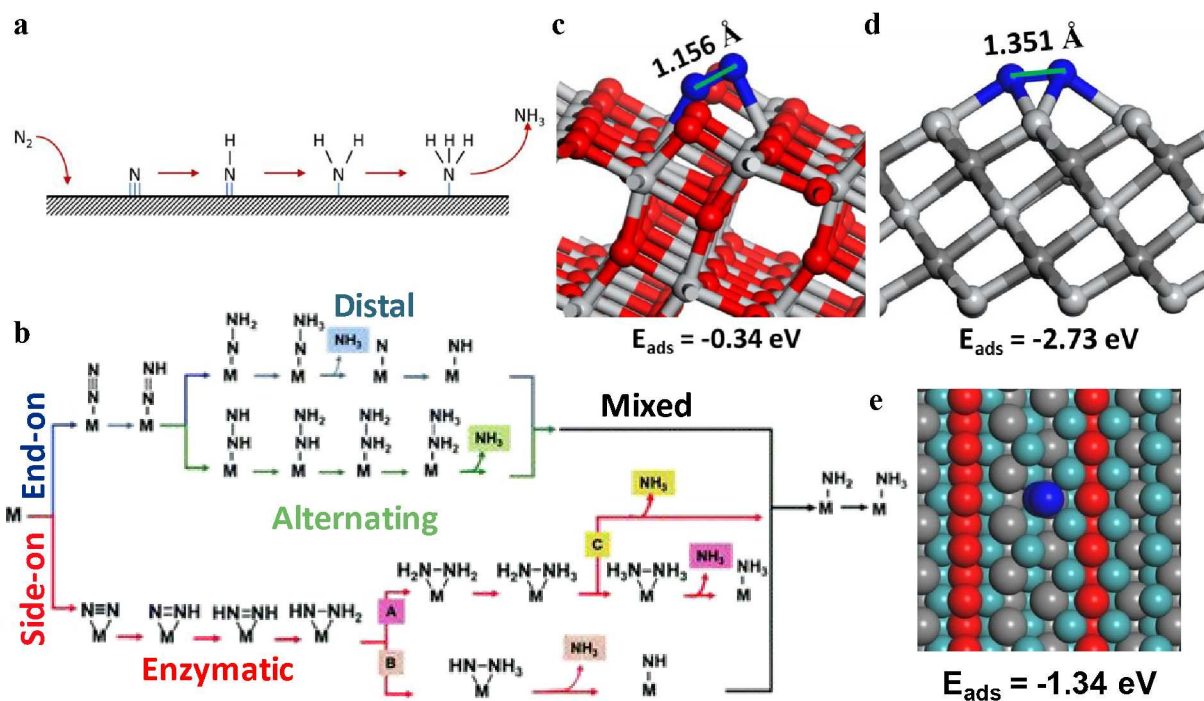
1  
2  
3 of the hexagonal  $\text{Ti}_3\text{C}_2\text{T}_x$  QDs was estimated to be significantly lower than the “bulk”  $\text{Ti}_3\text{C}_2\text{T}_x$   
4 sheets (**Figures 11d and 11e**), which resulted in more facile electron transfer from the  $\text{Cu}_2\text{O}$  photo-  
5 absorber, at a potential above the thermodynamic requirement for  $\text{CO}_2\text{RR}$  to methanol (-0.81 V  
6 vs. RHE, **Figure 11f**).<sup>202</sup> The  $\text{Ti}_3\text{C}_2\text{T}_x$  QD/ $\text{Cu}_2\text{O}$  hybrid supplied  $78.5 \mu\text{mol g}^{-1} \text{h}^{-1}$  of methanol.  
7  
8  
9

10  
11  
12  
13 Beyond  $\text{CO}_2\text{RR}$ , CdS/ $\text{Ti}_3\text{C}_2\text{T}_x$  was also shown to be active in the PC reduction of 4-  
14 nitroaniline to *p*-phenylenediamine (PPD),<sup>267</sup> an important synthetic intermediate for dyes and  
15 aramid fibers. While the PC activity of CdS in reducing aromatic nitro-compounds is not  
16 surprising, hybridization with MXenes significantly enhanced their activity and photo-stability. It  
17 was proposed that hybridization with CdS formed a Janus-like structure, characterized by the  
18 strong metallic adsorption of Cd onto  $\text{Ti}_3\text{C}_2\text{T}_x$ ,<sup>268</sup> thus limiting the dissolution of CdS. Similar  
19 strategies may therefore be extended to other TM chalcogenides for enhancing  $\text{CO}_2\text{RR}$  activity.  
20  
21  
22  
23  
24  
25  
26  
27  
28  
29

30 **MXenes hybrids and composites for electrocatalytic/photocatalytic (EC/PC) nitrogen**  
31 **reduction ( $\text{N}_2\text{RR}$ ).** The abundance of  $\text{N}_2$  in the air has attracted many attempts to convert them to  
32 nitrate and ammonium compounds for agricultural applications. Combined with steam reforming  
33 of natural gas, the Haber-Bosch process is still widely used in modern ammonia production plants  
34 worldwide today. Although the Haber-Bosch process is an exothermic reaction overall, it still  
35 requires a massive energy input to drive the  $\text{N}\equiv\text{N}$  bond dissociation ( $941 \text{ kJ mol}^{-1}$ ) through the  
36 dissociative pathway over a suitable catalyst (**Figure 12a**).<sup>269</sup>  
37  
38  
39  
40  
41  
42  
43  
44  
45  
46

47 EC/PC  $\text{N}_2\text{RR}$  offers an attractive alternative to the Haber-Bosch process. With the ability  
48 to be conducted under ambient conditions,  $\text{N}_2\text{RR}$  is potentially safer, cleaner, and a more  
49 sustainable way to produce  $\text{NH}_3$  with a smaller plant footprint when coupled with sustainable  
50 energy inputs. Unlike the Haber-Bosch process with a kinetically<sup>270</sup> (or thermodynamically,<sup>271</sup>  
51  
52  
53  
54  
55  
56  
57  
58  
59  
60

1  
2  
3 depending on the substrate) limited  $N\equiv N$  dissociation step, PC/EC  $N_2$ RR preferentially undergoes  
4 the associative pathway, whereby the adsorbed  $N_2$  molecule first undergoes stepwise  
5 protonation.<sup>269</sup> The associative  $N_2$ RR pathway diverges to three main pathways depending on the  
6 initial  $N_2$  adsorption geometry (**Figure 12b**): alternating and distal protonation mechanisms  
7 operate when  $N_2$  is adsorbed end-on, while the enzymatic mechanism operates after  $N_2$  is adsorbed  
8 side-on.<sup>272,273</sup> There are also possibilities of pathway inter-mixing, depending on the  
9 thermodynamic and kinetic barriers.<sup>274</sup> Side-on  $N_2$  adsorption is more favorable on the basal planes  
10 of bare  $M_2C$  MXenes,<sup>24,275,276</sup>  $M_3C_2$  MXenes with group 14 “M” elements (**Figure 12d**),<sup>277</sup> and  
11 ordered double TM  $Mo_2TiC_2T_x$  MXenes.<sup>278</sup> Conversely, distal adsorption is preferred on  $M_3C_2$   
12 MXenes with group 15 and 16 “M” elements.<sup>277</sup> However, it should be noted that bare MXenes  
13 are unlikely to be stable under  $N_2$ RR operating conditions,<sup>24</sup> and it is important to include the  
14 relevant  $T_x$  species when performing theoretical calculations. The  $T_x$  groups generally cause  $N_2$   
15 adsorption on MXenes to be more difficult,<sup>24</sup> although alternative adsorption sites can be provided  
16 by exposed “M” sites at the edges (**Figure 12e**),<sup>279</sup> or on single atom dopants.<sup>274</sup>  
17  
18  
19  
20  
21  
22  
23  
24  
25  
26  
27  
28  
29  
30  
31  
32  
33  
34  
35  
36  
37  
38  
39  
40  
41  
42  
43  
44  
45  
46  
47  
48  
49  
50  
51  
52  
53  
54  
55  
56  
57  
58  
59  
60



**Figure 12.** N<sub>2</sub>RR mechanistic study. (a) Dissociative N<sub>2</sub> reduction to NH<sub>3</sub>. Adapted with permission from ref <sup>269</sup>. Copyright 2016 Elsevier B.V. (b) Associative N<sub>2</sub> reduction to NH<sub>3</sub>, with diverging pathways depending on the adsorption geometry of the N<sub>2</sub> molecule. Adapted with permission from ref <sup>275</sup>. Copyright 2020 Royal Society of Chemistry. Schematics of side-on N<sub>2</sub> adsorption on (c) defective (101) TiO<sub>2</sub> surface with O-vacancy and on (d) Ti<sub>3</sub>C<sub>2</sub>T<sub>x</sub> MXene. Dark grey, red, light grey and blue balls represent C, O, Ti and N respectively. Adapted with permission from ref <sup>280</sup>. Copyright 2020 Elsevier B.V. (e) Alternative end-on N<sub>2</sub> adsorption on the exposed Ti site on Ti<sub>3</sub>C<sub>2</sub>O<sub>2</sub> MXene edges. Gray, red, sky blue and blue balls represent C, O, Ti and N respectively. Adapted with permission from ref <sup>279</sup>. Copyright 2018 Elsevier Inc.

Before discussing the catalytic N<sub>2</sub>RR activity of MXenes and their hybrids, it is imperative that we discuss the best activity reporting practices. A recurring issue in most PC/EC N<sub>2</sub>RR research is that the quantity of NH<sub>3</sub> product produced is very small, in the range of 10 to 1000 nmol,<sup>281</sup> and thus very susceptible to contamination and false positives. Therefore, establishing a suitable NH<sub>3</sub> detection protocol with robust control measurements is vital. There are two commonly adopted methods to quantify the produced NH<sub>3</sub> in solution: (1) colorimetric assays, including Nessler's reagent (Nessler) or Berthelot's reagent (*e.g.* indophenol blue, IB), and (2) ion chromatography (IC). While both methods generally work well in detecting low concentrations of

1  
2  
3 NH<sub>3</sub> (<500 μg L<sup>-1</sup>),<sup>282</sup> any impurities that result in false strong absorption in the detection  
4 wavelength, such as methanol and carbon particles, must be avoided in colorimetric-based  
5 methods. We note that the IB-based colorimetric assays are unsuitable for use at >500 μg L<sup>-1</sup> NH<sub>3</sub>,  
6 or in acidic media, due to higher deviations.<sup>282</sup> Finally, rigorous experimentation, including  
7 statistical reproducibility and confirmation that the NH<sub>3</sub> originated from N<sub>2</sub>RR, requires the use of  
8 isotopically labeled <sup>15</sup>N<sub>2</sub>. Detection of <sup>15</sup>NH<sub>3</sub> can be achieved using mass spectrometry, infrared,  
9 or nuclear magnetic resonance (NMR) spectroscopy.<sup>283</sup> For the reader's benefit, we report the NH<sub>3</sub>  
10 detection method, and whether <sup>15</sup>N isotope labeling control was performed in summary **Table S4b**.  
11  
12  
13  
14  
15  
16  
17  
18  
19  
20  
21

22 Ti<sub>3</sub>C<sub>2</sub>T<sub>x</sub> is the most commonly used MXene for PC/EC N<sub>2</sub>RR due to their stability<sup>284</sup> and  
23 close structural relationship with the popular TiO<sub>2</sub> photocatalyst. Ti<sub>3</sub>C<sub>2</sub>T<sub>x</sub> has been reported to  
24 perform EC N<sub>2</sub>RR with modest NH<sub>3</sub> yields (157–522 μmol g<sup>-1</sup> h<sup>-1</sup>) and FE at relatively low  
25 cathodic potentials (-0.1 to -0.4 V vs. RHE), with electrochemical and structural stability.<sup>239,279</sup>  
26 Investigations into MXene hybrids, especially through the use of single atom dopants, have  
27 predicted attractive N<sub>2</sub>RR activity, as the single atom dopants provide more favorable N<sub>2</sub>  
28 adsorption sites and correspondingly lower activation barriers. A range of *in-silico* single atom  
29 modifications (boron<sup>274</sup> and various TMs<sup>271,285,286</sup>) have been studied, with Ru, Mo, Ti, and Fe  
30 commonly identified as promising dopants with the least negative N<sub>2</sub>RR limiting potentials. Apart  
31 from calculating the lowest energy pathway from N<sub>2</sub> to NH<sub>3</sub>, it is also critical to evaluate the  
32 formation energy and the stability of the hybrid through first principle calculations, or from more  
33 realistic kinetic stability studies.<sup>287</sup>  
34  
35  
36  
37  
38  
39  
40  
41  
42  
43  
44  
45  
46  
47  
48  
49

50 Experimentally, Ti<sub>3</sub>C<sub>2</sub>T<sub>x</sub> has been used to support metallic N<sub>2</sub>RR electrocatalysts such as  
51 Ru (2321 μmol g<sup>-1</sup> h<sup>-1</sup> and 13% FE)<sup>288</sup> and fine (<10 nm) Au NPs (1761 μmol g<sup>-1</sup> h<sup>-1</sup> and 18.3%  
52 FE),<sup>289</sup> with up to 14 times higher N<sub>2</sub>RR activity than bare Ti<sub>3</sub>C<sub>2</sub>T<sub>x</sub>. Enhanced N<sub>2</sub> adsorption and  
53  
54  
55  
56  
57  
58  
59  
60

1  
2  
3 \*N<sub>2</sub> coverage was a reason for the high catalytic activity on fine Au NPs/Ti<sub>3</sub>C<sub>2</sub>T<sub>x</sub>, as shown in the  
4 desorption profile (**Figure 13a**). Despite numerous encouraging predictions of N<sub>2</sub>RR on single-  
5 atom/MXene hybrids, only one example was reported experimentally, using Ru single  
6 atoms/Mo<sub>2</sub>CT<sub>x</sub>.<sup>290</sup> This hybrid electrocatalyst is highly N<sub>2</sub>RR active, yielding 2382 μmol g<sup>-1</sup> h<sup>-1</sup>  
7 NH<sub>3</sub> at a significant 25.7% FE. The N<sub>2</sub>RR active site was investigated using *operando* Ru K-edge  
8 X-ray absorption near edge structure (XANES). A slight increase in the Ru oxidation state to +3.56  
9 was observed when N<sub>2</sub> was introduced without bias (at open circuit potential, OCP) compared to  
10 the baseline measurement in Ar (+3.27), attributed to the electron back-donation when the Ru-N<sub>2</sub>  
11 bond was formed. The oxidation state reduces back to +3.15 when a N<sub>2</sub>RR-relevant potential (-0.3  
12 V vs. RHE) was applied, indicating N<sub>2</sub>RR. This phenomenon was also observed in the Fourier  
13 transformed-XANES (FT-XANES, **Figure 13b**). A discernible shift in the first neighbor peak to  
14 a shorter apparent distance of 1.51 Å was seen when N<sub>2</sub> was introduced, which reverted back to  
15 1.56 Å during N<sub>2</sub>RR, possibly due to Ru–N coordination during adsorption.  
16  
17  
18  
19  
20  
21  
22  
23  
24  
25  
26  
27  
28  
29  
30  
31  
32  
33

34 Beyond metallic catalysts, Ti<sub>3</sub>C<sub>2</sub>T<sub>x</sub> was also combined with TM oxide catalysts such as  
35 Mn<sub>x</sub>O<sub>y</sub>.<sup>291</sup> Manganese oxides are N<sub>2</sub>RR active, but exist in many structures with poor conductivity  
36 that limit their EC N<sub>2</sub>RR performance. Hybridizing MnO<sub>2</sub> with Ti<sub>3</sub>C<sub>2</sub>T<sub>x</sub> MXenes yielded up to  
37 2003 μmol g<sup>-1</sup> h<sup>-1</sup> NH<sub>3</sub> (11.39% FE) and traces of N<sub>2</sub>H<sub>2</sub> at -0.55 V vs. RHE.<sup>291</sup> The superior N<sub>2</sub>RR  
38 activity of Ti<sub>3</sub>C<sub>2</sub>T<sub>x</sub>/MnO<sub>2</sub> was ascribed to multiple advantages provided by the Ti<sub>3</sub>C<sub>2</sub>T<sub>x</sub> support:  
39 (1) prevention of MnO<sub>2</sub> aggregation, (2) facilitation of electron transfer to MnO<sub>2</sub> and avoidance of  
40 parasitic current loss, and (3) larger surface area with favorable adsorption and active sites.  
41  
42  
43  
44  
45  
46  
47  
48  
49  
50

51 As discussed earlier, Ti<sub>3</sub>C<sub>2</sub>T<sub>x</sub> is a good precursor for *in-situ* conversion to Ti<sub>3</sub>C<sub>2</sub>T<sub>x</sub>/TiO<sub>2</sub>  
52 hybrids. It is interesting that Ti<sub>3</sub>C<sub>2</sub>T<sub>x</sub>/TiO<sub>2</sub> hybrids can display EC N<sub>2</sub>RR activity with modest NH<sub>3</sub>  
53 yield (1545–1889 μmol g<sup>-1</sup> h<sup>-1</sup>) and FE (8.42–16.07%) in aqueous solutions,<sup>91,292</sup> despite potential  
54  
55  
56  
57  
58  
59  
60

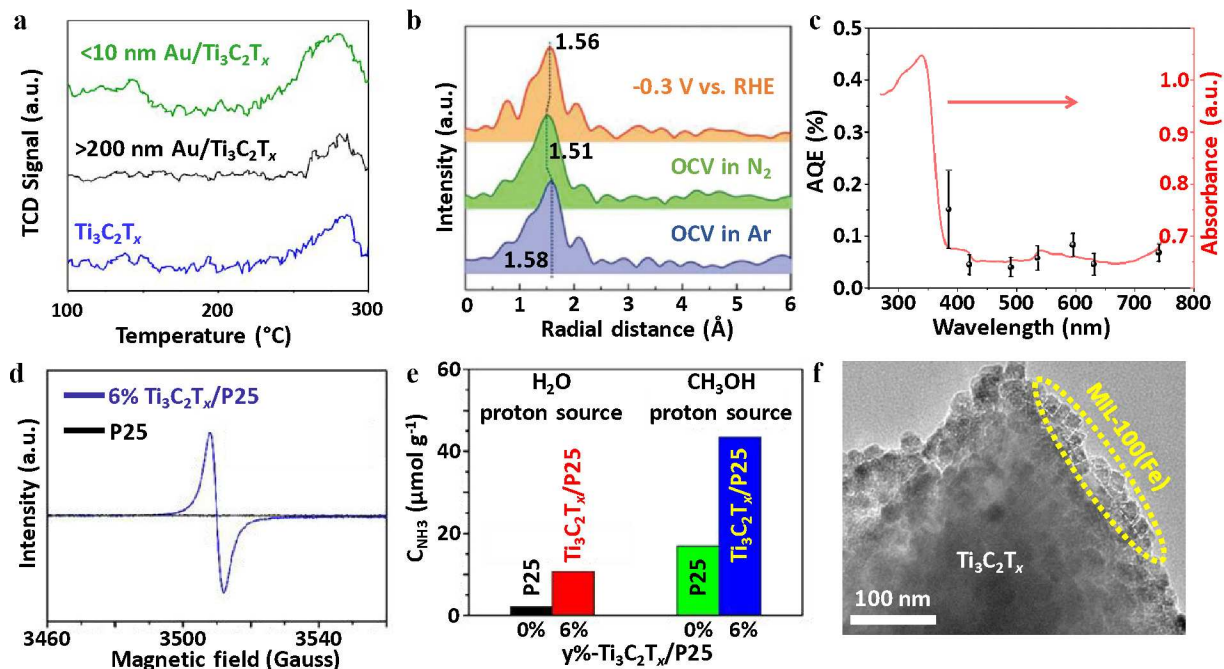


1  
2  
3 competition from HER and the poor conductivity of TiO<sub>2</sub>. Expectedly, there are many more  
4 examples of Ti<sub>3</sub>C<sub>2</sub>T<sub>x</sub>/TiO<sub>2</sub> hybrids reported for PC than EC N<sub>2</sub>RR to utilize TiO<sub>2</sub> as a photocatalyst.  
5  
6 The highest PC NH<sub>3</sub> yield using MXene hybrids so far is reported by Hou *et al.* (422 μmol g<sup>-1</sup> h<sup>-1</sup>).<sup>86</sup> This recent work demonstrated that the hybrid's photo-response extends up to the near-  
7 infrared region. A significant yield (82 μmol g<sup>-1</sup> h<sup>-1</sup>) was still detectible at 740 nm irradiation,  
8 corresponding to an apparent quantum efficiency (AQE) of 0.07% (**Figure 13c**).<sup>86</sup> Liao *et al.*  
9 recently investigated the role of Ti<sub>3</sub>C<sub>2</sub>T<sub>x</sub> in enhancing TiO<sub>2</sub> N<sub>2</sub>RR activity.<sup>280</sup> In this work, the  
10 authors mixed P25 TiO<sub>2</sub> (80% anatase and 20% rutile phase) with Ti<sub>3</sub>C<sub>2</sub>T<sub>x</sub> and treated them in N<sub>2</sub>  
11 atmosphere. Interestingly, the hybridization process introduced significant O-vacancies in TiO<sub>2</sub>,  
12 as indicated by the broadening of the Raman peak around 1500 cm<sup>-1</sup>, and a strong low temperature  
13 electron spin resonance (ESR) signal (**Figure 13d**). The defective TiO<sub>2</sub> sites acted as an alternative  
14 adsorption site (**Figure 12c**) alongside Ti<sub>3</sub>C<sub>2</sub> (**Figure 12d**), which enabled a higher coverage of  
15 adsorbed \*N<sub>2</sub>. At the optimum Ti<sub>3</sub>C<sub>2</sub>T<sub>x</sub> loading of 6%, the NH<sub>3</sub> yield of the hybrid was 10.74 μmol  
16 g<sup>-1</sup> h<sup>-1</sup> without any sacrificial reagents. The NH<sub>3</sub> yield was further enhanced to 43.44 μmol g<sup>-1</sup> h<sup>-1</sup>  
17 after 0.02 M CH<sub>3</sub>OH was added as a sacrificial electron donor (**Figure 13e**), indicating that the  
18 anodic reaction (water oxidation) is still a significant bottleneck.  
19  
20  
21  
22  
23  
24  
25  
26  
27  
28  
29  
30  
31  
32  
33  
34  
35  
36  
37  
38  
39  
40

41 Alternatively, the oxidation of Ti<sub>3</sub>C<sub>2</sub>T<sub>x</sub> to TiO<sub>2</sub> can be fully completed, resulting in a unique  
42 MXene-derived TiO<sub>2</sub> structure with many Ti<sup>3+</sup> sites, which are inherently more active  
43 catalytically.<sup>293</sup> These MXene-derived hybrids were used for EC and PC N<sub>2</sub>RR. Using *in-situ*  
44 oxidation, a more complex MXene-derived hybrid of TiO<sub>2</sub>@C/g-C<sub>3</sub>N<sub>4</sub> was also produced from  
45 Ti<sub>3</sub>C<sub>2</sub>T<sub>x</sub> for PC N<sub>2</sub>RR.<sup>293</sup> This structure was demonstrated to be an efficient and stable N<sub>2</sub>RR  
46 photocatalyst with an NH<sub>3</sub> production rate of 250.6 μmol g<sup>-1</sup> h<sup>-1</sup>. The outstanding NH<sub>3</sub> production  
47  
48  
49  
50  
51  
52  
53  
54  
55  
56  
57  
58  
59  
60



performance was attributed to the abundance of surface defects, efficient electron-donation, suitable light harvesting, small transition impedance, and strong N<sub>2</sub> adsorption.



**Figure 13.** MXene hybrids for N<sub>2</sub>RR. (a) N<sub>2</sub> temperature programmed desorption profile of Ti<sub>3</sub>C<sub>2</sub>T<sub>x</sub>, <10 nm Au/Ti<sub>3</sub>C<sub>2</sub>T<sub>x</sub> hybrid, and >200 nm Au/Ti<sub>3</sub>C<sub>2</sub>T<sub>x</sub> hybrid. A broad peak around 130 °C signifies N<sub>2</sub> physisorption, while the band closer to 280 °C represents N<sub>2</sub> chemisorption. Adapted with permission from ref<sup>289</sup>. Copyright 2019 American Chemical Society. (b) FT-EXAFS spectra derived from the normalized *operando* Ru K-edge XANES spectra for single atom Ru-Mo<sub>2</sub>CT<sub>x</sub> under various applied voltages vs. RHE in 0.5 M K<sub>2</sub>SO<sub>4</sub>. Adapted with permission from ref<sup>290</sup>. Copyright 2020 WILEY-VCH. (c) AQEs for N<sub>2</sub> fixation on Ti<sub>3</sub>C<sub>2</sub>T<sub>x</sub>/TiO<sub>2</sub> under monochromatic light irradiation. Adapted with permission from ref<sup>86</sup>. Copyright 2020 Elsevier B.V. (d) ESR spectra of bare P25 and 6% Ti<sub>3</sub>C<sub>2</sub>T<sub>x</sub>/P25 hybrid, (e) NH<sub>3</sub> yield after 1 h N<sub>2</sub>RR on 0% (bare P25) and 6% Ti<sub>3</sub>C<sub>2</sub>T<sub>x</sub>/P25 hybrid, in H<sub>2</sub>O and with 0.2 M CH<sub>3</sub>OH. Adapted with permission from ref<sup>280</sup>. Copyright 2020 Elsevier B.V. (f) HRTEM of 15%-Ti<sub>3</sub>C<sub>2</sub>T<sub>x</sub>/MIL-100(Fe) hybrid. Adapted with permission from ref<sup>294</sup>. Copyright 2019 American Chemical Society.

Apart from N<sub>2</sub>RR, NO oxidation is another pathway for nitrogen fixation and air pollution elimination, since NO accounts for 95% of all the NO<sub>x</sub> contaminations in air.<sup>294</sup> Wang *et al.* reported the PC oxidation of NO by the Ti<sub>3</sub>C<sub>2</sub>T<sub>x</sub>/MIL-100(Fe) MOF hybrid (**Figure 13f**). This work found that 58% NO was eliminated by the hybrid containing 15 wt% Ti<sub>3</sub>C<sub>2</sub>T<sub>x</sub>, which was 2.8 and 4.1 times more efficient than the bare MIL-100(Fe) MOF and Ti<sub>3</sub>C<sub>2</sub>T<sub>x</sub> MXene, respectively.

1  
2  
3 The enhanced NO oxidation was due to synergistic effects in the as-formed Schottky junction:  
4  $Ti_3C_2T_x$  acted as an electron conductor and accumulated electrons on surface to promote  $O_2RR$   
5 and form  $\cdot O_2^-$ . Both the generated  $\cdot O_2^-$  and  $h^+$  active species on the surface of MIL-100(Fe) then  
6  
7 oxidized NO to  $NO_3^-$  in the presence of water.  
8  
9  
10  
11  
12

13 **Summary, specific challenges, and outlook for EC/PC  $CO_2RR$  and  $N_2RR$ .** Thus far,  
14 we have elaborated on how MXene hybrids have found their way into emerging catalytic reactions  
15 (of  $CO_2$ ,  $N_2$  and related compounds), functioning either as support or active materials. Although  
16 the use of MXenes in these emerging catalytic reactions is nascent and has yet to result in record  
17 performance metrics, it provides a variety of different reaction pathways and is a welcome addition  
18 as an alternative catalyst support choice. We predict that the role of MXenes in these emerging  
19 reactions will continue to grow as we discover more MXene hybrids and learn more about their  
20 unique interactions with reaction intermediates and other co-catalysts. A summary table of  
21 performance metrics for various MXene hybrids in EC/PC  $CO_2RR$  and  $N_2RR$  is provided in  
22 **Tables S4a and S4b** respectively.  
23  
24  
25  
26  
27  
28  
29  
30  
31  
32  
33  
34  
35  
36

37 Specifically, we identify that the MXene/single atom hybrid is a worthwhile opportunity  
38 to pursue due to the many encouraging computational predictions but minimal experimental  
39 demonstrations. Single atom catalysis is a rapidly expanding field whereby methods of  
40 synthesizing and stabilizing these single atoms are quickly being developed.<sup>251</sup> Related to this  
41 point, mechanistic studies into MXene/single atom hybrids have not been established and is thus  
42 open for investigation, especially on the dynamic behavior of these single atom catalysts during  
43 catalytic reactions. Although the evidences so far suggest that single atom dopants are the active  
44 species, the catalytic action may also rely on the adsorbate interactions with the MXene catalyst  
45 support, for example through stepwise or cascading reactions. We foresee that *operando*  
46  
47  
48  
49  
50  
51  
52  
53  
54  
55  
56  
57  
58  
59  
60

1  
2  
3 techniques capable of discerning transient catalyst state and surface adsorbates, such as resonant  
4 inelastic X-ray scattering and SECM, will play an important role here.  
5  
6

7  
8  
9 Another interesting research opportunity lies in bridging the gap in understanding between  
10 the PC and EC operating modes of CO<sub>2</sub>RR and N<sub>2</sub>RR on MXenes and their hybrids. We note that  
11 most direct experimental CO<sub>2</sub>RR on MXene hybrids have been reported on PC compared to EC,  
12 possibly pointing to the direction of an indirect electron transfer driven reaction. In PC reactions,  
13 HER appears to be less severe a problem, even if these reactions (CO<sub>2</sub>RR, N<sub>2</sub>RR) are conducted  
14 in aqueous electrolytes. Although it is possible to run EC CO<sub>2</sub>RR or N<sub>2</sub>RR in non-aqueous  
15 electrolytes,<sup>25</sup> it is still important to improve our understanding on how to limit the HER side-  
16 reaction and run EC CO<sub>2</sub>RR or N<sub>2</sub>RR more economically in aqueous solutions. Some strategies  
17 for theoretical and experimental investigations are thus required (*e.g.* decoupling the lifetime of  
18 photo-generated carriers with the reaction dynamics). Additionally, studying how to tune the Fermi  
19 level of MXenes with different T<sub>x</sub> groups and the coupled co-catalyst is important to ensure the  
20 efficient photo-carrier movement towards the desired surface.  
21  
22  
23  
24  
25  
26  
27  
28  
29  
30  
31  
32  
33  
34  
35  
36

37 We also see a huge opportunity from MXene-derived materials in catalysis. Although this  
38 class of material does not fit the MXene hybrids category strictly, we recognize that the resulting  
39 MXene-derived materials behave differently and are much more active than those obtained using  
40 conventional methods. While many examples of TiO<sub>2</sub> hybrids have been derived from Ti-based  
41 MXenes, far fewer have reported using other MXenes. In particular, group 14, 15, and 16 TM  
42 MXene-derived materials could hold interesting properties for CO<sub>2</sub>RR and N<sub>2</sub>RR.  
43  
44  
45  
46  
47  
48  
49  
50  
51  
52  
53  
54  
55  
56  
57  
58  
59  
60

## CONCLUDING REMARKS AND FUTURE OUTLOOK

In this review, we discussed the design rules behind MXene hybrids for catalytic energy storage and conversion applications. We summarized the different classes of secondary materials hybridized with MXenes and their synthesis methods, highlighting their differences. By carefully considering the MXenes' properties ( $T_x$  groups, basal plane defects, edge charges, and identity of the outer metal surface), a variety of secondary materials can be chemically coupled with MXenes to form MXene hybrids with varying architectures, from vertically-aligned nanomaterials on MXenes to lateral coverages of MXenes and even more complex 3D mesoporous structures.

In general, MXenes and their hybrids are susceptible to oxidative degradation in environments containing water and/or oxygen,<sup>193</sup> and under applied anodic potentials in aqueous media,<sup>29</sup> both of which are common in catalysis. The MXenes' instability should thus be thoughtfully considered when designing MXene hybrids for energy storage and conversion. This can be circumvented through recent advances in the synthesis (F-free<sup>295</sup> and/or aqueous-free<sup>296,297</sup>), storage,<sup>193,298</sup> and stabilization (in thin films<sup>299</sup> or colloids<sup>300</sup>) of MXenes. These breakthroughs also offer greater flexibility and control of surface  $T_x$  groups for targeted hybrid assembly. This can be translated to the preparation of stable MXenes and their hybrids for water-sensitive applications, such as non-polar organic composites, polymer inks for additive manufacturing, and organic electrolytes for supercapacitors and batteries,<sup>301,302</sup> and are also highly relevant for communities working on flexible electronics, biomedical, and electromagnetic applications.

Additionally, we expect directed efforts to be made beyond mono-metal MXenes to synthesize multi-metal MXenes such as ordered double MXenes ( $M'_2MC_2T_x$  and  $M'_2M_2C_3T_x$ ), which have already been theoretically predicted to possess high levels of HER activity.<sup>303</sup> Adding

1  
2  
3 to the already-growing MXenes family, disordered double TM solid solution MXenes such as  
4  
5  $(\text{Ti},\text{V})_2\text{CT}_x$  and  $(\text{Mo},\text{V})_4\text{C}_3\text{T}_x$  are also attractive prospects for synthesis and characterization, given  
6  
7 the ease of tuning their electrochemical and physical properties based on their compositions.<sup>84,304</sup>  
8  
9  
10 Another key challenge lies in the expansion of existing etching methods to ternary transition metal  
11  
12 nitrides MAX materials to produce nitride MXenes, since only  $\text{Ti}_2\text{NT}_x$  has been produced in this  
13  
14 manner,<sup>305</sup> while  $\text{Ti}_4\text{N}_3\text{T}_x$  has only been synthesized through harsh molten fluoride salt  
15  
16 etching.<sup>19,201</sup> Other Mo-containing nitride MXenes are instead produced through ammoniating  
17  
18 their corresponding carbide MXenes with  $\text{NH}_3$  gas at a similarly high temperature of  $600^\circ\text{C}$ .<sup>306</sup>  
19  
20 Additionally, closely related 2D MXene-like TM nitrides, such as MoN, have also been reported  
21  
22 to be catalytically active for energy storage and conversion applications.<sup>307–309</sup> Investigating these  
23  
24 layered 2D MXene-like TM nitrides can potentially reveal important insights into the predicted  
25  
26 stability and chemical reactivity of MXene nitrides. In all, expanding the MXenes family can create  
27  
28 more possibilities in advanced MXene hybrid design to realize theoretically predicted properties  
29  
30 and competitive performances as multi-functional MXene hybrids and composites.  
31  
32  
33  
34  
35

36 For each of the industrially relevant catalytic energy storage (metal-air/sulfur batteries) and  
37  
38 conversion (water splitting, HER, OER,  $\text{CO}_2\text{RR}$  and  $\text{N}_2\text{RR}$ ) applications, we clarified the roles of  
39  
40 each material component in the MXene hybrids – a conductive support, co-catalyst, electronic  
41  
42 structure modulator, photo-carrier generator and phase stabilizer, to name a few. More importantly,  
43  
44 we described how strong chemical and electronic coupling within the hybrid can induce directed  
45  
46 morphological growth, alter the electronic structure, and create more catalytically active motifs for  
47  
48 synergistic enhancement in catalytic activity and stability. By combining  $\text{T}_x$  control, doping and  
49  
50 hybridization to modulate the electronic density and intrinsic activity of active site, coupled with  
51  
52 nanostructuring to increase the density and accessibility of those active sites, many MXene hybrids  
53  
54  
55  
56  
57  
58  
59  
60

1  
2  
3 have outperformed their separate individual components in both catalytic activity and stability. We  
4 also provide application-specific challenges and our outlook at the end of each application section  
5  
6 for readers working on those applications. A summary of key performance metrics for HER, OER,  
7  
8 ORR, CO<sub>2</sub>RR and N<sub>2</sub>RR is provided in **Tables S2–S4** for the reader's convenience.  
9

10  
11  
12  
13 MXene hybrids and composites have achieved superior catalytic energy storage and  
14 conversion performances compared to traditional materials, and we anticipate further advances as  
15 the chemical and electronic nature of the MXene hybrid interfaces are elucidated using a powerful  
16 combination of *in-situ/operando* experiments and theoretical modelling.<sup>21,202,238</sup> A better  
17 understanding of the dynamics at the MXenes' hybrid surface and interface in the presence of  
18 reactive species, solvent, and applied potential is indispensable toward building a more realistic  
19 and multi-scale MXene hybrid model that incorporates the effects of electrochemical potential,  
20 solvation, and micro-kinetics into the current purely atomistic view of DFT, as recently  
21 demonstrated on metallic catalysts.<sup>310–312</sup> So far, *operando* measurements demonstrated on bare  
22 MXenes<sup>19</sup> have clarified our fundamental understanding of the localized electrochemical activity  
23 and electronic structure at the catalytic surface. For this purpose, it is not unreasonable to use  
24 MXene-like surrogate structures that can be synthesized using bottom-up approaches with atomic  
25 precision (CVD and ALD) for such fundamental studies.<sup>65,66,148</sup>  
26  
27  
28  
29  
30  
31  
32  
33  
34  
35  
36  
37  
38  
39  
40  
41  
42  
43

44 Finally, efforts can be undertaken in the development of mild and scalable top-down  
45 MXene synthesis and hybridization techniques to (1) minimize MXene oxidation and mechanical  
46 damage during processing especially at high temperatures,<sup>192,193</sup> (2) enable greater control over the  
47 chemical composition, morphology and distribution of the secondary material grown on MXenes,  
48 and (3) realize highly porous and 3D MXene hybrid networks for efficient mass and long-range  
49 charge transport to further enhance catalytic activity.<sup>169</sup> Given the rapid rise in interest amongst  
50  
51  
52  
53  
54  
55  
56  
57  
58  
59  
60

1  
2  
3 MXene hybrids and composites, we expect an increase in both experimental and theoretical efforts  
4  
5 towards developing MXene hybrids for clean energy and related applications in the near future.  
6  
7  
8  
9  
10  
11  
12  
13  
14  
15  
16  
17  
18  
19  
20  
21  
22  
23  
24  
25  
26  
27  
28  
29  
30  
31  
32  
33  
34  
35  
36  
37  
38  
39  
40  
41  
42  
43  
44  
45  
46  
47  
48  
49  
50  
51  
52  
53  
54  
55  
56  
57  
58  
59  
60

1  
2  
3 ASSOCIATED CONTENT  
4  
5

6 The authors declare no competing financial interests.  
7  
8

9  
10 **Supporting Information.**  
11

12  
13 Detailed data entries (categorization of MXene hybrid publications, electrocatalytic  
14 HER/OER/ORR performances, photocatalytic HER performances, photo/electrocatalytic  
15 CO<sub>2</sub>RR/N<sub>2</sub>RR performances) is available free of charge in the Supporting Information online.  
16  
17  
18  
19

20  
21 AUTHOR INFORMATION  
22

23  
24 **Corresponding Author**  
25

26  
27 \*Z. W. Seh: [sehzw@imre.a-star.edu.sg](mailto:sehzw@imre.a-star.edu.sg)  
28

29  
30 \*B. Anasori: [banasori@iupui.edu](mailto:banasori@iupui.edu)  
31  
32

33 **Author Contributions**  
34

35 The manuscript was written through contributions of all authors. All authors have given approval  
36 to the final version of the manuscript.  
37  
38  
39

40  
41 ACKNOWLEDGEMENT  
42

43  
44 This work was supported by the Singapore National Research Foundation (NRF-NRFF2017-04).  
45 H.-Y.J. acknowledges the National Natural Science Foundation of China (NSFC, No. 21703170)  
46 and Key Research and Development Program of Shaanxi (Program No. 2020GY-244). J.T.  
47 acknowledges the RS International Exchanges 2017 Cost Share Award (IEC\NSFC\170342) and  
48 the Leverhulme Trust (RPG-2017-122).  
49  
50  
51  
52  
53  
54  
55  
56  
57  
58  
59  
60



## VOCABULARY

**MXene hybrid/composite**, a material fabricated by combining MXenes with another at least one other non-MXene material (metal, semiconductor or insulator) to form at least one interface. A hybrid/composite material is a more general classification than a heterostructure (see definition for heterostructure below).

**MXene heterostructure**, a material fabricated by growing at least one non-MXene material on MXenes in a repetitive layered manner, which forms more than one MXene-other material interface that repeats itself *i.e.* MXene-other material-MXene-other material-... and so on.

**(Photo)electrocatalyst**, a material that reduces the activation energy and overpotential (see definition for overpotential below) to drive an electrochemical reaction of interest, such as HER, OER, ORR, CO<sub>2</sub>RR and N<sub>2</sub>RR.

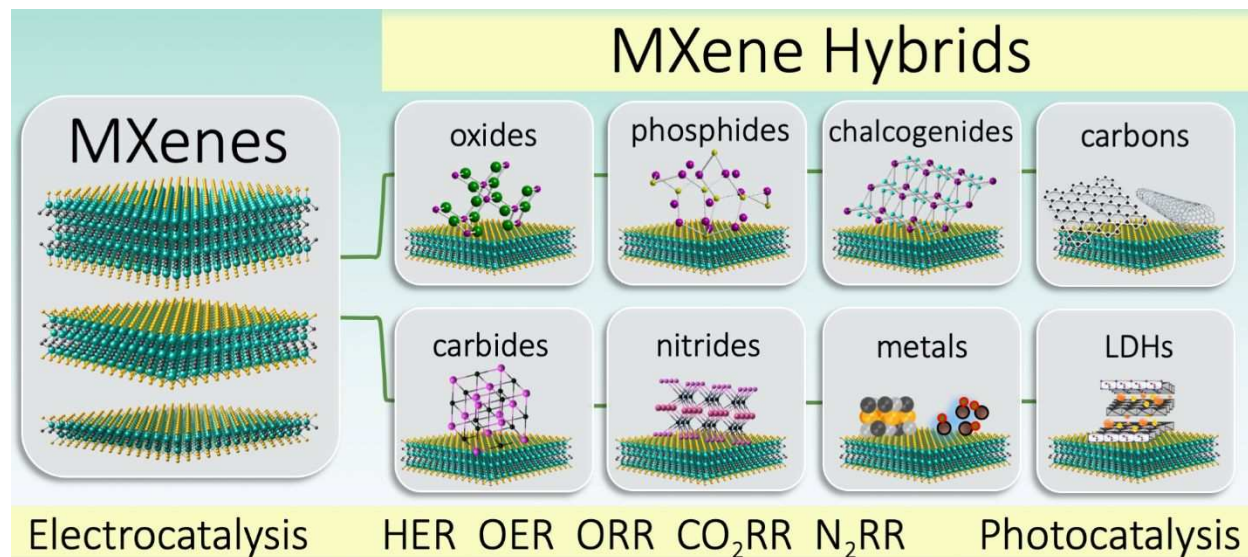
**Overpotential (at -10 mA cm<sup>-2</sup> current density)  $\eta_{j=10}$** , the additional potential difference (voltage) beyond the thermodynamically determined redox potential to drive an electrochemical redox half-cell reaction at a specific current density.

**Tafel slope**, the amount of increase in overpotential required to increase the current density produced for an electrochemical redox half-cell reaction by a factor of ten.

**Metal-air/sulfur battery**, two different battery architectures for energy storage. Metal-air/sulfur batteries use a metal anode and an air/sulfur cathode. The redox half-cell reactions occurring at the cathode are OER/ORR for metal-air batteries and S-redox reactions for metal-sulfur batteries.

1  
2  
3 **Faradaic efficiency**, the ratio of the number of electrons used to produce the desired  
4 electrochemical product compared to the total number of electrons added into the system. For  
5 example, a 70% Faradaic efficiency in CO<sub>2</sub>RR to CH<sub>4</sub> indicates that 70% of the electrons added  
6 are used to reduce CO<sub>2</sub> to CH<sub>4</sub> while the other 30% of electrons added are used to reduce CO<sub>2</sub> to  
7 other products.  
8  
9  
10  
11  
12  
13  
14  
15  
16  
17  
18  
19  
20  
21  
22  
23  
24  
25  
26  
27  
28  
29  
30  
31  
32  
33  
34  
35  
36  
37  
38  
39  
40  
41  
42  
43  
44  
45  
46  
47  
48  
49  
50  
51  
52  
53  
54  
55  
56  
57  
58  
59  
60

TOC FIGURE (can be rescaled to 9 cm width × 4 cm height)



## REFERENCES

- (1) Chu, S.; Majumdar, A. Opportunities and Challenges for a Sustainable Energy Future. *Nature* **2012**, *488*, 294–303.
- (2) Armstrong, R. C.; Wolfram, C.; de Jong, K. P.; Gross, R.; Lewis, N. S.; Boardman, B.; Ragauskas, A. J.; Ehrhardt-Martinez, K.; Crabtree, G.; Ramana, M. V. The Frontiers of Energy. *Nat. Energy* **2016**, *1*, 15020.
- (3) Seh, Z. W.; Kibsgaard, J.; Dickens, C. F.; Chorkendorff, I.; Nørskov, J. K.; Jaramillo, T. F. Combining Theory and Experiment in Electrocatalysis: Insights into Materials Design. *Science* **2017**, *355*, eaad4998.
- (4) Di, J.; Yan, C.; Handoko, A. D.; Seh, Z. W.; Li, H.; Liu, Z. Ultrathin Two-Dimensional Materials for Photo- and Electrocatalytic Hydrogen Evolution. *Mater. Today* **2018**, *21*, 749–770.
- (5) Chia, X.; Pumera, M. Characteristics and Performance of Two-Dimensional Materials for Electrocatalysis. *Nat. Catal.* **2018**, *1*, 909–921.
- (6) Pomerantseva, E.; Bonaccorso, F.; Feng, X.; Cui, Y.; Gogotsi, Y. Energy Storage: The Future Enabled by Nanomaterials. *Science* **2019**, *366*, eaan8285.
- (7) Sun, Y.; Liu, N.; Cui, Y. Promises and Challenges of Nanomaterials for Lithium-Based Rechargeable Batteries. *Nat. Energy* **2016**, *1*, 16071.
- (8) Li, Y.; Dai, H. Recent Advances in Zinc–Air Batteries. *Chem. Soc. Rev.* **2014**, *43*, 5257–5275.
- (9) Greeley, J.; Stephens, I. E. L.; Bondarenko, A. S.; Johansson, T. P.; Hansen, H. A.; Jaramillo, T. F.; Rossmeisl, J.; Chorkendorff, I.; Nørskov, J. K. Alloys of Platinum and Early Transition Metals as Oxygen Reduction Electrocatalysts. *Nat. Chem.* **2009**, *1*, 552–556.
- (10) Greeley, J.; Jaramillo, T. F.; Bonde, J.; Chorkendorff, I.; Nørskov, J. K. Computational High-Throughput Screening of Electrocatalytic Materials for Hydrogen Evolution. *Nat. Mater.* **2006**, *5*, 909–913.
- (11) Montoya, J. H.; Seitz, L. C.; Chakhranont, P.; Vojvodic, A.; Jaramillo, T. F.; Nørskov, J. K. Materials for Solar Fuels and Chemicals. *Nat. Mater.* **2017**, *16*, 70–81.
- (12) Naguib, M.; Kurtoglu, M.; Presser, V.; Lu, J.; Niu, J.; Heon, M.; Hultman, L.; Gogotsi, Y.; Barsoum, M. W. Two-Dimensional Nanocrystals Produced by Exfoliation of  $\text{Ti}_3\text{AlC}_2$ . *Adv. Mater.* **2011**, *23*, 4248–4253.
- (13) Gogotsi, Y.; Anasori, B. The Rise of MXenes. *ACS Nano* **2019**, *13*, 8491–8494.
- (14) Anasori, B.; Gogotsi, Y. Introduction to 2D Transition Metal Carbides and Nitrides (MXenes). In *2D Metal Carbides and Nitrides (MXenes): Structure, Properties and Applications*; Springer International Publishing: Cham, 2019; pp 3–12.
- (15) Li, Z.; Wu, Y. 2D Early Transition Metal Carbides (MXenes) for Catalysis. *Small* **2019**, *15*, 1804736.
- (16) Naguib, M.; Mochalin, V. N.; Barsoum, M. W.; Gogotsi, Y. 25th Anniversary Article: MXenes: A New Family of Two-Dimensional Materials. *Adv. Mater.* **2014**, *26*, 992–1005.
- (17) Seh, Z. W.; Fredrickson, K. D.; Anasori, B.; Kibsgaard, J.; Strickler, A. L.; Lukatskaya, M. R.; Gogotsi, Y.; Jaramillo, T. F.; Vojvodic, A. Two-Dimensional Molybdenum Carbide (MXene) as an Efficient Electrocatalyst for Hydrogen Evolution. *ACS Energy Lett.* **2016**, *1*, 589–594.

- 1  
2  
3 (18) Handoko, A. D.; Fredrickson, K. D.; Anasori, B.; Convey, K. W.; Johnson, L. R.; Gogotsi,  
4 Y.; Vojvodic, A.; Seh, Z. W. Tuning the Basal Plane Functionalization of Two-  
5 Dimensional Metal Carbides (MXenes) To Control Hydrogen Evolution Activity. *ACS*  
6 *Appl. Energy Mater.* **2018**, *1*, 173–180.
- 7  
8 (19) Djire, A.; Wang, X.; Xiao, C.; Nwamba, O. C.; Mirkin, M. V.; Neale, N. R. Basal Plane  
9 Hydrogen Evolution Activity from Mixed Metal Nitride MXenes Measured by Scanning  
10 Electrochemical Microscopy. *Adv. Funct. Mater.* **2020**, 2001136.
- 11 (20) Jaramillo, T. F.; Jorgensen, K. P.; Bonde, J.; Nielsen, J. H.; Horch, S.; Chorkendorff, I.  
12 Identification of Active Edge Sites for Electrochemical H<sub>2</sub> Evolution from MoS<sub>2</sub>  
13 Nanocatalysts. *Science* **2007**, *317*, 100–102.
- 14 (21) Zhan, C.; Sun, W.; Xie, Y.; Jiang, D.; Kent, P. R. C. Computational Discovery and Design  
15 of MXenes for Energy Applications: Status, Successes, and Opportunities. *ACS Appl.*  
16 *Mater. Interfaces* **2019**, *11*, 24885–24905.
- 17 (22) Chen, H.; Handoko, A. D.; Xiao, J.; Feng, X.; Fan, Y.; Wang, T.; Legut, D.; Seh, Z. W.;  
18 Zhang, Q. Catalytic Effect on CO<sub>2</sub> Electroreduction by Hydroxyl-Terminated Two-  
19 Dimensional MXenes. *ACS Appl. Mater. Interfaces* **2019**, *11*, 36571–36579.
- 20 (23) Handoko, A. D.; Khoo, K. H.; Tan, T. L.; Jin, H.; Seh, Z. W. Establishing New Scaling  
21 Relations on Two-Dimensional MXenes for CO<sub>2</sub> Electroreduction. *J. Mater. Chem. A*  
22 **2018**, *6*, 21885–21890.
- 23 (24) Johnson, L. R.; Sridhar, S.; Zhang, L.; Fredrickson, K. D.; Raman, A. S.; Jang, J.; Leach,  
24 C.; Padmanabhan, A.; Price, C. C.; Frey, N. C.; Raizada, A.; Rajaraman, V.; Saiprasad, S.  
25 A.; Tang, X.; Vojvodic, A. MXene Materials for the Electrochemical Nitrogen  
26 Reduction—Functionalized or Not? *ACS Catal.* **2020**, *10*, 253–264.
- 27 (25) Handoko, A. D.; Chen, H.; Lum, Y.; Zhang, Q.; Anasori, B.; Seh, Z. W. Two-Dimensional  
28 Titanium and Molybdenum Carbide MXenes as Electrocatalysts for CO<sub>2</sub> Reduction.  
29 *iScience* **2020**, *23*, 101181.
- 30 (26) Deysher, G.; Shuck, C. E.; Hantanasirisakul, K.; Frey, N. C.; Foucher, A. C.; Maleski, K.;  
31 Sarycheva, A.; Shenoy, V. B.; Stach, E. A.; Anasori, B.; Gogotsi, Y. Synthesis of  
32 Mo<sub>4</sub>VAIC<sub>4</sub> MAX Phase and Two-Dimensional Mo<sub>4</sub>VC<sub>4</sub> MXene with Five Atomic Layers  
33 of Transition Metals. *ACS Nano* **2020**, *14*, 204–217.
- 34 (27) Naguib, M.; Mashtalir, O.; Carle, J.; Presser, V.; Lu, J.; Hultman, L.; Gogotsi, Y.;  
35 Barsoum, M. W. Two-Dimensional Transition Metal Carbides. *ACS Nano* **2012**, *6*, 1322–  
36 1331.
- 37 (28) Halim, J.; Kota, S.; Lukatskaya, M. R.; Naguib, M.; Zhao, M.-Q.; Moon, E. J.; Pitock, J.;  
38 Nanda, J.; May, S. J.; Gogotsi, Y.; Barsoum, M. W. Synthesis and Characterization of 2D  
39 Molybdenum Carbide (MXene). *Adv. Funct. Mater.* **2016**, *26*, 3118–3127.
- 40 (29) Anasori, B.; Lukatskaya, M. R.; Gogotsi, Y. 2D Metal Carbides and Nitrides (MXenes)  
41 for Energy Storage. *Nat. Rev. Mater.* **2017**, *2*, 16098.
- 42 (30) Srivastava, P.; Mishra, A.; Mizuseki, H.; Lee, K.-R.; Singh, A. K. Mechanistic Insight into  
43 the Chemical Exfoliation and Functionalization of Ti<sub>3</sub>C<sub>2</sub> MXene. *ACS Appl. Mater.*  
44 *Interfaces* **2016**, *8*, 24256–24264.
- 45 (31) Naguib, M.; Gogotsi, Y. Synthesis of Two-Dimensional Materials by Selective Extraction.  
46 *Acc. Chem. Res.* **2015**, *48*, 128–135.
- 47 (32) Shuck, C. E.; Sarycheva, A.; Anayee, M.; Levitt, A.; Zhu, Y.; Uzun, S.; Balitskiy, V.;  
48 Zahorodna, V.; Gogotsi, O.; Gogotsi, Y. Scalable Synthesis of Ti<sub>3</sub>C<sub>2</sub>T<sub>x</sub> MXene. *Adv. Eng.*  
49 *Mater.* **2020**, *22*, 1901241.
- 50  
51  
52  
53  
54  
55  
56  
57  
58  
59  
60

- 1  
2  
3 (33) Verger, L.; Natu, V.; Carey, M.; Barsoum, M. W. MXenes: An Introduction of Their  
4 Synthesis, Select Properties, and Applications. *Trends Chem.* **2019**, *1*, 656–669.
- 5 (34) Alhabeb, M.; Maleski, K.; Anasori, B.; Lelyukh, P.; Clark, L.; Sin, S.; Gogotsi, Y.  
6 Guidelines for Synthesis and Processing of Two-Dimensional Titanium Carbide ( $\text{Ti}_3\text{C}_2\text{T}_x$   
7 MXene). *Chem. Mater.* **2017**, *29*, 7633–7644.
- 8 (35) Halim, J.; Lukatskaya, M. R.; Cook, K. M.; Lu, J.; Smith, C. R.; Näslund, L.-Å.; May, S.  
9 J.; Hultman, L.; Gogotsi, Y.; Eklund, P.; Barsoum, M. W. Transparent Conductive Two-  
10 Dimensional Titanium Carbide Epitaxial Thin Films. *Chem. Mater.* **2014**, *26*, 2374–2381.
- 11 (36) Sun, W.; Shah, S. A.; Chen, Y.; Tan, Z.; Gao, H.; Habib, T.; Radovic, M.; Green, M. J.  
12 Electrochemical Etching of  $\text{Ti}_2\text{AlC}$  to  $\text{Ti}_2\text{CT}_x$  (MXene) in Low-Concentration  
13 Hydrochloric Acid Solution. *J. Mater. Chem. A* **2017**, *5*, 21663–21668.
- 14 (37) Li, P.; Zhu, J.; Handoko, A. D.; Zhang, R.; Wang, H.; Legut, D.; Wen, X.; Fu, Z.; Seh, Z.  
15 W.; Zhang, Q. High-Throughput Theoretical Optimization of the Hydrogen Evolution  
16 Reaction on MXenes by Transition Metal Modification. *J. Mater. Chem. A* **2018**, *6*, 4271–  
17 4278.
- 18 (38) Naguib, M.; Unocic, R. R.; Armstrong, B. L.; Nanda, J. Large-Scale Delamination of  
19 Multi-Layers Transition Metal Carbides and Carbonitrides “MXenes.” *Dalton Trans.*  
20 **2015**, *44*, 9353–9358.
- 21 (39) Mashtalir, O.; Naguib, M.; Mochalin, V. N.; Dall’Agnese, Y.; Heon, M.; Barsoum, M. W.;  
22 Gogotsi, Y. Intercalation and Delamination of Layered Carbides and Carbonitrides. *Nat.*  
23 *Commun.* **2013**, *4*, 1716.
- 24 (40) Fu, Z.; Wang, N.; Legut, D.; Si, C.; Zhang, Q.; Du, S.; Germann, T. C.; Francisco, J. S.;  
25 Zhang, R. Rational Design of Flexible Two-Dimensional MXenes with Multiple  
26 Functionalities. *Chem. Rev.* **2019**, *119*, 11980–12031.
- 27 (41) Liu, Y.-T.; Zhu, X.-D.; Pan, L. Hybrid Architectures Based on 2D MXenes and Low-  
28 Dimensional Inorganic Nanostructures: Methods, Synergies, and Energy-Related  
29 Applications. *Small* **2018**, *14*, 1803632.
- 30 (42) Zhan, X.; Si, C.; Zhou, J.; Sun, Z. MXene and MXene-Based Composites: Synthesis,  
31 Properties and Environment-Related Applications. *Nanoscale Horiz.* **2020**, *5*, 235–258.
- 32 (43) Yu, H.; Wang, Y.; Jing, Y.; Ma, J.; Du, C.; Yan, Q. Surface Modified MXene-Based  
33 Nanocomposites for Electrochemical Energy Conversion and Storage. *Small* **2019**, *15*,  
34 1901503.
- 35 (44) Peng, J.; Chen, X.; Ong, W.-J.; Zhao, X.; Li, N. Surface and Heterointerface Engineering  
36 of 2D MXenes and Their Nanocomposites: Insights into Electro- and Photocatalysis. *Chem*  
37 **2019**, *5*, 18–50.
- 38 (45) Wang, H.; Lee, J.-M. Recent Advances in Structural Engineering of MXene  
39 Electrocatalysts. *J. Mater. Chem. A* **2020**, *8*, 10604–10624.
- 40 (46) Zheng, L.; Han, S.; Liu, H.; Yu, P.; Fang, X. Hierarchical  $\text{MoS}_2$  Nanosheet@ $\text{TiO}_2$   
41 Nanotube Array Composites with Enhanced Photocatalytic and Photocurrent  
42 Performances. *Small* **2016**, *12*, 1527–1536.
- 43 (47) Peng, C.; Yang, X.; Li, Y.; Yu, H.; Wang, H.; Peng, F. Hybrids of Two-Dimensional  $\text{Ti}_3\text{C}_2$   
44 and  $\text{TiO}_2$  Exposing {001} Facets toward Enhanced Photocatalytic Activity. *ACS Appl.*  
45 *Mater. Interfaces* **2016**, *8*, 6051–6060.
- 46 (48) Wang, H.; Wu, Y.; Xiao, T.; Yuan, X.; Zeng, G.; Tu, W.; Wu, S.; Lee, H. Y.; Tan, Y. Z.;  
47 Chew, J. W. Formation of Quasi-Core-Shell  $\text{In}_2\text{S}_3/\text{Anatase TiO}_2$ @metallic  $\text{Ti}_3\text{C}_2\text{T}_x$   
48  
49  
50  
51  
52  
53  
54  
55  
56  
57  
58  
59  
60

- Hybrids with Favorable Charge Transfer Channels for Excellent Visible-Light-Photocatalytic Performance. *Appl. Catal. B: Environ.* **2018**, *233*, 213–225.
- (49) Kong, F.; He, X.; Liu, Q.; Qi, X.; Sun, D.; Zheng, Y.; Wang, R.; Bai, Y. Further Surface Modification by Carbon Coating for *In-Situ* Growth of Fe<sub>3</sub>O<sub>4</sub> Nanoparticles on MXene Ti<sub>3</sub>C<sub>2</sub> Multilayers for Advanced Li-Ion Storage. *Electrochim. Acta* **2018**, *289*, 228–237.
- (50) Zuo, D.; Song, S.; An, C.; Tang, L.; He, Z.; Zheng, J. Synthesis of Sandwich-like Structured Sn/SnO<sub>x</sub>@MXene Composite through *In-Situ* Growth for Highly Reversible Lithium Storage. *Nano Energy* **2019**, *62*, 401–409.
- (51) Sun, X.; Tan, K.; Liu, Y.; Zhang, J.; Denis, D. K.; Zaman, F. uz; Hou, L.; Yuan, C. A Two-Dimensional Assembly of Ultrafine Cobalt Oxide Nanocrystallites Anchored on Single-Layer Ti<sub>3</sub>C<sub>2</sub>T<sub>x</sub> Nanosheets with Enhanced Lithium Storage for Li-Ion Batteries. *Nanoscale* **2019**, *11*, 16755–16766.
- (52) Li, Z.; Qi, Z.; Wang, S.; Ma, T.; Zhou, L.; Wu, Z.; Luan, X.; Lin, F.-Y.; Chen, M.; Miller, J. T.; Xin, H.; Huang, W.; Wu, Y. *In Situ* Formed Pt<sub>3</sub>Ti Nanoparticles on a Two-Dimensional Transition Metal Carbide (MXene) Used as Efficient Catalysts for Hydrogen Evolution Reactions. *Nano Lett.* **2019**, *19*, 5102–5108.
- (53) Zhu, X.-D.; Xie, Y.; Liu, Y.-T. Exploring the Synergy of 2D MXene-Supported Black Phosphorus Quantum Dots in Hydrogen and Oxygen Evolution Reactions. *J. Mater. Chem. A* **2018**, *6*, 21255–21260.
- (54) Xu, J.; Shim, J.; Park, J.-H.; Lee, S. MXene Electrode for the Integration of WSe<sub>2</sub> and MoS<sub>2</sub> Field Effect Transistors. *Adv. Funct. Mater.* **2016**, *26*, 5328–5334.
- (55) Naguib, M.; Mashtalir, O.; Lukatskaya, M. R.; Dyatkin, B.; Zhang, C.; Presser, V.; Gogotsi, Y.; Barsoum, M. W. One-Step Synthesis of Nanocrystalline Transition Metal Oxides on Thin Sheets of Disordered Graphitic Carbon by Oxidation of MXenes. *Chem. Commun.* **2014**, *50*, 7420–7423.
- (56) Liang, X.; Rangom, Y.; Kwok, C. Y.; Pang, Q.; Nazar, L. F. Interwoven MXene Nanosheet/Carbon-Nanotube Composites as Li-S Cathode Hosts. *Adv. Mater.* **2017**, *29*, 1603040.
- (57) Venkatkarthick, R.; Rodthongkum, N.; Zhang, X.; Wang, S.; Pattananuwat, P.; Zhao, Y.; Liu, R.; Qin, J. Vanadium-Based Oxide on Two-Dimensional Vanadium Carbide MXene (V<sub>2</sub>O<sub>x</sub>@V<sub>2</sub>CT<sub>x</sub>) as Cathode for Rechargeable Aqueous Zinc-Ion Batteries. *ACS Appl. Energy Mater.* **2020**, *3*, 4677–4689.
- (58) Wang, Z.; Yu, K.; Feng, Y.; Qi, R.; Ren, J.; Zhu, Z. VO<sub>2</sub>(p)-V<sub>2</sub>C(MXene) Grid Structure as a Lithium Polysulfide Catalytic Host for High-Performance Li–S Battery. *ACS Appl. Mater. Interfaces* **2019**, *11*, 44282–44292.
- (59) Bai, J.; Zhao, B.; Lin, S.; Li, K.; Zhou, J.; Dai, J.; Zhu, X.; Sun, Y. Construction of Hierarchical V<sub>4</sub>C<sub>3</sub>-MXene/MoS<sub>2</sub>/C Nanohybrids for High Rate Lithium-Ion Batteries. *Nanoscale* **2020**, *12*, 1144–1154.
- (60) Wang, X.; Li, H.; Li, H.; Lin, S.; Bai, J.; Dai, J.; Liang, C.; Zhu, X.; Sun, Y.; Dou, S. Heterostructures of Ni–Co–Al Layered Double Hydroxide Assembled on V<sub>4</sub>C<sub>3</sub> MXene for High-Energy Hybrid Supercapacitors. *J. Mater. Chem. A* **2019**, *7*, 2291–2300.
- (61) Butt, R.; Siddique, A. H.; Bokhari, S. W.; Jiang, S.; Lei, D.; Zhou, X.; Liu, Z. Niobium Carbide/Reduced Graphene Oxide Hybrid Porous Aerogel as High Capacity and Long-life Anode Material for Li-ion Batteries. *Int. J. Energy Res.* **2019**, *43*, 4995–5003.

- 1  
2  
3 (62) Zhang, C. J.; Kim, S. J.; Ghidui, M.; Zhao, M.-Q.; Barsoum, M. W.; Nicolosi, V.; Gogotsi,  
4 Y. Layered Orthorhombic Nb<sub>2</sub>O<sub>5</sub>@Nb<sub>4</sub>C<sub>3</sub>T<sub>x</sub> and TiO<sub>2</sub>@Ti<sub>3</sub>C<sub>2</sub>T<sub>x</sub> Hierarchical Composites  
5 for High Performance Li-Ion Batteries. *Adv. Funct. Mater.* **2016**, *26*, 4143–4151.
- 6 (63) Qin, L.; Tao, Q.; El Ghazaly, A.; Fernandez-Rodriguez, J.; Persson, P. O. Å.; Rosen, J.;  
7 Zhang, F. High-Performance Ultrathin Flexible Solid-State Supercapacitors Based on  
8 Solution Processable Mo<sub>1.33</sub>C MXene and PEDOT:PSS. *Adv. Funct. Mater.* **2018**, *28*,  
9 1703808.
- 10 (64) Lv, L.; Guo, C.; Sun, W.; Wang, Y. Strong Surface-Bound Sulfur in Carbon Nanotube  
11 Bridged Hierarchical Mo<sub>2</sub>C-Based MXene Nanosheets for Lithium–Sulfur Batteries.  
12 *Small* **2018**, 1804338.
- 13 (65) Jeon, J.; Park, Y.; Choi, S.; Lee, J.; Lim, S. S.; Lee, B. H.; Song, Y. J.; Cho, J. H.; Jang, Y.  
14 H.; Lee, S. Epitaxial Synthesis of Molybdenum Carbide and Formation of a Mo<sub>2</sub>C/MoS<sub>2</sub>  
15 Hybrid Structure *via* Chemical Conversion of Molybdenum Disulfide. *ACS Nano* **2018**,  
16 *12*, 338–346.
- 17 (66) Sun, W.; Wang, X.; Feng, J.; Li, T.; Huan, Y.; Qiao, J.; He, L.; Ma, D. Controlled Synthesis  
18 of 2D Mo<sub>2</sub>C/Graphene Heterostructure on Liquid Au Substrates as Enhanced  
19 Electrocatalytic Electrodes. *Nanotechnology* **2019**, *30*, 385601.
- 20 (67) Chen, C.; Xie, X.; Anasori, B.; Sarycheva, A.; Makaryan, T.; Zhao, M.; Urbankowski, P.;  
21 Miao, L.; Jiang, J.; Gogotsi, Y. MoS<sub>2</sub>-on-MXene Heterostructures as Highly Reversible  
22 Anode Materials for Lithium-Ion Batteries. *Angew. Chem. Int. Ed.* **2018**, *57*, 1846–1850.
- 23 (68) Dai, C.; Chen, Y.; Jing, X.; Xiang, L.; Yang, D.; Lin, H.; Liu, Z.; Han, X.; Wu, R. Two-  
24 Dimensional Tantalum Carbide (MXenes) Composite Nanosheets for Multiple Imaging-  
25 Guided Photothermal Tumor Ablation. *ACS Nano* **2017**, *11*, 12696–12712.
- 26 (69) Zhang, J.; Kong, N.; Uzun, S.; Levitt, A.; Seyedin, S.; Lynch, P. A.; Qin, S.; Han, M.;  
27 Yang, W.; Liu, J.; Wang, X.; Gogotsi, Y.; Razal, J. M. Scalable Manufacturing of  
28 Free-Standing, Strong Ti<sub>3</sub>C<sub>2</sub>T<sub>x</sub> MXene Films with Outstanding Conductivity. *Adv. Mater.*  
29 **2020**, *32*, 2001093.
- 30 (70) Wu, X.; Wang, Z.; Yu, M.; Xiu, L.; Qiu, J. Stabilizing the MXenes by Carbon Nanoplate  
31 for Developing Hierarchical Nanohybrids with Efficient Lithium Storage and Hydrogen  
32 Evolution Capability. *Adv. Mater.* **2017**, *29*, 1607017.
- 33 (71) Gao, Y.; Wang, L.; Zhou, A.; Li, Z.; Chen, J.; Bala, H.; Hu, Q.; Cao, X. Hydrothermal  
34 Synthesis of TiO<sub>2</sub>/Ti<sub>3</sub>C<sub>2</sub> Nanocomposites with Enhanced Photocatalytic Activity. *Mater.*  
35 *Lett.* **2015**, *150*, 62–64.
- 36 (72) Zhang, H.; Dong, H.; Zhang, X.; Xu, Y.; Fransaer, J. Cu<sub>2</sub>O Hybridized Titanium Carbide  
37 with Open Conductive Frameworks for Lithium-Ion Batteries. *Electrochim. Acta* **2016**,  
38 *202*, 24–31.
- 39 (73) Rakhi, R. B.; Ahmed, B.; Anjum, D.; Alshareef, H. N. Direct Chemical Synthesis of MnO<sub>2</sub>  
40 Nanowhiskers on Transition-Metal Carbide Surfaces for Supercapacitor Applications.  
41 *ACS Appl. Mater. Interfaces* **2016**, *8*, 18806–18814.
- 42 (74) Du, Y.; Zhang, X.; Wei, L.; Yu, B.; Wang, Y.; Wang, Y.; Ye, S. Electrodeposition of a Ni-  
43 P Composite Coating Reinforced with Ti<sub>3</sub>C<sub>2</sub>T<sub>x</sub>@TiO<sub>2</sub>/MoS<sub>2</sub> Particles. *Mater. Chem. Phys.*  
44 **2020**, *241*, 122448.
- 45 (75) Mai, Y. J.; Li, Y. G.; Li, S. L.; Zhang, L. Y.; Liu, C. S.; Jie, X. H. Self-Lubricating Ti<sub>3</sub>C<sub>2</sub>  
46 Nanosheets/Copper Composite Coatings. *J. Alloys Compd.* **2019**, *770*, 1–5.
- 47  
48  
49  
50  
51  
52  
53  
54  
55  
56  
57  
58  
59  
60



- 1  
2  
3 (76) Yang, Q.; Huang, Z.; Li, X.; Liu, Z.; Li, H.; Liang, G.; Wang, D.; Huang, Q.; Zhang, S.;  
4 Chen, S.; Zhi, C. A Wholly Degradable, Rechargeable Zn–Ti<sub>3</sub>C<sub>2</sub> MXene Capacitor with  
5 Superior Anti-Self-Discharge Function. *ACS Nano* **2019**, *13*, 8275–8283.
- 6 (77) Aïssa, B.; Ali, A.; Mahmoud, K. A.; Haddad, T.; Nedil, M. Transport Properties of a  
7 Highly Conductive 2D Ti<sub>3</sub>C<sub>2</sub>T<sub>x</sub> MXene/Graphene Composite. *Appl. Phys. Lett.* **2016**, *109*,  
8 043109.
- 9 (78) Peng, C.; Wei, P.; Li, X.; Liu, Y.; Cao, Y.; Wang, H.; Yu, H.; Peng, F.; Zhang, L.; Zhang,  
10 B.; Lv, K. High Efficiency Photocatalytic Hydrogen Production over Ternary  
11 Cu/TiO<sub>2</sub>@Ti<sub>3</sub>C<sub>2</sub>T<sub>x</sub> Enabled by Low-Work-Function 2D Titanium Carbide. *Nano Energy*  
12 **2018**, *53*, 97–107.
- 13 (79) Ahmed, B.; Anjum, D. H.; Gogotsi, Y.; Alshareef, H. N. Atomic Layer Deposition of SnO<sub>2</sub>  
14 on MXene for Li-Ion Battery Anodes. *Nano Energy* **2017**, *34*, 249–256.
- 15 (80) Yu, X.; Wang, T.; Yin, W.; Zhang, Y. Ti<sub>3</sub>C<sub>2</sub> MXene Nanoparticles Modified Metal Oxide  
16 Composites for Enhanced Photoelectrochemical Water Splitting. *Int. J. Hydrog. Energy*  
17 **2019**, *44*, 2704–2710.
- 18 (81) Karlsson, L. H.; Birch, J.; Halim, J.; Barsoum, M. W.; Persson, P. O. Å. Atomically  
19 Resolved Structural and Chemical Investigation of Single MXene Sheets. *Nano Lett.* **2015**,  
20 *15*, 4955–4960.
- 21 (82) Byeon, A.; Hatter, C. B.; Park, J. H.; Ahn, C. W.; Gogotsi, Y.; Lee, J. W. Molybdenum  
22 Oxide/Carbon Composites Derived from the CO<sub>2</sub> Oxidation of Mo<sub>2</sub>CT<sub>x</sub> (MXene) for  
23 Lithium Ion Battery Anodes. *Electrochim. Acta* **2017**, *258*, 979–987.
- 24 (83) Yuan, W.; Cheng, L.; Zhang, Y.; Wu, H.; Lv, S.; Chai, L.; Guo, X.; Zheng, L. 2D-Layered  
25 Carbon/TiO<sub>2</sub> Hybrids Derived from Ti<sub>3</sub>C<sub>2</sub> MXenes for Photocatalytic Hydrogen Evolution  
26 under Visible Light Irradiation. *Adv. Mater. Interfaces* **2017**, *4*, 1700577.
- 27 (84) Yazdanparast, S.; Soltanmohammad, S.; Fash-White, A.; Tucker, G. J.; Brennecka, G. L.  
28 Synthesis and Surface Chemistry of 2D TiVC Solid-Solution MXenes. *ACS Appl. Mater.*  
29 *Interfaces* **2020**, *12*, 20129–20137.
- 30 (85) Low, J.; Zhang, L.; Tong, T.; Shen, B.; Yu, J. TiO<sub>2</sub>/MXene Ti<sub>3</sub>C<sub>2</sub> Composite with  
31 Excellent Photocatalytic CO<sub>2</sub> Reduction Activity. *J. Catal.* **2018**, *361*, 255–266.
- 32 (86) Hou, T.; Li, Q.; Zhang, Y.; Zhu, W.; Yu, K.; Wang, S.; Xu, Q.; Liang, S.; Wang, L. Near-  
33 Infrared Light-Driven Photofixation of Nitrogen over Ti<sub>3</sub>C<sub>2</sub>T<sub>x</sub>/TiO<sub>2</sub> Hybrid Structures with  
34 Superior Activity and Stability. *Appl. Catal. B: Environ.* **2020**, *273*, 119072.
- 35 (87) Li, Y.; Zhang, D.; Feng, X.; Liao, Y.; Wen, Q.; Xiang, Q. Truncated Octahedral  
36 Bipyramidal TiO<sub>2</sub>/MXene Ti<sub>3</sub>C<sub>2</sub> Hybrids with Enhanced Photocatalytic H<sub>2</sub> Production  
37 Activity. *Nanoscale Adv.* **2019**, *1*, 1812–1818.
- 38 (88) Hao, C.; Liao, Y.; Wu, Y.; An, Y.; Lin, J.; Gu, Z.; Jiang, M.; Hu, S.; Wang, X. RuO<sub>2</sub>-  
39 Loaded TiO<sub>2</sub>-MXene as a High Performance Photocatalyst for Nitrogen Fixation. *J. Phys.*  
40 *Chem. Solids* **2020**, *136*, 109141.
- 41 (89) Li, Y.; Deng, X.; Tian, J.; Liang, Z.; Cui, H. Ti<sub>3</sub>C<sub>2</sub> MXene-Derived Ti<sub>3</sub>C<sub>2</sub>/TiO<sub>2</sub>  
42 Nanoflowers for Noble-Metal-Free Photocatalytic Overall Water Splitting. *Appl. Mater.*  
43 *Today* **2018**, *13*, 217–227.
- 44 (90) Zheng, R.; Shu, C.; Hou, Z.; Hu, A.; Hei, P.; Yang, T.; Li, J.; Liang, R.; Long, J. *In Situ*  
45 Fabricating Oxygen Vacancy-Rich TiO<sub>2</sub> Nanoparticles *via* Utilizing Thermodynamically  
46 Metastable Ti Atoms on Ti<sub>3</sub>C<sub>2</sub>T<sub>x</sub> MXene Nanosheet Surface To Boost Electrocatalytic  
47 Activity for High-Performance Li–O<sub>2</sub> Batteries. *ACS Appl. Mater. Interfaces* **2019**, *11*,  
48 46696–46704.
- 49  
50  
51  
52  
53  
54  
55  
56  
57  
58  
59  
60

- 1  
2  
3 (91) Fang, Y.; Liu, Z.; Han, J.; Jin, Z.; Han, Y.; Wang, F.; Niu, Y.; Wu, Y.; Xu, Y. High-Performance Electrocatalytic Conversion of N<sub>2</sub> to NH<sub>3</sub> Using Oxygen-Vacancy-Rich TiO<sub>2</sub> *In Situ* Grown on Ti<sub>3</sub>C<sub>2</sub>T<sub>x</sub> MXene. *Adv. Energy Mater.* **2019**, *9*, 1803406.
- 4  
5  
6 (92) Xu, Y.; Wang, S.; Yang, J.; Han, B.; Nie, R.; Wang, J.; Wang, J.; Jing, H. *In-Situ* Grown Nanocrystal TiO<sub>2</sub> on 2D Ti<sub>3</sub>C<sub>2</sub> Nanosheets for Artificial Photosynthesis of Chemical Fuels. *Nano Energy* **2018**, *51*, 442–450.
- 7  
8  
9 (93) Peng, C.; Wang, H.; Yu, H.; Peng, F. (111) TiO<sub>2-x</sub>/Ti<sub>3</sub>C<sub>2</sub>: Synergy of Active Facets, Interfacial Charge Transfer and Ti<sup>3+</sup> Doping for Enhance Photocatalytic Activity. *Mater. Res. Bull.* **2017**, *89*, 16–25.
- 10  
11  
12 (94) Lotfi, R.; Naguib, M.; Yilmaz, D. E.; Nanda, J.; van Duin, A. C. T. A Comparative Study on the Oxidation of Two-Dimensional Ti<sub>3</sub>C<sub>2</sub> MXene Structures in Different Environments. *J. Mater. Chem. A* **2018**, *6*, 12733–12743.
- 13  
14  
15 (95) Chertopalov, S.; Mochalin, V. N. Environment-Sensitive Photoresponse of Spontaneously Partially Oxidized Ti<sub>3</sub>C<sub>2</sub> MXene Thin Films. *ACS Nano* **2018**, *12*, 6109–6116.
- 16  
17  
18 (96) Ghassemi, H.; Harlow, W.; Mashtalir, O.; Beidaghi, M.; Lukatskaya, M. R.; Gogotsi, Y.; Taheri, M. L. *In Situ* Environmental Transmission Electron Microscopy Study of Oxidation of Two-Dimensional Ti<sub>3</sub>C<sub>2</sub> and Formation of Carbon-Supported TiO<sub>2</sub>. *J. Mater. Chem. A* **2014**, *2*, 14339.
- 19  
20  
21 (97) Yuan, W.; Cheng, L.; An, Y.; Lv, S.; Wu, H.; Fan, X.; Zhang, Y.; Guo, X.; Tang, J. Laminated Hybrid Junction of Sulfur-Doped TiO<sub>2</sub> and a Carbon Substrate Derived from Ti<sub>3</sub>C<sub>2</sub> MXenes: Toward Highly Visible Light-Driven Photocatalytic Hydrogen Evolution. *Adv. Sci.* **2018**, *5*, 1700870.
- 22  
23  
24 (98) Anasori, B.; Xie, Y.; Beidaghi, M.; Lu, J.; Hosler, B. C.; Hultman, L.; Kent, P. R. C.; Gogotsi, Y.; Barsoum, M. W. Two-Dimensional, Ordered, Double Transition Metals Carbides (MXenes). *ACS Nano* **2015**, *9*, 9507–9516.
- 25  
26  
27 (99) Anasori, B.; Shi, C.; Moon, E. J.; Xie, Y.; Voigt, C. A.; Kent, P. R. C.; May, S. J.; Billinge, S. J. L.; Barsoum, M. W.; Gogotsi, Y. Control of Electronic Properties of 2D Carbides (MXenes) by Manipulating Their Transition Metal Layers. *Nanoscale Horiz.* **2016**, *1*, 227–234.
- 28  
29  
30 (100) Kong, X.; Gao, P.; Jiang, R.; Feng, J.; Yang, P.; Gai, S.; Chen, Y.; Chi, Q.; Xu, F.; Ye, W. Orderly Layer-by-Layered TiO<sub>2</sub>/Carbon Superstructures Based on MXene's Defect Engineering for Efficient Hydrogen Evolution. *Appl. Catal. A: General* **2020**, *590*, 117341.
- 31  
32  
33 (101) Cao, S.; Shen, B.; Tong, T.; Fu, J.; Yu, J. 2D/2D Heterojunction of Ultrathin MXene/Bi<sub>2</sub>WO<sub>6</sub> Nanosheets for Improved Photocatalytic CO<sub>2</sub> Reduction. *Adv. Funct. Mater.* **2018**, *28*, 1800136.
- 34  
35  
36 (102) Li, N.; Zhang, Y.; Jia, M.; Lv, X.; Li, X.; Li, R.; Ding, X.; Zheng, Y.-Z.; Tao, X. 1T/2H MoSe<sub>2</sub>-on-MXene Heterostructure as Bifunctional Electrocatalyst for Efficient Overall Water Splitting. *Electrochim. Acta* **2019**, *326*, 134976.
- 37  
38  
39 (103) Zhao, M.-Q.; Torelli, M.; Ren, C. E.; Ghidui, M.; Ling, Z.; Anasori, B.; Barsoum, M. W.; Gogotsi, Y. 2D Titanium Carbide and Transition Metal Oxides Hybrid Electrodes for Li-Ion Storage. *Nano Energy* **2016**, *30*, 603–613.
- 40  
41  
42 (104) Xiong, J.; Pan, L.; Wang, H.; Du, F.; Chen, Y.; Yang, J.; Zhang, C. (John). Synergistically Enhanced Lithium Storage Performance Based on Titanium Carbide Nanosheets (MXene) Backbone and SnO<sub>2</sub> Quantum Dots. *Electrochim. Acta* **2018**, *268*, 503–511.
- 43  
44  
45  
46  
47  
48  
49  
50  
51  
52  
53  
54  
55  
56  
57  
58  
59  
60

- 1  
2  
3 (105) Gao, X.-T.; Xie, Y.; Zhu, X.-D.; Sun, K.-N.; Xie, X.-M.; Liu, Y.-T.; Yu, J.-Y.; Ding, B.  
4 Ultrathin MXene Nanosheets Decorated with TiO<sub>2</sub> Quantum Dots as an Efficient Sulfur  
5 Host toward Fast and Stable Li-S Batteries. *Small* **2018**, *14*, 1802443.
- 6 (106) Li, X.; Yin, X.; Xu, H.; Han, M.; Li, M.; Liang, S.; Cheng, L.; Zhang, L. Ultralight MXene-  
7 Coated, Interconnected SiC<sub>n</sub>s Three-Dimensional Lamellar Foams for Efficient  
8 Microwave Absorption in the X-Band. *ACS Appl. Mater. Interfaces* **2018**, *10*, 34524–  
9 34533.
- 10 (107) Zhao, L.; Dong, B.; Li, S.; Zhou, L.; Lai, L.; Wang, Z.; Zhao, S.; Han, M.; Gao, K.; Lu,  
11 M.; Xie, X.; Chen, B.; Liu, Z.; Wang, X.; Zhang, H.; Li, H.; Liu, J.; Zhang, H.; Huang, X.;  
12 Huang, W. Interdiffusion Reaction-Assisted Hybridization of Two-Dimensional Metal–  
13 Organic Frameworks and Ti<sub>3</sub>C<sub>2</sub>T<sub>x</sub> Nanosheets for Electrocatalytic Oxygen Evolution. *ACS*  
14 *Nano* **2017**, *11*, 5800–5807.
- 15 (108) Byrappa, K.; Yoshimura, M. *Handbook of Hydrothermal Technology*, 2nd ed.; William  
16 Andrew: Oxford ; Waltham, Mass, 2013.
- 17 (109) Zhao, R.; Wang, M.; Zhao, D.; Li, H.; Wang, C.; Yin, L. Molecular-Level Heterostructures  
18 Assembled from Titanium Carbide MXene and Ni–Co–Al Layered Double-Hydroxide  
19 Nanosheets for All-Solid-State Flexible Asymmetric High-Energy Supercapacitors. *ACS*  
20 *Energy Lett.* **2018**, *3*, 132–140.
- 21 (110) Li, H.; Musharavati, F.; Zalenezhad, E.; Chen, X.; Hui, K. N.; Hui, K. S. Electrodeposited  
22 Ni Co Layered Double Hydroxides on Titanium Carbide as a Binder-Free Electrode for  
23 Supercapacitors. *Electrochim. Acta* **2018**, *261*, 178–187.
- 24 (111) Huang, H.; Cui, J.; Liu, G.; Bi, R.; Zhang, L. Carbon-Coated MoSe<sub>2</sub>/MXene Hybrid  
25 Nanosheets for Superior Potassium Storage. *ACS Nano* **2019**, *13*, 3448–3456.
- 26 (112) Handoko, A. D.; Goh, G. K. L. Hydrothermal Synthesis of Sodium Potassium Niobate  
27 Solid Solutions at 200°C. *Green Chem.* **2010**, *12*, 680.
- 28 (113) Gogotsi, Y. G.; Kofstad, P.; Yoshimura, M.; Nickel, K. G. Formation of Sp<sup>3</sup>-Bonded  
29 Carbon upon Hydrothermal Treatment of SiC. *Diam. Relat. Mater.* **1996**, *5*, 151–162.
- 30 (114) Lange, F. F. Chemical Solution Routes to Single-Crystal Thin Films. *Science* **1996**, *273*,  
31 903–909.
- 32 (115) Handoko, A. D.; Goh, G. K. L. Hydrothermal Growth of Piezoelectrically Active Lead-  
33 Free (Na,K)NbO<sub>3</sub>–LiTaO<sub>3</sub> Thin Films. *CrystEngComm* **2013**, *15*, 672–678.
- 34 (116) Demazeau, G. Solvothermal Reactions: An Original Route for the Synthesis of Novel  
35 Materials. *J. Mater. Sci.* **2008**, *43*, 2104–2114.
- 36 (117) Zhu, L.; Lv, J.; Yu, X.; Zhao, H.; Sun, C.; Zhou, Z.; Ying, Y.; Tan, L. Further Construction  
37 of MnO<sub>2</sub> Composite through *In-Situ* Growth on MXene Surface Modified by Carbon  
38 Coating with Outstanding Catalytic Properties on Thermal Decomposition of Ammonium  
39 Perchlorate. *Appl. Surf. Sci.* **2020**, *502*, 144171.
- 40 (118) Liang, J.; Ding, C.; Liu, J.; Chen, T.; Peng, W.; Li, Y.; Zhang, F.; Fan, X. Heterostructure  
41 Engineering of Co-Doped MoS<sub>2</sub> Coupled with Mo<sub>2</sub>CT<sub>x</sub> MXene for Enhanced Hydrogen  
42 Evolution in Alkaline Media. *Nanoscale* **2019**, *11*, 10992–11000.
- 43 (119) Cui, B.; Hu, B.; Liu, J.; Wang, M.; Song, Y.; Tian, K.; Zhang, Z.; He, L. Solution-Plasma-  
44 Assisted Bimetallic Oxide Alloy Nanoparticles of Pt and Pd Embedded within Two-  
45 Dimensional Ti<sub>3</sub>C<sub>2</sub>T<sub>x</sub> Nanosheets as Highly Active Electrocatalysts for Overall Water  
46 Splitting. *ACS Appl. Mater. Interfaces* **2018**, *10*, 23858–23873.
- 47  
48  
49  
50  
51  
52  
53  
54  
55  
56  
57  
58  
59  
60

- 1  
2  
3  
4  
5  
6  
7  
8  
9  
10  
11  
12  
13  
14  
15  
16  
17  
18  
19  
20  
21  
22  
23  
24  
25  
26  
27  
28  
29  
30  
31  
32  
33  
34  
35  
36  
37  
38  
39  
40  
41  
42  
43  
44  
45  
46  
47  
48  
49  
50  
51  
52  
53  
54  
55  
56  
57  
58  
59  
60
- (120) Zou, H.; He, B.; Kuang, P.; Yu, J.; Fan, K. Metal–Organic Framework-Derived Nickel–Cobalt Sulfide on Ultrathin MXene Nanosheets for Electrocatalytic Oxygen Evolution. *ACS Appl. Mater. Interfaces* **2018**, *10*, 22311–22319.
- (121) Zeng, Z.; Yan, Y.; Chen, J.; Zan, P.; Tian, Q.; Chen, P. Boosting the Photocatalytic Ability of Cu<sub>2</sub>O Nanowires for CO<sub>2</sub> Conversion by MXene Quantum Dots. *Adv. Funct. Mater.* **2019**, *29*, 1806500.
- (122) Cai, T.; Wang, L.; Liu, Y.; Zhang, S.; Dong, W.; Chen, H.; Yi, X.; Yuan, J.; Xia, X.; Liu, C.; Luo, S. Ag<sub>3</sub>PO<sub>4</sub>/Ti<sub>3</sub>C<sub>2</sub> MXene Interface Materials as a Schottky Catalyst with Enhanced Photocatalytic Activities and Anti-Photocorrosion Performance. *Appl. Catal. B: Environ.* **2018**, *239*, 545–554.
- (123) Li, Z.; Zhuang, Z.; Lv, F.; Zhu, H.; Zhou, L.; Luo, M.; Zhu, J.; Lang, Z.; Feng, S.; Chen, W.; Mai, L.; Guo, S. The Marriage of the FeN<sub>4</sub> Moiety and MXene Boosts Oxygen Reduction Catalysis: Fe 3d Electron Delocalization Matters. *Adv. Mater.* **2018**, *30*, 1803220.
- (124) Zhao, J.-H.; Liu, L.-W.; Li, K.; Li, T.; Liu, F.-T. Conductive Ti<sub>3</sub>C<sub>2</sub> and MOF-Derived CoS<sub>x</sub> Boosting the Photocatalytic Hydrogen Production Activity of TiO<sub>2</sub>. *CrystEngComm* **2019**, *21*, 2416–2421.
- (125) Pan, A.; Ma, X.; Huang, S.; Wu, Y.; Jia, M.; Shi, Y.; Liu, Y.; Wangyang, P.; He, L.; Liu, Y. CsPbBr<sub>3</sub> Perovskite Nanocrystal Grown on MXene Nanosheets for Enhanced Photoelectric Detection and Photocatalytic CO<sub>2</sub> Reduction. *J. Phys. Chem. Lett.* **2019**, *10*, 6590–6597.
- (126) Yu, M.; Zhou, S.; Wang, Z.; Zhao, J.; Qiu, J. Boosting Electrocatalytic Oxygen Evolution by Synergistically Coupling Layered Double Hydroxide with MXene. *Nano Energy* **2018**, *44*, 181–190.
- (127) Zhang, X.; Shao, B.; Sun, Z.; Gao, Z.; Qin, Y.; Zhang, C.; Cui, F.; Yang, X. Platinum Nanoparticle-Deposited Ti<sub>3</sub>C<sub>2</sub>T<sub>x</sub> MXene for Hydrogen Evolution Reaction. *Ind. Eng. Chem. Res.* **2020**, *59*, 1822–1828.
- (128) Li, X.; Yin, X.; Han, M.; Song, C.; Xu, H.; Hou, Z.; Zhang, L.; Cheng, L. Ti<sub>3</sub>C<sub>2</sub> MXenes Modified with *In Situ* Grown Carbon Nanotubes for Enhanced Electromagnetic Wave Absorption Properties. *J. Mater. Chem. C* **2017**, *5*, 4068–4074.
- (129) Zhang, S.; Ying, H.; Guo, R.; Yang, W.; Han, W.-Q. Vapor Deposition Red Phosphorus to Prepare Nitrogen-Doped Ti<sub>3</sub>C<sub>2</sub>T<sub>x</sub> MXenes Composites for Lithium-Ion Batteries. *J. Phys. Chem. Lett.* **2019**, *10*, 6446–6454.
- (130) Geng, D.; Zhao, X.; Chen, Z.; Sun, W.; Fu, W.; Chen, J.; Liu, W.; Zhou, W.; Loh, K. P. Direct Synthesis of Large-Area 2D Mo<sub>2</sub>C on *In Situ* Grown Graphene. *Adv. Mater.* **2017**, *29*, 1700072.
- (131) Tang, Y.; Yang, C.; Yang, Y.; Yin, X.; Que, W.; Zhu, J. Three Dimensional Hierarchical Network Structure of S-NiFe<sub>2</sub>O<sub>4</sub> Modified Few-Layer Titanium Carbides (MXene) Flakes on Nickel Foam as a High Efficient Electrocatalyst for Oxygen Evolution. *Electrochim. Acta* **2019**, *296*, 762–770.
- (132) Yang, L.; Zheng, W.; Zhang, P.; Chen, J.; Tian, W. B.; Zhang, Y. M.; Sun, Z. M. MXene/CNTs Films Prepared by Electrophoretic Deposition for Supercapacitor Electrodes. *J. Electroanal. Chem.* **2018**, *830–831*, 1–6.
- (133) An, X.; Wang, W.; Wang, J.; Duan, H.; Shi, J.; Yu, X. The Synergetic Effects of Ti<sub>3</sub>C<sub>2</sub> MXene and Pt as Co-Catalysts for Highly Efficient Photocatalytic Hydrogen Evolution over g-C<sub>3</sub>N<sub>4</sub>. *Phys. Chem. Chem. Phys.* **2018**, *20*, 11405–11411.

- 1  
2  
3 (134) Luo, J.; Tao, X.; Zhang, J.; Xia, Y.; Huang, H.; Zhang, L.; Gan, Y.; Liang, C.; Zhang, W.  
4 Sn<sup>4+</sup> Ion Decorated Highly Conductive Ti<sub>3</sub>C<sub>2</sub> MXene: Promising Lithium-Ion Anodes with  
5 Enhanced Volumetric Capacity and Cyclic Performance. *ACS Nano* **2016**, *10*, 2491–2499.
- 6 (135) Peng, Q.; Guo, J.; Zhang, Q.; Xiang, J.; Liu, B.; Zhou, A.; Liu, R.; Tian, Y. Unique Lead  
7 Adsorption Behavior of Activated Hydroxyl Group in Two-Dimensional Titanium  
8 Carbide. *J. Am. Chem. Soc.* **2014**, *136*, 4113–4116.
- 9 (136) Wenderich, K.; Mul, G. Methods, Mechanism, and Applications of Photodeposition in  
10 Photocatalysis: A Review. *Chem. Rev.* **2016**, *116*, 14587–14619.
- 11 (137) Li, J.; Qin, R.; Yan, L.; Chi, Z.; Yu, Z.; Li, N.; Hu, M.; Chen, H.; Shan, G. Plasmonic Light  
12 Illumination Creates a Channel To Achieve Fast Degradation of Ti<sub>3</sub>C<sub>2</sub>T<sub>x</sub> Nanosheets.  
13 *Inorg. Chem.* **2019**, *58*, 7285–7294.
- 14 (138) Shen, S.; Ke, T.; Rajavel, K.; Yang, K.; Lin, D. Dispersibility and Photochemical Stability  
15 of Delaminated MXene Flakes in Water. *Small* **2020**, 2002433.
- 16 (139) Ma, T. Y.; Cao, J. L.; Jaroniec, M.; Qiao, S. Z. Interacting Carbon Nitride and Titanium  
17 Carbide Nanosheets for High-Performance Oxygen Evolution. *Angew. Chem. Int. Ed.*  
18 **2016**, *55*, 1138–1142.
- 19 (140) Sambyal, P.; Iqbal, A.; Hong, J.; Kim, H.; Kim, M.-K.; Hong, S. M.; Han, M.; Gogotsi,  
20 Y.; Koo, C. M. Ultralight and Mechanically Robust Ti<sub>3</sub>C<sub>2</sub>T<sub>x</sub> Hybrid Aerogel Reinforced  
21 by Carbon Nanotubes for Electromagnetic Interference Shielding. *ACS Appl. Mater.*  
22 *Interfaces* **2019**, *11*, 38046–38054.
- 23 (141) Zhao, M.-Q.; Ren, C. E.; Ling, Z.; Lukatskaya, M. R.; Zhang, C.; Van Aken, K. L.;  
24 Barsoum, M. W.; Gogotsi, Y. Flexible MXene/Carbon Nanotube Composite Paper with  
25 High Volumetric Capacitance. *Adv. Mater.* **2015**, *27*, 339–345.
- 26 (142) Yue, Y.; Liu, N.; Ma, Y.; Wang, S.; Liu, W.; Luo, C.; Zhang, H.; Cheng, F.; Rao, J.; Hu,  
27 X.; Su, J.; Gao, Y. Highly Self-Healable 3D Microsupercapacitor with MXene–Graphene  
28 Composite Aerogel. *ACS Nano* **2018**, *12*, 4224–4232.
- 29 (143) Li, Y.; Ding, L.; Guo, Y.; Liang, Z.; Cui, H.; Tian, J. Boosting the Photocatalytic Ability  
30 of G-C<sub>3</sub>N<sub>4</sub> for Hydrogen Production by Ti<sub>3</sub>C<sub>2</sub> MXene Quantum Dots. *ACS Appl. Mater.*  
31 *Interfaces* **2019**, *11*, 41440–41447.
- 32 (144) Yan, J.; Ren, C. E.; Maleski, K.; Hatter, C. B.; Anasori, B.; Urbankowski, P.; Sarycheva,  
33 A.; Gogotsi, Y. Flexible MXene/Graphene Films for Ultrafast Supercapacitors with  
34 Outstanding Volumetric Capacitance. *Adv. Funct. Mater.* **2017**, *27*, 1701264.
- 35 (145) Yu, P.; Cao, G.; Yi, S.; Zhang, X.; Li, C.; Sun, X.; Wang, K.; Ma, Y. Binder-Free 2D  
36 Titanium Carbide (MXene)/Carbon Nanotube Composites for High-Performance Lithium-  
37 Ion Capacitors. *Nanoscale* **2018**, *10*, 5906–5913.
- 38 (146) Yang, C.; Jiang, Q.; Li, W.; He, H.; Yang, L.; Lu, Z.; Huang, H. Ultrafine Pt Nanoparticle-  
39 Decorated 3D Hybrid Architectures Built from Reduced Graphene Oxide and MXene  
40 Nanosheets for Methanol Oxidation. *Chem. Mater.* **2019**, *31*, 9277–9287.
- 41 (147) Gu, H.; Xing, Y.; Xiong, P.; Tang, H.; Li, C.; Chen, S.; Zeng, R.; Han, K.; Shi, G. Three-  
42 Dimensional Porous Ti<sub>3</sub>C<sub>2</sub>T<sub>x</sub> MXene–Graphene Hybrid Films for Glucose Biosensing.  
43 *ACS Appl. Nano Mater.* **2019**, *2*, 6537–6545.
- 44 (148) Yang, L.; Chen, W.; Yang, R.; Chen, A.; Zhang, H.; Sun, Y.; Jia, Y.; Li, X.; Tang, Z.; Gui,  
45 X. Fabrication of MoO<sub>x</sub>/Mo<sub>2</sub>C-Layered Hybrid Structures by Direct Thermal Oxidation of  
46 Mo<sub>2</sub>C. *ACS Appl. Mater. Interfaces* **2020**, *12*, 10755–10762.
- 47  
48  
49  
50  
51  
52  
53  
54  
55  
56  
57  
58  
59  
60

- 1  
2  
3 (149) Yu, M.; Wang, Z.; Liu, J.; Sun, F.; Yang, P.; Qiu, J. A Hierarchically Porous and  
4 Hydrophilic 3D Nickel–Iron/MXene Electrode for Accelerating Oxygen and Hydrogen  
5 Evolution at High Current Densities. *Nano Energy* **2019**, *63*, 103880.  
6  
7 (150) Hope, M. A.; Forse, A. C.; Griffith, K. J.; Lukatskaya, M. R.; Ghidui, M.; Gogotsi, Y.;  
8 Grey, C. P. NMR Reveals the Surface Functionalisation of Ti<sub>3</sub>C<sub>2</sub> MXene. *Phys. Chem.*  
9 *Chem. Phys.* **2016**, *18*, 5099–5102.  
10  
11 (151) Wu, X.; Zhou, S.; Wang, Z.; Liu, J.; Pei, W.; Yang, P.; Zhao, J.; Qiu, J. Engineering  
12 Multifunctional Collaborative Catalytic Interface Enabling Efficient Hydrogen Evolution  
13 in All PH Range and Seawater. *Adv. Energy Mater.* **2019**, *9*, 1901333.  
14  
15 (152) Hantanasirisakul, K.; Gogotsi, Y. Electronic and Optical Properties of 2D Transition Metal  
16 Carbides and Nitrides (MXenes). *Adv. Mater.* **2018**, *30*, 1804779.  
17  
18 (153) Hao, C.; Wu, Y.; An, Y.; Cui, B.; Lin, J.; Li, X.; Wang, D.; Jiang, M.; Cheng, Z.; Hu, S.  
19 Interface-Coupling of CoFe-LDH on MXene as High-Performance Oxygen Evolution  
20 Catalyst. *Mater. Today Energy* **2019**, *12*, 453–462.  
21  
22 (154) Pandey, M.; Thygesen, K. S. Two-Dimensional MXenes as Catalysts for Electrochemical  
23 Hydrogen Evolution: A Computational Screening Study. *J. Phys. Chem. C* **2017**, *121*,  
24 13593–13598.  
25  
26 (155) Gao, G.; O’Mullane, A. P.; Du, A. 2D MXenes: A New Family of Promising Catalysts for  
27 the Hydrogen Evolution Reaction. *ACS Catal.* **2017**, *7*, 494–500.  
28  
29 (156) Zheng, J.; Sun, X.; Qiu, C.; Yan, Y.; Yao, Z.; Deng, S.; Zhong, X.; Zhuang, G.; Wei, Z.;  
30 Wang, J. High-Throughput Screening of Hydrogen Evolution Reaction Catalysts in  
31 MXene Materials. *J. Phys. Chem. C* **2020**, *124*, 13695–13705.  
32  
33 (157) Yuan, W.; Cheng, L.; An, Y.; Wu, H.; Yao, N.; Fan, X.; Guo, X. MXene Nanofibers as  
34 Highly Active Catalysts for Hydrogen Evolution Reaction. *ACS Sustainable Chem. Eng.*  
35 **2018**, *6*, 8976–8982.  
36  
37 (158) Yang, X.; Gao, N.; Zhou, S.; Zhao, J. MXene Nanoribbons as Electrocatalysts for the  
38 Hydrogen Evolution Reaction with Fast Kinetics. *Phys. Chem. Chem. Phys.* **2018**, *20*,  
39 19390–19397.  
40  
41 (159) Zhang, J.; Zhao, Y.; Guo, X.; Chen, C.; Dong, C.-L.; Liu, R.-S.; Han, C.-P.; Li, Y.;  
42 Gogotsi, Y.; Wang, G. Single Platinum Atoms Immobilized on an MXene as an Efficient  
43 Catalyst for the Hydrogen Evolution Reaction. *Nat. Catal.* **2018**, *1*, 985–992.  
44  
45 (160) Kuznetsov, D. A.; Chen, Z.; Kumar, P. V.; Tsoukalou, A.; Kierzkowska, A.; Abdala, P.  
46 M.; Safonova, O. V.; Fedorov, A.; Müller, C. R. Single Site Cobalt Substitution in 2D  
47 Molybdenum Carbide (MXene) Enhances Catalytic Activity in the Hydrogen Evolution  
48 Reaction. *J. Am. Chem. Soc.* **2019**, *141*, 17809–17816.  
49  
50 (161) Ramalingam, V.; Varadhan, P.; Fu, H.; Kim, H.; Zhang, D.; Chen, S.; Song, L.; Ma, D.;  
51 Wang, Y.; Alshareef, H. N.; He, J. Heteroatom-Mediated Interactions between Ruthenium  
52 Single Atoms and an MXene Support for Efficient Hydrogen Evolution. *Adv. Mater.* **2019**,  
53 *31*, 1903841.  
54  
55 (162) Li, Z.; Cui, Y.; Wu, Z.; Milligan, C.; Zhou, L.; Mitchell, G.; Xu, B.; Shi, E.; Miller, J. T.;  
56 Ribeiro, F. H.; Wu, Y. Reactive Metal–Support Interactions at Moderate Temperature in  
57 Two-Dimensional Niobium-Carbide-Supported Platinum Catalysts. *Nat. Catal.* **2018**, *1*,  
58 349–355.  
59  
60 (163) Le, T. A.; Bui, Q. V.; Tran, N. Q.; Cho, Y.; Hong, Y.; Kawazoe, Y.; Lee, H. Synergistic  
Effects of Nitrogen Doping on MXene for Enhancement of Hydrogen Evolution Reaction.  
*ACS Sustainable Chem. Eng.* **2019**, *7*, 16879–16888.

- 1  
2  
3 (164) Qu, G.; Zhou, Y.; Wu, T.; Zhao, G.; Li, F.; Kang, Y.; Xu, C. Phosphorized MXene-Phase  
4 Molybdenum Carbide as an Earth-Abundant Hydrogen Evolution Electrocatalyst. *ACS*  
5 *Appl. Energy Mater.* **2018**, *1*, 7206–7212.
- 6 (165) Yoon, Y.; Tiwari, A. P.; Choi, M.; Novak, T. G.; Song, W.; Chang, H.; Zyung, T.; Lee, S.  
7 S.; Jeon, S.; An, K. Precious-Metal-Free Electrocatalysts for Activation of Hydrogen  
8 Evolution with Nonmetallic Electron Donor: Chemical Composition Controllable  
9 Phosphorous Doped Vanadium Carbide MXene. *Adv. Funct. Mater.* **2019**, *29*, 1903443.
- 10 (166) He, Y.; He, Q.; Wang, L.; Zhu, C.; Golani, P.; Handoko, A. D.; Yu, X.; Gao, C.; Ding, M.;  
11 Wang, X.; Liu, F.; Zeng, Q.; Yu, P.; Guo, S.; Yakobson, B. I.; Wang, L.; Seh, Z. W.;  
12 Zhang, Z.; Wu, M.; Wang, Q. J.; Zhang, H.; Liu, Z. Self-Gating in Semiconductor  
13 Electrocatalysis. *Nat. Mater.* **2019**, *18*, 1098–1104.
- 14 (167) Du, C.-F.; Dinh, K. N.; Liang, Q.; Zheng, Y.; Luo, Y.; Zhang, J.; Yan, Q. Self-Assemble  
15 and *In Situ* Formation of Ni<sub>1-x</sub>Fe<sub>x</sub>PS<sub>3</sub> Nanomosaic-Decorated MXene Hybrids for Overall  
16 Water Splitting. *Adv. Energy Mater.* **2018**, *8*, 1801127.
- 17 (168) Yue, Q.; Sun, J.; Chen, S.; Zhou, Y.; Li, H.; Chen, Y.; Zhang, R.; Wei, G.; Kang, Y.  
18 Hierarchical Mesoporous MXene–NiCoP Electrocatalyst for Water-Splitting. *ACS Appl.*  
19 *Mater. Interfaces* **2020**, *12*, 18570–18577.
- 20 (169) Xiu, L.; Wang, Z.; Yu, M.; Wu, X.; Qiu, J. Aggregation-Resistant 3D MXene-Based  
21 Architecture as Efficient Bifunctional Electrocatalyst for Overall Water Splitting. *ACS*  
22 *Nano* **2018**, *12*, 8017–8028.
- 23 (170) Selvam, N. C. S.; Lee, J.; Choi, G. H.; Oh, M. J.; Xu, S.; Lim, B.; Yoo, P. J. MXene  
24 Supported Co<sub>x</sub>A<sub>y</sub> (A = OH, P, Se) Electrocatalysts for Overall Water Splitting: Unveiling  
25 the Role of Anions in Intrinsic Activity and Stability. *J. Mater. Chem. A* **2019**, *7*, 27383–  
26 27393.
- 27 (171) Wang, H.; Lin, Y.; Liu, S.; Li, J.; Bu, L.; Chen, J.; Xiao, X.; Choi, J.-H.; Gao, L.; Lee, J.-  
28 M. Confined Growth of Pyridinic N–Mo<sub>2</sub>C Sites on MXenes for Hydrogen Evolution. *J.*  
29 *Mater. Chem. A* **2020**, *8*, 7109–7116.
- 30 (172) Attanayake, N. H.; Abeyweera, S. C.; Thenuwara, A. C.; Anasori, B.; Gogotsi, Y.; Sun,  
31 Y.; Strongin, D. R. Vertically Aligned MoS<sub>2</sub> on Ti<sub>3</sub>C<sub>2</sub> (MXene) as an Improved HER  
32 Catalyst. *J. Mater. Chem. A* **2018**, *6*, 16882–16889.
- 33 (173) Liu, J.; Liu, Y.; Xu, D.; Zhu, Y.; Peng, W.; Li, Y.; Zhang, F.; Fan, X. Hierarchical  
34 “Nanoroll” like MoS<sub>2</sub>/Ti<sub>3</sub>C<sub>2</sub>T<sub>x</sub> Hybrid with High Electrocatalytic Hydrogen Evolution  
35 Activity. *Appl. Catal. B: Environ.* **2019**, *241*, 89–94.
- 36 (174) Kuang, P.; He, M.; Zhu, B.; Yu, J.; Fan, K.; Jaroniec, M. 0D/2D NiS<sub>2</sub>/V-MXene  
37 Composite for Electrocatalytic H<sub>2</sub> Evolution. *J. Catal.* **2019**, *375*, 8–20.
- 38 (175) Jiang, H.; Wang, Z.; Yang, Q.; Tan, L.; Dong, L.; Dong, M. Ultrathin Ti<sub>3</sub>C<sub>2</sub>T<sub>x</sub> (MXene)  
39 Nanosheet-Wrapped NiSe<sub>2</sub> Octahedral Crystal for Enhanced Supercapacitor Performance  
40 and Synergetic Electrocatalytic Water Splitting. *Nano-Micro Lett.* **2019**, *11*, 31.
- 41 (176) Wang, Z.; Xu, W.; Yu, K.; Feng, Y.; Zhu, Z. 2D Heterogeneous Vanadium Compound  
42 Interfacial Modulation Enhanced Synergistic Catalytic Hydrogen Evolution for Full PH  
43 Range Seawater Splitting. *Nanoscale* **2020**, *12*, 6176–6187.
- 44 (177) Du, C.; Sun, X.; Yu, H.; Liang, Q.; Dinh, K. N.; Zheng, Y.; Luo, Y.; Wang, Z.; Yan, Q.  
45 Synergy of Nb Doping and Surface Alloy Enhanced on Water–Alkali Electrocatalytic  
46 Hydrogen Generation Performance in Ti-Based MXene. *Adv. Sci.* **2019**, 1900116.
- 47 (178) Zhao, G.; Rui, K.; Dou, S. X.; Sun, W. Boosting Electrochemical Water Oxidation: The  
48 Merits of Heterostructured Electrocatalysts. *J. Mater. Chem. A* **2020**, *8*, 6393–6405.
- 49  
50  
51  
52  
53  
54  
55  
56  
57  
58  
59  
60

- 1  
2  
3  
4 (179) Li, N.; Wei, S.; Xu, Y.; Liu, J.; Wu, J.; Jia, G.; Cui, X. Synergetic Enhancement of Oxygen  
5 Evolution Reaction by  $\text{Ti}_3\text{C}_2\text{T}_x$  Nanosheets Supported Amorphous  $\text{FeOOH}$  Quantum Dots.  
6 *Electrochim. Acta* **2018**, *290*, 364–368.
- 7 (180) Wu, Z.; Wang, H.; Xiong, P.; Li, G.; Qiu, T.; Gong, W.-B.; Zhao, F.; Li, C.; Li, Q.; Wang,  
8 G.; Geng, F. Molecularly Thin Nitride Sheets Stabilized by Titanium Carbide as Efficient  
9 Bifunctional Electrocatalysts for Fiber-Shaped Rechargeable Zinc-Air Batteries. *Nano*  
10 *Lett.* **2020**, *20*, 2892–2898.
- 11 (181) Hao, N.; Wei, Y.; Wang, J.; Wang, Z.; Zhu, Z.; Zhao, S.; Han, M.; Huang, X. *In Situ*  
12 Hybridization of an MXene/ $\text{TiO}_2$ /NiFeCo-Layered Double Hydroxide Composite for  
13 Electrochemical and Photoelectrochemical Oxygen Evolution. *RSC Adv.* **2018**, *8*, 20576–  
14 20584.
- 15 (182) Zhang, Y.; Jiang, H.; Lin, Y.; Liu, H.; He, Q.; Wu, C.; Duan, T.; Song, L. *In Situ* Growth  
16 of Cobalt Nanoparticles Encapsulated Nitrogen-Doped Carbon Nanotubes among  $\text{Ti}_3\text{C}_2\text{T}_x$   
17 (MXene) Matrix for Oxygen Reduction and Evolution. *Adv. Mater. Interfaces* **2018**, *5*,  
18 1800392.
- 19 (183) Liu, J.; Chen, T.; Juan, P.; Peng, W.; Li, Y.; Zhang, F.; Fan, X. Hierarchical Cobalt  
20 Borate/MXenes Hybrid with Extraordinary Electrocatalytic Performance in Oxygen  
21 Evolution Reaction. *ChemSusChem* **2018**, *11*, 3758–3765.
- 22 (184) Deng, S.; Yang, F.; Zhang, Q.; Zhong, Y.; Zeng, Y.; Lin, S.; Wang, X.; Lu, X.; Wang, C.-  
23 Z.; Gu, L.; Xia, X.; Tu, J. Phase Modulation of (1T-2H)- $\text{MoSe}_2$ / $\text{TiC}$ -C Shell/Core Arrays  
24 via Nitrogen Doping for Highly Efficient Hydrogen Evolution Reaction. *Adv. Mater.* **2018**,  
25 *30*, 1802223.
- 26 (185) Chen, Y.; Lai, Z.; Zhang, X.; Fan, Z.; He, Q.; Tan, C.; Zhang, H. Phase Engineering of  
27 Nanomaterials. *Nat. Rev. Chem.* **2020**, *4*, 243–256.
- 28 (186) Benchakar, M.; Bilyk, T.; Garnero, C.; Loupias, L.; Morais, C.; Pacaud, J.; Canaff, C.;  
29 Chartier, P.; Morisset, S.; Guignard, N.; Mauchamp, V.; Célérier, S.; Habrioux, A. MXene  
30 Supported Cobalt Layered Double Hydroxide Nanocrystals: Facile Synthesis Route for a  
31 Synergistic Oxygen Evolution Reaction Electrocatalyst. *Adv. Mater. Interfaces* **2019**, *6*,  
32 1901328.
- 33 (187) Ran, J.; Gao, G.; Li, F.-T.; Ma, T.-Y.; Du, A.; Qiao, S.-Z.  $\text{Ti}_3\text{C}_2$  MXene Co-Catalyst on  
34 Metal Sulfide Photo-Absorbers for Enhanced Visible-Light Photocatalytic Hydrogen  
35 Production. *Nat. Commun.* **2017**, *8*, 13907.
- 36 (188) Sun, Y.; Meng, X.; Dall’Agnese, Y.; Dall’Agnese, C.; Duan, S.; Gao, Y.; Chen, G.; Wang,  
37 X.-F. 2D MXenes as Co-Catalysts in Photocatalysis: Synthetic Methods. *Nano-Micro Lett.*  
38 **2019**, *11*, 79.
- 39 (189) Lin, J.; Yu, Y.; Zhang, Z.; Gao, F.; Liu, S.; Wang, W.; Li, G. A Novel Approach for  
40 Achieving High-Efficiency Photoelectrochemical Water Oxidation in InGaN Nanorods  
41 Grown on Si System: MXene Nanosheets as Multifunctional Interfacial Modifier. *Adv.*  
42 *Funct. Mater.* **2020**, *30*, 1910479.
- 43 (190) Kong, X.; Peng, Z.; Jiang, R.; Jia, P.; Feng, J.; Yang, P.; Chi, Q.; Ye, W.; Xu, F.; Gao, P.  
44 Nanolayered Heterostructures of N-Doped  $\text{TiO}_2$  and N-Doped Carbon for Hydrogen  
45 Evolution. *ACS Appl. Nano Mater.* **2020**, *3*, 1373–1381.
- 46 (191) Jia, G.; Wang, Y.; Cui, X.; Zheng, W. Highly Carbon-Doped  $\text{TiO}_2$  Derived from MXene  
47 Boosting the Photocatalytic Hydrogen Evolution. *ACS Sustainable Chem. Eng.* **2018**, *6*,  
48 13480–13486.
- 49  
50  
51  
52  
53  
54  
55  
56  
57  
58  
59  
60



- 1  
2  
3 (192) Xia, F.; Lao, J.; Yu, R.; Sang, X.; Luo, J.; Li, Y.; Wu, J. Ambient Oxidation of  $\text{Ti}_3\text{C}_2$   
4 MXene Initialized by Atomic Defects. *Nanoscale* **2019**, *11*, 23330–23337.
- 5 (193) Chae, Y.; Kim, S. J.; Cho, S.-Y.; Choi, J.; Maleski, K.; Lee, B.-J.; Jung, H.-T.; Gogotsi,  
6 Y.; Lee, Y.; Ahn, C. W. An Investigation into the Factors Governing the Oxidation of  
7 Two-Dimensional  $\text{Ti}_3\text{C}_2$  MXene. *Nanoscale* **2019**, *11*, 8387–8393.
- 8 (194) Su, T.; Peng, R.; Hood, Z. D.; Naguib, M.; Ivanov, I. N.; Keum, J. K.; Qin, Z.; Guo, Z.;  
9 Wu, Z. One-Step Synthesis of  $\text{Nb}_2\text{O}_5/\text{C}/\text{Nb}_2\text{C}$  (MXene) Composites and Their Use as  
10 Photocatalysts for Hydrogen Evolution. *ChemSusChem* **2018**, *11*, 688–699.
- 11 (195) Tian, Y.; An, Y.; Wei, H.; Wei, C.; Tao, Y.; Li, Y.; Xi, B.; Xiong, S.; Feng, J.; Qian, Y.  
12 Micron-Sized Nanoporous Vanadium Pentoxide Arrays for High-Performance Gel Zinc-  
13 Ion Batteries and Potassium Batteries. *Chem. Mater.* **2020**, *32*, 4054–4064.
- 14 (196) Li, Y.; Yin, Z.; Ji, G.; Liang, Z.; Xue, Y.; Guo, Y.; Tian, J.; Wang, X.; Cui, H. 2D/2D/2D  
15 Heterojunction of  $\text{Ti}_3\text{C}_2$  MXene/ $\text{MoS}_2$  Nanosheets/ $\text{TiO}_2$  Nanosheets with Exposed (001)  
16 Facets toward Enhanced Photocatalytic Hydrogen Production Activity. *Appl. Catal. B:*  
17 *Environ.* **2019**, *246*, 12–20.
- 18 (197) Cheng, L.; Chen, Q.; Li, J.; Liu, H. Boosting the Photocatalytic Activity of  $\text{CdLa}_2\text{S}_4$  for  
19 Hydrogen Production Using  $\text{Ti}_3\text{C}_2$  MXene as a Co-Catalyst. *Appl. Catal. B: Environ.* **2020**,  
20 *267*, 118379.
- 21 (198) Wang, H.; Sun, Y.; Wu, Y.; Tu, W.; Wu, S.; Yuan, X.; Zeng, G.; Xu, Z. J.; Li, S.; Chew,  
22 J. W. Electrical Promotion of Spatially Photoinduced Charge Separation *via* Interfacial-  
23 Built-in Quasi-Alloying Effect in Hierarchical  $\text{Zn}_2\text{In}_2\text{S}_5/\text{Ti}_3\text{C}_2(\text{O}, \text{OH})_x$  Hybrids toward  
24 Efficient Photocatalytic Hydrogen Evolution and Environmental Remediation. *Appl.*  
25 *Catal. B: Environ.* **2019**, *245*, 290–301.
- 26 (199) Su, T.; Hood, Z. D.; Naguib, M.; Bai, L.; Luo, S.; Rouleau, C. M.; Ivanov, I. N.; Ji, H.;  
27 Qin, Z.; Wu, Z. 2D/2D Heterojunction of  $\text{Ti}_3\text{C}_2/\text{g-C}_3\text{N}_4$  Nanosheets for Enhanced  
28 Photocatalytic Hydrogen Evolution. *Nanoscale* **2019**, *11*, 8138–8149.
- 29 (200) Ren, J.; Zong, H.; Sun, Y.; Gong, S.; Feng, Y.; Wang, Z.; Hu, L.; Yu, K.; Zhu, Z. 2D  
30 Organ-like Molybdenum Carbide (MXene) Coupled with  $\text{MoS}_2$  Nanoflowers Enhances  
31 the Catalytic Activity in the Hydrogen Evolution Reaction. *CrystEngComm* **2020**, *22*,  
32 1395–1403.
- 33 (201) Djire, A.; Zhang, H.; Liu, J.; Miller, E. M.; Neale, N. R. Electrocatalytic and  
34 Optoelectronic Characteristics of the Two-Dimensional Titanium Nitride  $\text{Ti}_4\text{N}_3\text{T}_x$  MXene.  
35 *ACS Appl. Mater. Interfaces* **2019**, *11*, 11812–11823.
- 36 (202) Handoko, A. D.; Wei, F.; Jenndy; Yeo, B. S.; Seh, Z. W. Understanding Heterogeneous  
37 Electrocatalytic Carbon Dioxide Reduction through *Operando* Techniques. *Nat. Catal.*  
38 **2018**, *1*, 922–934.
- 39 (203) Jiang, L.; Duan, J.; Zhu, J.; Chen, S.; Antonietti, M. Iron-Cluster-Directed Synthesis of  
40 2D/2D Fe–N–C/MXene Superlattice-like Heterostructure with Enhanced Oxygen  
41 Reduction Electrocatalysis. *ACS Nano* **2020**, *14*, 2436–2444.
- 42 (204) Chen, J.; Yuan, X.; Lyu, F.; Zhong, Q.; Hu, H.; Pan, Q.; Zhang, Q. Integrating MXene  
43 Nanosheets with Cobalt-Tipped Carbon Nanotubes for an Efficient Oxygen Reduction  
44 Reaction. *J. Mater. Chem. A* **2019**, *7*, 1281–1286.
- 45 (205) Ostadhossein, A.; Guo, J.; Simeski, F.; Ihme, M. Functionalization of 2D Materials for  
46 Enhancing OER/ORR Catalytic Activity in Li–Oxygen Batteries. *Commun. Chem.* **2019**,  
47 *2*, 95.
- 48  
49  
50  
51  
52  
53  
54  
55  
56  
57  
58  
59  
60

- 1  
2  
3 (206) Zeng, Z.; Fu, G.; Yang, H. B.; Yan, Y.; Chen, J.; Yu, Z.; Gao, J.; Gan, L. Y.; Liu, B.; Chen,  
4 P. Bifunctional N-CoSe<sub>2</sub>/3D-MXene as Highly Efficient and Durable Cathode for  
5 Rechargeable Zn–Air Battery. *ACS Materials Lett.* **2019**, *1*, 432–439.
- 6 (207) Xue, Q.; Pei, Z.; Huang, Y.; Zhu, M.; Tang, Z.; Li, H.; Huang, Y.; Li, N.; Zhang, H.; Zhi,  
7 C. Mn<sub>3</sub>O<sub>4</sub> Nanoparticles on Layer-Structured Ti<sub>3</sub>C<sub>2</sub> MXene towards the Oxygen Reduction  
8 Reaction and Zinc–Air Batteries. *J. Mater. Chem. A* **2017**, *5*, 20818–20823.
- 9 (208) Zhang, H.; Qi, Q.; Zhang, P.; Zheng, W.; Chen, J.; Zhou, A.; Tian, W.; Zhang, W.; Sun,  
10 Z. Self-Assembled 3D MnO<sub>2</sub> Nanosheets@Delaminated-Ti<sub>3</sub>C<sub>2</sub> Aerogel as Sulfur Host for  
11 Lithium–Sulfur Battery Cathodes. *ACS Appl. Energy Mater.* **2019**, *2*, 705–714.
- 12 (209) Wang, J.; Zhai, P.; Zhao, T.; Li, M.; Yang, Z.; Zhang, H.; Huang, J. Laminar MXene-  
13 Nafion-Modified Separator with Highly Inhibited Shuttle Effect for Long-Life Lithium–  
14 Sulfur Batteries. *Electrochim. Acta* **2019**, *320*, 134558.
- 15 (210) Guo, D.; Ming, F.; Su, H.; Wu, Y.; Wahyudi, W.; Li, M.; Hedhili, M. N.; Sheng, G.; Li,  
16 L.-J.; Alshareef, H. N.; Li, Y.; Lai, Z. MXene Based Self-Assembled Cathode and  
17 Antifouling Separator for High-Rate and Dendrite-Inhibited Li–S Battery. *Nano Energy*  
18 **2019**, *61*, 478–485.
- 19 (211) Wang, H.-F.; Xu, Q. Materials Design for Rechargeable Metal-Air Batteries. *Matter* **2019**,  
20 *1*, 565–595.
- 21 (212) Li, Y.; Fu, J.; Zhong, C.; Wu, T.; Chen, Z.; Hu, W.; Amine, K.; Lu, J. Recent Advances in  
22 Flexible Zinc-Based Rechargeable Batteries. *Adv. Energy Mater.* **2019**, *9*, 1802605.
- 23 (213) Wang, H.-F.; Tang, C.; Zhang, Q. A Review of Precious-Metal-Free Bifunctional Oxygen  
24 Electrocatalysts: Rational Design and Applications in Zn–Air Batteries. *Adv. Funct.*  
25 *Mater.* **2018**, *28*, 1803329.
- 26 (214) Wen, Y.; Ma, C.; Wei, Z.; Zhu, X.; Li, Z. FeNC/MXene Hybrid Nanosheet as an Efficient  
27 Electrocatalyst for Oxygen Reduction Reaction. *RSC Adv.* **2019**, *9*, 13424–13430.
- 28 (215) Wang, Z.; Chen, X.; Shen, F.; Hang, X.; Niu, C. TiC MXene High Energy Density Cathode  
29 for Lithium-Air Battery. *Adv. Theory Simul.* **2018**, *1*, 1800059.
- 30 (216) Seh, Z. W.; Sun, Y.; Zhang, Q.; Cui, Y. Designing High-Energy Lithium–Sulfur Batteries.  
31 *Chem. Soc. Rev.* **2016**, *45*, 5605–5634.
- 32 (217) Liang, X.; Garsuch, A.; Nazar, L. F. Sulfur Cathodes Based on Conductive MXene  
33 Nanosheets for High-Performance Lithium-Sulfur Batteries. *Angew. Chem. Int. Ed.* **2015**,  
34 *54*, 3907–3911.
- 35 (218) Zhou, H.-Y.; Sui, Z.-Y.; Amin, K.; Lin, L.-W.; Wang, H.-Y.; Han, B.-H. Investigating the  
36 Electrocatalysis of a Ti<sub>3</sub>C<sub>2</sub>/Carbon Hybrid in Polysulfide Conversion of Lithium–Sulfur  
37 Batteries. *ACS Appl. Mater. Interfaces* **2020**, *12*, 13904–13913.
- 38 (219) Liang, P.; Zhang, L.; Wang, D.; Man, X.; Shu, H.; Wang, L.; Wan, H.; Du, X.; Wang, H.  
39 First-Principles Explorations of Li<sub>2</sub>S@V<sub>2</sub>CT<sub>x</sub> Hybrid Structure as Cathode Material for  
40 Lithium-sulfur Battery. *Appl. Surf. Sci.* **2019**, *489*, 677–683.
- 41 (220) Bao, W.; Su, D.; Zhang, W.; Guo, X.; Wang, G. 3D Metal Carbide@Mesoporous Carbon  
42 Hybrid Architecture as a New Polysulfide Reservoir for Lithium-Sulfur Batteries. *Adv.*  
43 *Funct. Mater.* **2016**, *26*, 8746–8756.
- 44 (221) Li, N.; Meng, Q.; Zhu, X.; Li, Z.; Ma, J.; Huang, C.; Song, J.; Fan, J. Lattice Constant-  
45 Dependent Anchoring Effect of MXenes for Lithium–Sulfur (Li–S) Batteries: A DFT  
46 Study. *Nanoscale* **2019**, *11*, 8485–8493.
- 47  
48  
49  
50  
51  
52  
53  
54  
55  
56  
57  
58  
59  
60

- 1  
2  
3 (222) Sim, E. S.; Yi, G. S.; Je, M.; Lee, Y.; Chung, Y.-C. Understanding the Anchoring Behavior  
4 of Titanium Carbide-Based MXenes Depending on the Functional Group in Li-S Batteries:  
5 A Density Functional Theory Study. *J. Power Sources* **2017**, *342*, 64–69.
- 6 (223) Bao, W.; Liu, L.; Wang, C.; Choi, S.; Wang, D.; Wang, G. Facile Synthesis of Crumpled  
7 Nitrogen-Doped MXene Nanosheets as a New Sulfur Host for Lithium-Sulfur Batteries.  
8 *Adv. Energy Mater.* **2018**, *8*, 1702485.
- 9 (224) Zhang, Y.; Mu, Z.; Yang, C.; Xu, Z.; Zhang, S.; Zhang, X.; Li, Y.; Lai, J.; Sun, Z.; Yang,  
10 Y.; Chao, Y.; Li, C.; Ge, X.; Yang, W.; Guo, S. Rational Design of MXene/1T-2H MoS<sub>2</sub>-  
11 C Nanohybrids for High-Performance Lithium-Sulfur Batteries. *Adv. Funct. Mater.* **2018**,  
12 *28*, 1707578.
- 13 (225) Du, C.; Wu, J.; Yang, P.; Li, S.; Xu, J.; Song, K. Embedding S@TiO<sub>2</sub> Nanospheres into  
14 MXene Layers as High Rate Cyclability Cathodes for Lithium-Sulfur Batteries.  
15 *Electrochim. Acta* **2019**, *295*, 1067–1074.
- 16 (226) Liu, P.; Qu, L.; Tian, X.; Yi, Y.; Xia, J.; Wang, T.; Nan, J.; Yang, P.; Wang, T.; Fang, B.;  
17 Li, M.; Yang, B. Ti<sub>3</sub>C<sub>2</sub>T<sub>x</sub>/Graphene Oxide Free-Standing Membranes as Modified  
18 Separators for Lithium–Sulfur Batteries with Enhanced Rate Performance. *ACS Appl.*  
19 *Energy Mater.* **2020**, *3*, 2708–2718.
- 20 (227) Jiao, L.; Zhang, C.; Geng, C.; Wu, S.; Li, H.; Lv, W.; Tao, Y.; Chen, Z.; Zhou, G.; Li, J.;  
21 Ling, G.; Wan, Y.; Yang, Q. Capture and Catalytic Conversion of Polysulfides by *In Situ*  
22 Built TiO<sub>2</sub>-MXene Heterostructures for Lithium–Sulfur Batteries. *Adv. Energy Mater.*  
23 **2019**, *9*, 1900219.
- 24 (228) Bao, W.; Shuck, C. E.; Zhang, W.; Guo, X.; Gogotsi, Y.; Wang, G. Boosting Performance  
25 of Na–S Batteries Using Sulfur-Doped Ti<sub>3</sub>C<sub>2</sub>T<sub>x</sub> MXene Nanosheets with a Strong Affinity  
26 to Sodium Polysulfides. *ACS Nano* **2019**, *13*, 11500–11509.
- 27 (229) Li, B.; Zhang, D.; Liu, Y.; Yu, Y.; Li, S.; Yang, S. Flexible Ti<sub>3</sub>C<sub>2</sub> MXene-Lithium Film  
28 with Lamellar Structure for Ultrastable Metallic Lithium Anodes. *Nano Energy* **2017**, *39*,  
29 654–661.
- 30 (230) Shi, H.; Yue, M.; Zhang, C. J.; Dong, Y.; Lu, P.; Zheng, S.; Huang, H.; Chen, J.; Wen, P.;  
31 Xu, Z.; Zheng, Q.; Li, X.; Yu, Y.; Wu, Z.-S. 3D Flexible, Conductive, and Recyclable  
32 Ti<sub>3</sub>C<sub>2</sub>T<sub>x</sub> MXene-Melamine Foam for High-Areal-Capacity and Long-Lifetime Alkali-  
33 Metal Anode. *ACS Nano* **2020**, *14*, 8678–8688.
- 34 (231) Luo, J.; Matios, E.; Wang, H.; Tao, X.; Li, W. Interfacial Structure Design of MXene-based  
35 Nanomaterials for Electrochemical Energy Storage and Conversion. *InfoMat* **2020**.
- 36 (232) Luo, J.; Wang, C.; Wang, H.; Hu, X.; Matios, E.; Lu, X.; Zhang, W.; Tao, X.; Li, W.  
37 Pillared MXene with Ultralarge Interlayer Spacing as a Stable Matrix for High  
38 Performance Sodium Metal Anodes. *Adv. Funct. Mater.* **2019**, *29*, 1805946.
- 39 (233) Orita, M.; Kojima, I.; Miyazaki, E. Catalysis by Transition-Metal Carbides. VII. Kinetic  
40 and XPS Studies of the Decomposition of Methanol on TiC, TaC, Mo<sub>2</sub>C, WC, and W<sub>2</sub>C.  
41 *Bull. Chem. Soc. Jpn.* **1986**, *59*, 689–695.
- 42 (234) Wang, S.; Ge, H.; Sun, S.; Zhang, J.; Liu, F.; Wen, X.; Yu, X.; Wang, L.; Zhang, Y.; Xu,  
43 H.; Neuefeind, J. C.; Qin, Z.; Chen, C.; Jin, C.; Li, Y.; He, D.; Zhao, Y. A New  
44 Molybdenum Nitride Catalyst with Rhombohedral MoS<sub>2</sub> Structure for Hydrogenation  
45 Applications. *J. Am. Chem. Soc.* **2015**, *137*, 4815–4822.
- 46 (235) Wang, S.; Temel, B.; Shen, J.; Jones, G.; Grabow, L. C.; Studt, F.; Bligaard, T.; Abild-  
47 Pedersen, F.; Christensen, C. H.; Nørskov, J. K. Universal Brønsted-Evans-Polanyi  
48  
49  
50  
51  
52  
53  
54  
55  
56  
57  
58  
59  
60

- Relations for C–C, C–O, C–N, N–O, N–N, and O–O Dissociation Reactions. *Catal. Lett.* **2011**, *141*, 370–373.
- (236) Khaledialidusti, R.; Mishra, A. K.; Barnoush, A. Atomic Defects in Monolayer Ordered Double Transition Metal Carbide ( $\text{Mo}_2\text{TiC}_2\text{T}_x$ ) MXene and  $\text{CO}_2$  Adsorption. *J. Mater. Chem. C* **2020**, *8*, 4771–4779.
- (237) Morales-García, Á.; Fernández-Fernández, A.; Viñes, F.; Illas, F.  $\text{CO}_2$  Abatement Using Two-Dimensional MXene Carbides. *J. Mater. Chem. A* **2018**, *6*, 3381–3385.
- (238) Handoko, A. D.; Steinmann, S. N.; Seh, Z. W. Theory-Guided Materials Design: Two-Dimensional MXenes in Electro- and Photocatalysis. *Nanoscale Horiz.* **2019**, *4*, 809–827.
- (239) Zhao, J.; Zhang, L.; Xie, X.-Y.; Li, X.; Ma, Y.; Liu, Q.; Fang, W.-H.; Shi, X.; Cui, G.; Sun, X.  $\text{Ti}_3\text{C}_2\text{T}_x$  (T = F, OH) MXene Nanosheets: Conductive 2D Catalysts for Ambient Electrohydrogenation of  $\text{N}_2$  to  $\text{NH}_3$ . *J. Mater. Chem. A* **2018**, *6*, 24031–24035.
- (240) Williams, W. S. Transition Metal Carbides, Nitrides, and Borides for Electronic Applications. *JOM* **1997**, *49*, 38–42.
- (241) Harris, K. J.; Bugnet, M.; Naguib, M.; Barsoum, M. W.; Goward, G. R. Direct Measurement of Surface Termination Groups and Their Connectivity in the 2D MXene  $\text{V}_2\text{CT}_x$  Using NMR Spectroscopy. *J. Phys. Chem. C* **2015**, *119*, 13713–13720.
- (242) Schultz, T.; Frey, N. C.; Hantanasirisakul, K.; Park, S.; May, S. J.; Shenoy, V. B.; Gogotsi, Y.; Koch, N. Surface Termination Dependent Work Function and Electronic Properties of  $\text{Ti}_3\text{C}_2\text{T}_x$  MXene. *Chem. Mater.* **2019**, *31*, 6590–6597.
- (243) Liu, Y.; Xiao, H.; Goddard, W. A. Schottky-Barrier-Free Contacts with Two-Dimensional Semiconductors by Surface-Engineered MXenes. *J. Am. Chem. Soc.* **2016**, *138*, 15853–15856.
- (244) Li, N.; Chen, X.; Ong, W.-J.; MacFarlane, D. R.; Zhao, X.; Cheetham, A. K.; Sun, C. Understanding of Electrochemical Mechanisms for  $\text{CO}_2$  Capture and Conversion into Hydrocarbon Fuels in Transition-Metal Carbides (MXenes). *ACS Nano* **2017**, *11*, 10825–10833.
- (245) Zhang, X.; Zhang, Z.; Li, J.; Zhao, X.; Wu, D.; Zhou, Z.  $\text{Ti}_2\text{CO}_2$  MXene: A Highly Active and Selective Photocatalyst for  $\text{CO}_2$  Reduction. *J. Mater. Chem. A* **2017**, *5*, 12899–12903.
- (246) Abild-Pedersen, F.; Greeley, J.; Studt, F.; Rossmeisl, J.; Munter, T. R.; Moses, P. G.; Skúlason, E.; Bligaard, T.; Nørskov, J. K. Scaling Properties of Adsorption Energies for Hydrogen-Containing Molecules on Transition-Metal Surfaces. *Phys. Rev. Lett.* **2007**, *99*, 016105.
- (247) Li, Z.; Yu, L.; Milligan, C.; Ma, T.; Zhou, L.; Cui, Y.; Qi, Z.; Libretto, N.; Xu, B.; Luo, J.; Shi, E.; Wu, Z.; Xin, H.; Delgass, W. N.; Miller, J. T.; Wu, Y. Two-Dimensional Transition Metal Carbides as Supports for Tuning the Chemistry of Catalytic Nanoparticles. *Nat. Commun.* **2018**, *9*, 5258.
- (248) Penner, S.; Armbrüster, M. Formation of Intermetallic Compounds by Reactive Metal-Support Interaction: A Frequently Encountered Phenomenon in Catalysis. *ChemCatChem* **2015**, *7*, 374–392.
- (249) Tackett, B. M.; Sheng, W.; Chen, J. G. Opportunities and Challenges in Utilizing Metal-Modified Transition Metal Carbides as Low-Cost Electrocatalysts. *Joule* **2017**, *1*, 253–263.
- (250) Sun, X.; Gao, Y.; Zhao, C.; Deng, S.; Zhong, X.; Zhuang, G.; Wei, Z.; Wang, J. Palladium Dimer Supported on  $\text{Mo}_2\text{CO}_2$  (MXene) for Direct Methane to Methanol Conversion. *Adv. Theory Simul.* **2019**, *2*, 1800158.

- 1  
2  
3 (251) Wang, A.; Li, J.; Zhang, T. Heterogeneous Single-Atom Catalysis. *Nat. Rev. Chem.* **2018**,  
4 2, 65–81.
- 5 (252) Zhao, D.; Chen, Z.; Yang, W.; Liu, S.; Zhang, X.; Yu, Y.; Cheong, W.-C.; Zheng, L.; Ren,  
6 F.; Ying, G.; Cao, X.; Wang, D.; Peng, Q.; Wang, G.; Chen, C. MXene (Ti<sub>3</sub>C<sub>2</sub>) Vacancy-  
7 Confined Single-Atom Catalyst for Efficient Functionalization of CO<sub>2</sub>. *J. Am. Chem. Soc.*  
8 **2019**, *141*, 4086–4093.
- 9 (253) Wu, J.; Huang, Y.; Ye, W.; Li, Y. CO<sub>2</sub> Reduction: From the Electrochemical to  
10 Photochemical Approach. *Adv. Sci.* **2017**, *4*, 1700194.
- 11 (254) Maeda, K.; Teramura, K.; Saito, N.; Inoue, Y.; Domen, K. Improvement of Photocatalytic  
12 Activity of (Ga<sub>1-x</sub>Zn<sub>x</sub>)(N<sub>1-x</sub>O<sub>x</sub>) Solid Solution for Overall Water Splitting by Co-Loading  
13 Cr and Another Transition Metal. *J. Catal.* **2006**, *243*, 303–308.
- 14 (255) Sels, B. F.; Voorde, M. H. van de. *Nanotechnology in Catalysis: Applications in the*  
15 *Chemical Industry, Energy Development, and Environment Protection*, 1st edition.;  
16 Nanotechnology innovation & applications; Wiley-VCH Verlag GmbH & Co. KGaA:  
17 Weinheim, 2017.
- 18 (256) Fresno, F.; Villar-García, I. J.; Collado, L.; Alfonso-González, E.; Reñones, P.; Barawi,  
19 M.; de la Peña O’Shea, V. A. Mechanistic View of the Main Current Issues in  
20 Photocatalytic CO<sub>2</sub> Reduction. *J. Phys. Chem. Lett.* **2018**, *9*, 7192–7204.
- 21 (257) Takanebe, K. Photocatalytic Water Splitting: Quantitative Approaches toward  
22 Photocatalyst by Design. *ACS Catal.* **2017**, *7*, 8006–8022.
- 23 (258) Zhang, Y.; Xia, W.; Wu, Y.; Zhang, P. Prediction of MXene Based 2D Tunable Band Gap  
24 Semiconductors: GW Quasiparticle Calculations. *Nanoscale* **2019**, *11*, 3993–4000.
- 25 (259) Yang, C.; Tan, Q.; Li, Q.; Zhou, J.; Fan, J.; Li, B.; Sun, J.; Lv, K. 2D/2D Ti<sub>3</sub>C<sub>2</sub> MXene/g-  
26 C<sub>3</sub>N<sub>4</sub> Nanosheets Heterojunction for High Efficient CO<sub>2</sub> Reduction Photocatalyst: Dual  
27 Effects of Urea. *Appl. Catal. B: Environ.* **2020**, *268*, 118738.
- 28 (260) Tang, Q.; Sun, Z.; Deng, S.; Wang, H.; Wu, Z. Decorating G-C<sub>3</sub>N<sub>4</sub> with Alkalinized Ti<sub>3</sub>C<sub>2</sub>  
29 MXene for Promoted Photocatalytic CO<sub>2</sub> Reduction Performance. *J. Colloid Interface Sci.*  
30 **2020**, *564*, 406–417.
- 31 (261) Martin, D. J.; Qiu, K.; Shevlin, S. A.; Handoko, A. D.; Chen, X.; Guo, Z.; Tang, J. Highly  
32 Efficient Photocatalytic H<sub>2</sub> Evolution from Water Using Visible Light and Structure-  
33 Controlled Graphitic Carbon Nitride. *Angew. Chem. Int. Ed.* **2014**, *53*, 9240–9245.
- 34 (262) Jiang, J.; Mu, Z.; Zhao, P.; Wang, H.; Lin, Y. Photogenerated Charge Behavior of BiOI/g-  
35 C<sub>3</sub>N<sub>4</sub> Photocatalyst in Photoreduction of Cr (VI): A Novel Understanding for High-  
36 Performance. *Mater. Chem. Phys.* **2020**, *252*, 123194.
- 37 (263) Xu, Y.; Wang, S.; Yang, J.; Han, B.; Nie, R.; Wang, J.; Dong, Y.; Yu, X.; Wang, J.; Jing,  
38 H. Highly Efficient Photoelectrocatalytic Reduction of CO<sub>2</sub> on the Ti<sub>3</sub>C<sub>2</sub>/g-C<sub>3</sub>N<sub>4</sub>  
39 Heterojunction with Rich Ti<sup>3+</sup> and Pyri-N Species. *J. Mater. Chem. A* **2018**, *6*, 15213–  
40 15220.
- 41 (264) Liu, X.; Xiao, J.; Peng, H.; Hong, X.; Chan, K.; Nørskov, J. K. Understanding Trends in  
42 Electrochemical Carbon Dioxide Reduction Rates. *Nat. Commun.* **2017**, *8*, 15438.
- 43 (265) Shen, J.; Shen, J.; Zhang, W.; Yu, X.; Tang, H.; Zhang, M.; Zulfiqar; Liu, Q. Built-in  
44 Electric Field Induced CeO<sub>2</sub>/Ti<sub>3</sub>C<sub>2</sub>-MXene Schottky-Junction for Coupled Photocatalytic  
45 Tetracycline Degradation and CO<sub>2</sub> Reduction. *Ceram. Int.* **2019**, *45*, 24146–24153.
- 46 (266) Ye, M.; Wang, X.; Liu, E.; Ye, J.; Wang, D. Boosting the Photocatalytic Activity of P25  
47 for Carbon Dioxide Reduction by Using a Surface-Alkalinized Titanium Carbide MXene  
48 as Cocatalyst. *ChemSusChem* **2018**, *11*, 1606–1611.
- 49  
50  
51  
52  
53  
54  
55  
56  
57  
58  
59  
60

- 1  
2  
3 (267) Xie, X.; Zhang, N.; Tang, Z.-R.; Anpo, M.; Xu, Y.-J.  $\text{Ti}_3\text{C}_2\text{T}_x$  MXene as a Janus Cocatalyst  
4 for Concurrent Promoted Photoactivity and Inhibited Photocorrosion. *Appl. Catal. B:*  
5 *Environ.* **2018**, *237*, 43–49.
- 6 (268) Guo, J.; Peng, Q.; Fu, H.; Zou, G.; Zhang, Q. Heavy-Metal Adsorption Behavior of Two-  
7 Dimensional Alkalization-Intercalated MXene by First-Principles Calculations. *J. Phys.*  
8 *Chem. C* **2015**, *119*, 20923–20930.
- 9 (269) Shipman, M. A.; Symes, M. D. Recent Progress towards the Electrosynthesis of Ammonia  
10 from Sustainable Resources. *Catal. Today* **2017**, *286*, 57–68.
- 11 (270) Honkala, K. Ammonia Synthesis from First-Principles Calculations. *Science* **2005**, *307*,  
12 555–558.
- 13 (271) Gao, Y.; Zhuo, H.; Cao, Y.; Sun, X.; Zhuang, G.; Deng, S.; Zhong, X.; Wei, Z.; Wang, J.  
14 A Theoretical Study of Electrocatalytic Ammonia Synthesis on Single Metal  
15 Atom/MXene. *Chin. J. Catal.* **2019**, *40*, 152–159.
- 16 (272) Yao, Y.; Zhu, S.; Wang, H.; Li, H.; Shao, M. A Spectroscopic Study on the Nitrogen  
17 Electrochemical Reduction Reaction on Gold and Platinum Surfaces. *J. Am. Chem. Soc.*  
18 **2018**, *140*, 1496–1501.
- 19 (273) Zhao, J.; Chen, Z. Single Mo Atom Supported on Defective Boron Nitride Monolayer as  
20 an Efficient Electrocatalyst for Nitrogen Fixation: A Computational Study. *J. Am. Chem.*  
21 *Soc.* **2017**, *139*, 12480–12487.
- 22 (274) Zheng, S.; Li, S.; Mei, Z.; Hu, Z.; Chu, M.; Liu, J.; Chen, X.; Pan, F. Electrochemical  
23 Nitrogen Reduction Reaction Performance of Single-Boron Catalysts Tuned by MXene  
24 Substrates. *J. Phys. Chem. Lett.* **2019**, *10*, 6984–6989.
- 25 (275) Wang, S.; Li, B.; Li, L.; Tian, Z.; Zhang, Q.; Chen, L.; Zeng, X. C. Highly Efficient  $\text{N}_2$   
26 Fixation Catalysts: Transition-Metal Carbides  $\text{M}_2\text{C}$  (MXenes). *Nanoscale* **2020**, *12*, 538–  
27 547.
- 28 (276) Shao, M.; Shao, Y.; Chen, W.; Ao, K. L.; Tong, R.; Zhu, Q.; Chan, I. N.; Ip, W. F.; Shi,  
29 X.; Pan, H. Efficient Nitrogen Fixation to Ammonia on MXenes. *Phys. Chem. Chem. Phys.*  
30 **2018**, *20*, 14504–14512.
- 31 (277) Azofra, L. M.; Li, N.; MacFarlane, D. R.; Sun, C. Promising Prospects for 2D  $d^2$ – $d^4$   $\text{M}_3\text{C}_2$   
32 Transition Metal Carbides (MXenes) in  $\text{N}_2$  Capture and Conversion into Ammonia. *Energy*  
33 *Environ. Sci.* **2016**, *9*, 2545–2549.
- 34 (278) Gao, Y.; Cao, Y.; Zhuo, H.; Sun, X.; Gu, Y.; Zhuang, G.; Deng, S.; Zhong, X.; Wei, Z.;  
35 Li, X.; Wang, J.  $\text{Mo}_2\text{TiC}_2$  MXene: A Promising Catalyst for Electrocatalytic Ammonia  
36 Synthesis. *Catal. Today* **2020**, *339*, 120–126.
- 37 (279) Luo, Y.; Chen, G.-F.; Ding, L.; Chen, X.; Ding, L.-X.; Wang, H. Efficient Electrocatalytic  
38  $\text{N}_2$  Fixation with MXene under Ambient Conditions. *Joule* **2019**, *3*, 279–289.
- 39 (280) Liao, Y.; Qian, J.; Xie, G.; Han, Q.; Dang, W.; Wang, Y.; Lv, L.; Zhao, S.; Luo, L.; Zhang,  
40 W.; Jiang, H.-Y.; Tang, J. 2D-Layered  $\text{Ti}_3\text{C}_2$  MXenes for Promoted Synthesis of  $\text{NH}_3$  on  
41 P25 Photocatalysts. *Appl. Catal. B: Environ.* **2020**, *273*, 119054.
- 42 (281) Suryanto, B. H. R.; Du, H.-L.; Wang, D.; Chen, J.; Simonov, A. N.; MacFarlane, D. R.  
43 Challenges and Prospects in the Catalysis of Electroreduction of Nitrogen to Ammonia.  
44 *Nat. Catal.* **2019**, *2*, 290–296.
- 45 (282) Zhao, Y.; Shi, R.; Bian, X.; Zhou, C.; Zhao, Y.; Zhang, S.; Wu, F.; Waterhouse, G. I. N.;  
46 Wu, L.; Tung, C.; Zhang, T. Ammonia Detection Methods in Photocatalytic and  
47 Electrocatalytic Experiments: How to Improve the Reliability of  $\text{NH}_3$  Production Rates?  
48 *Adv. Sci.* **2019**, *6*, 1802109.
- 49  
50  
51  
52  
53  
54  
55  
56  
57  
58  
59  
60

- 1  
2  
3 (283) Andersen, S. Z.; Čolić, V.; Yang, S.; Schwalbe, J. A.; Nielander, A. C.; McEnaney, J. M.;  
4 Enemark-Rasmussen, K.; Baker, J. G.; Singh, A. R.; Rohr, B. A.; Statt, M. J.; Blair, S. J.;  
5 Mezzavilla, S.; Kibsgaard, J.; Vesborg, P. C. K.; Cargnello, M.; Bent, S. F.; Jaramillo, T.  
6 F.; Stephens, I. E. L.; Nørskov, J. K.; Chorkendorff, I. A Rigorous Electrochemical  
7 Ammonia Synthesis Protocol with Quantitative Isotope Measurements. *Nature* **2019**, *570*,  
8 504–508.  
9  
10 (284) Habib, T.; Zhao, X.; Shah, S. A.; Chen, Y.; Sun, W.; An, H.; Lutkenhaus, J. L.; Radovic,  
11 M.; Green, M. J. Oxidation Stability of  $Ti_3C_2T_x$  MXene Nanosheets in Solvents and  
12 Composite Films. *npj 2D Mater. Appl.* **2019**, *3*, 8.  
13 (285) Li, L.; Wang, X.; Guo, H.; Yao, G.; Yu, H.; Tian, Z.; Li, B.; Chen, L. Theoretical Screening  
14 of Single Transition Metal Atoms Embedded in MXene Defects as Superior Electrocatalyst  
15 of Nitrogen Reduction Reaction. *Small Methods* **2019**, *3*, 1900337.  
16 (286) Huang, B.; Li, N.; Ong, W.-J.; Zhou, N. Single Atom-Supported MXene: How Single-  
17 Atomic-Site Catalysts Tune the High Activity and Selectivity of Electrochemical Nitrogen  
18 Fixation. *J. Mater. Chem. A* **2019**, *7*, 27620–27631.  
19 (287) Su, Y.-Q.; Wang, Y.; Liu, J.-X.; Filot, I. A. W.; Alexopoulos, K.; Zhang, L.; Muravev, V.;  
20 Zijlstra, B.; Vlachos, D. G.; Hensen, E. J. M. Theoretical Approach To Predict the Stability  
21 of Supported Single-Atom Catalysts. *ACS Catal.* **2019**, *9*, 3289–3297.  
22 (288) Liu, A.; Gao, M.; Ren, X.; Meng, F.; Yang, Y.; Yang, Q.; Guan, W.; Gao, L.; Liang, X.;  
23 Ma, T. A Two-Dimensional Ru@MXene Catalyst for Highly Selective Ambient  
24 Electrocatalytic Nitrogen Reduction. *Nanoscale* **2020**, *12*, 10933–10938.  
25 (289) Liu, D.; Zhang, G.; Ji, Q.; Zhang, Y.; Li, J. Synergistic Electrocatalytic Nitrogen Reduction  
26 Enabled by Confinement of Nanosized Au Particles onto a Two-Dimensional  $Ti_3C_2$   
27 Substrate. *ACS Appl. Mater. Interfaces* **2019**, *11*, 25758–25765.  
28 (290) Peng, W.; Luo, M.; Xu, X.; Jiang, K.; Peng, M.; Chen, D.; Chan, T.; Tan, Y. Spontaneous  
29 Atomic Ruthenium Doping in  $Mo_2CT_x$  MXene Defects Enhances Electrocatalytic Activity  
30 for the Nitrogen Reduction Reaction. *Adv. Energy Mater.* **2020**, *10*, 2001364.  
31 (291) Kong, W.; Gong, F. (Frank); Zhou, Q.; Yu, G.; Ji, L.; Sun, X.; Asiri, A. M.; Wang, T.;  
32 Luo, Y.; Xu, Y. An  $MnO_2$ - $Ti_3C_2T_x$  MXene Nanohybrid: An Efficient and Durable  
33 Electrocatalyst toward Artificial  $N_2$  Fixation to  $NH_3$  under Ambient Conditions. *J. Mater.*  
34 *Chem. A* **2019**, *7*, 18823–18827.  
35 (292) Zhang, J.; Yang, L.; Wang, H.; Zhu, G.; Wen, H.; Feng, H.; Sun, X.; Guan, X.; Wen, J.;  
36 Yao, Y. *In Situ* Hydrothermal Growth of  $TiO_2$  Nanoparticles on a Conductive  $Ti_3C_2T_x$   
37 MXene Nanosheet: A Synergistically Active Ti-Based Nanohybrid Electrocatalyst for  
38 Enhanced  $N_2$  Reduction to  $NH_3$  at Ambient Conditions. *Inorg. Chem.* **2019**, *58*, 5414–  
39 5418.  
40 (293) Liu, Q.; Ai, L.; Jiang, J. MXene-Derived  $TiO_2$ @C/g- $C_3N_4$  Heterojunctions for Highly  
41 Efficient Nitrogen Photofixation. *J. Mater. Chem. A* **2018**, *6*, 4102–4110.  
42 (294) Wang, H.; Zhao, R.; Qin, J.; Hu, H.; Fan, X.; Cao, X.; Wang, D. MIL-100(Fe)/ $Ti_3C_2$   
43 MXene as a Schottky Catalyst with Enhanced Photocatalytic Oxidation for Nitrogen  
44 Fixation Activities. *ACS Appl. Mater. Interfaces* **2019**, *11*, 44249–44262.  
45 (295) Pang, S.-Y.; Wong, Y.-T.; Yuan, S.; Liu, Y.; Tsang, M.-K.; Yang, Z.; Huang, H.; Wong,  
46 W.-T.; Hao, J. Universal Strategy for HF-Free Facile and Rapid Synthesis of Two-  
47 Dimensional MXenes as Multifunctional Energy Materials. *J. Am. Chem. Soc.* **2019**, *141*,  
48 9610–9616.  
49  
50  
51  
52  
53  
54  
55  
56  
57  
58  
59  
60

- 1  
2  
3 (296) Li, Y.; Shao, H.; Lin, Z.; Lu, J.; Liu, L.; Duployer, B.; Persson, P. O. Å.; Eklund, P.;  
4 Hultman, L.; Li, M.; Chen, K.; Zha, X.-H.; Du, S.; Rozier, P.; Chai, Z.; Raymundo-Piñero,  
5 E.; Taberna, P.-L.; Simon, P.; Huang, Q. A General Lewis Acidic Etching Route for  
6 Preparing MXenes with Enhanced Electrochemical Performance in Non-Aqueous  
7 Electrolyte. *Nat. Mater.* **2019**, *19*, 894–899.
- 8  
9 (297) Natu, V.; Pai, R.; Sokol, M.; Carey, M.; Kalra, V.; Barsoum, M. W. 2D  $Ti_3C_2T_z$  MXene  
10 Synthesized by Water-Free Etching of  $Ti_3AlC_2$  in Polar Organic Solvents. *Chem* **2020**, *6*,  
11 616–630.
- 12 (298) Zhang, C. J.; Pinilla, S.; McEvoy, N.; Cullen, C. P.; Anasori, B.; Long, E.; Park, S.-H.;  
13 Seral-Ascaso, A.; Shmeliov, A.; Krishnan, D.; Morant, C.; Liu, X.; Duesberg, G. S.;  
14 Gogotsi, Y.; Nicolosi, V. Oxidation Stability of Colloidal Two-Dimensional Titanium  
15 Carbides (MXenes). *Chem. Mater.* **2017**, *29*, 4848–4856.
- 16 (299) Chen, H.; Wen, Y.; Qi, Y.; Zhao, Q.; Qu, L.; Li, C. Pristine Titanium Carbide MXene  
17 Films with Environmentally Stable Conductivity and Superior Mechanical Strength. *Adv.*  
18 *Funct. Mater.* **2020**, *30*, 1906996.
- 19 (300) Zhao, X.; Vashisth, A.; Prehn, E.; Sun, W.; Shah, S. A.; Habib, T.; Chen, Y.; Tan, Z.;  
20 Lutkenhaus, J. L.; Radovic, M.; Green, M. J. Antioxidants Unlock Shelf-Stable  $Ti_3C_2T_x$   
21 (MXene) Nanosheet Dispersions. *Matter* **2019**, *1*, 513–526.
- 22 (301) Maleski, K.; Mochalin, V. N.; Gogotsi, Y. Dispersions of Two-Dimensional Titanium  
23 Carbide MXene in Organic Solvents. *Chem. Mater.* **2017**, *29*, 1632–1640.
- 24 (302) Kim, D.; Ko, T. Y.; Kim, H.; Lee, G. H.; Cho, S.; Koo, C. M. Nonpolar Organic Dispersion  
25 of 2D  $Ti_3C_2T_x$  MXene Flakes *via* Simultaneous Interfacial Chemical Grafting and Phase  
26 Transfer Method. *ACS Nano* **2019**, *13*, 13818–13828.
- 27 (303) Jin, D.; Johnson, L. R.; Raman, A. S.; Ming, X.; Gao, Y.; Du, F.; Wei, Y.; Chen, G.;  
28 Vojvodic, A.; Gogotsi, Y.; Meng, X. Computational Screening of 2D Ordered Double  
29 Transition-Metal Carbides (MXenes) as Electrocatalysts for Hydrogen Evolution  
30 Reaction. *J. Phys. Chem. C* **2020**, *124*, 10584–10592.
- 31 (304) Pinto, D.; Anasori, B.; Avireddy, H.; Shuck, C. E.; Hantanasirisakul, K.; Deysheer, G.;  
32 Morante, J. R.; Porzio, W.; Alshareef, H. N.; Gogotsi, Y. Synthesis and Electrochemical  
33 Properties of 2D Molybdenum Vanadium Carbides – Solid Solution MXenes. *J. Mater.*  
34 *Chem. A* **2020**, *8*, 8957–8968.
- 35 (305) Djire, A.; Bos, A.; Liu, J.; Zhang, H.; Miller, E. M.; Neale, N. R. Pseudocapacitive Storage  
36 in Nanolayered  $Ti_2NT_x$  MXene Using Mg-Ion Electrolyte. *ACS Appl. Nano Mater.* **2019**,  
37 *2*, 2785–2795.
- 38 (306) Urbankowski, P.; Anasori, B.; Hantanasirisakul, K.; Yang, L.; Zhang, L.; Haines, B.; May,  
39 S. J.; Billinge, S. J. L.; Gogotsi, Y. 2D Molybdenum and Vanadium Nitrides Synthesized  
40 by Ammoniation of 2D Transition Metal Carbides (MXenes). *Nanoscale* **2017**, *9*, 17722–  
41 17730.
- 42 (307) Xiao, X.; Yu, H.; Jin, H.; Wu, M.; Fang, Y.; Sun, J.; Hu, Z.; Li, T.; Wu, J.; Huang, L.;  
43 Gogotsi, Y.; Zhou, J. Salt-Templated Synthesis of 2D Metallic MoN and Other Nitrides.  
44 *ACS Nano* **2017**, *11*, 2180–2186.
- 45 (308) Ye, C.; Jiao, Y.; Jin, H.; Slattery, A. D.; Davey, K.; Wang, H.; Qiao, S. 2D MoN-VN  
46 Heterostructure To Regulate Polysulfides for Highly Efficient Lithium-Sulfur Batteries.  
47 *Angew. Chem. Int. Ed.* **2018**, *57*, 16703–16707.
- 48  
49  
50  
51  
52  
53  
54  
55  
56  
57  
58  
59  
60



- 1  
2  
3 (309) Jin, H.; Liu, X.; Vasileff, A.; Jiao, Y.; Zhao, Y.; Zheng, Y.; Qiao, S.-Z. Single-Crystal  
4 Nitrogen-Rich Two-Dimensional Mo<sub>5</sub>N<sub>6</sub> Nanosheets for Efficient and Stable Seawater  
5 Splitting. *ACS Nano* **2018**, *12*, 12761–12769.  
6  
7 (310) Singh, M. R.; Goodpaster, J. D.; Weber, A. Z.; Head-Gordon, M.; Bell, A. T. Mechanistic  
8 Insights into Electrochemical Reduction of CO<sub>2</sub> over Ag Using Density Functional Theory  
9 and Transport Models. *Proc Natl Acad Sci USA* **2017**, *114*, E8812–E8821.  
10 (311) Goodpaster, J. D.; Bell, A. T.; Head-Gordon, M. Identification of Possible Pathways for  
11 C–C Bond Formation during Electrochemical Reduction of CO<sub>2</sub>: New Theoretical Insights  
12 from an Improved Electrochemical Model. *J. Phys. Chem. Lett.* **2016**, *7*, 1471–1477.  
13 (312) Cheng, T.; Wang, L.; Merinov, B. V.; Goddard, W. A. Explanation of Dramatic PH-  
14 Dependence of Hydrogen Binding on Noble Metal Electrode: Greatly Weakened Water  
15 Adsorption at High PH. *J. Am. Chem. Soc.* **2018**, *140*, 7787–7790.  
16  
17  
18  
19  
20  
21  
22  
23  
24  
25  
26  
27  
28  
29  
30  
31  
32  
33  
34  
35  
36  
37  
38  
39  
40  
41  
42  
43  
44  
45  
46  
47  
48  
49  
50  
51  
52  
53  
54  
55  
56  
57  
58  
59  
60